

**SYNTHESIS AND STRUCTURE-PROPERTY RELATIONSHIPS OF A FEW
FLUORIDE COMPOUNDS: (I) MIXED-METAL FLUOROCARBONATES
AND (II) A REDUCED NIOBIUM OXYFLUORIDE**

A Dissertation Presented to
the Faculty of the Department of Chemistry
University of Houston

In Partial Fulfillment
of the Requirements for the Degree
Doctor of Philosophy

By

Thanh Thao Tran

May 2015

**SYNTHESIS AND STRUCTURE-PROPERTY RELATIONSHIPS OF A FEW
FLUORIDE COMPOUNDS: (I) MIXED-METAL FLUOROCARBONATES
AND (II) A REDUCED NIOBIUM OXYFLUORIDE**

Thanh Thao Tran

APPROVED:

Dr. P. Shiv Halasyamani, Chair

Dr. Arnold M. Guloy

Dr. Bernd Lorenz

Dr. Eric Bittner

Dr. Jakoah Brgoch

Dean, College of Natural Sciences and
Mathematics

*Dedicated to my family:
my Mother, Father and Sister Truc
for their never ending love, encouragement and support*

ACKNOWLEDGEMENTS

Firstly, I would like to thank my advisors, Dr. P. Shiv Halasyamani and Dr. Arnold M. Guloy. I have no doubt in my mind that having two of them as my advisors was a great gift.

To Dr. P. Shiv Halasyamani, words cannot express how grateful I am to him. When I started out my journey at the University of Houston, I had no clues in the field I was entering. I was totally blank and he spent his time out of his tight schedule teaching me. Always, he offered me countless opportunities, not only in our work but also in our collaborations with other research groups internationally, to learn and experience a great deal of valuable lessons. His encouragement, enthusiasm and dedication to science have influenced my thoughts. It is my understanding that I am, at some points, ‘abnormal’. Patiently and nicely, he has drawn me to the way I should be simply by what he did and how he did that. All he has taught me, in and out chemistry, I shall carry along with me for years to come. Also, I would like to thank his entire beautiful family – Shiv, Angela, gorgeous Oliver and Ingrid – for the warm conversations we engaged in every time I had a chance meeting with them.

To Dr. Arnold M. Guloy, I would like to thank you very much for opening up a new direction for my research. His lightheartedness and enthusiasm about our research made me easy to ask questions. He created a relaxed and yet motivating atmosphere to work in. From him, I learned how to approach things systematically. Also I learned how to be

open to new ideas and critical of them at the same time. It is my intention to implement many of these lessons to my independent career.

I would also like to thank the members of my committee, Dr. Bernd Lorenz, Dr. Eric Bittner and Dr. Jakoah Brgoch for their mindful suggestions to my research as well as my dissertation. I am especially thankful to Dr. Bernd Lorenz for his assistance and stimulating discussions in magnetism and transport property. Whenever I got lost, he was the person who was always there to help me out. From him, my background on physics of condensed matters was improved. In addition, I would like to express my deep gratitude to Dr. Jakoah Brgoch and Dr. James M. Rondinelli, Dr. Jiangang He (Northwestern University) for the theoretical calculations, Dr. Kenneth R. Poeppelmeier, Dr. Shichao Wang, Dr. Martin Donakowski (Northwestern University) for assistance in FTIR measurements, Dr. Alexander P. Litvinchuk (Raman scattering), Dr. Melissa Gooch (magnetic and transport measurements). I would also like to thank Dr. James D. Korp and Dr. Xiqu Wang for their assistance and helpful discussions in crystallography. I am grateful to Dr. James Meen and Dr. Karoline Mueller for their training and assistance in SEM/EDS analysis.

A university is not a school at all without students and post-docs, and the University of Houston is one of sharing. Several good friends shared my life of a graduate student in the Halasyamani group: Dr. Weiguo Zhang, Dr. Jeongho Yeon, Dr. Sang-Hwan Kim, Dr. Hongwei Yu, Dr. Sau Nguyen, Dr. Sunwoo Kim, Ilyana Derkach and Philip Ayazi; and the Guloy group: Dr. Zhongjia Tang, Dr. Phuong Doan, Maurice Sorolla, Sean See, John Manongdo and Xin Zhong. I also cannot forget a great time hanging out with Thien Si

Nguyen (and his family), Ha Le, Thien Trong Nguyen, Phong Le, Ha Do, Hung Tran, Yiting Chen, Nui and the other friends I made.

A number of my other colleagues and friends back in Vietnam and all around the world made my stay here more pleasant through their letters, emails and phone calls. They are Dat Dang, Thanh Bui, Nguyen H. Nguyen, Phuc Nguyen, Minh Tran, Nhan Nguyen, Tanh Nguyen and Phuoc Dinh.

I would not be a person who I am now if I did not meet my professor, Ngoc Minh Huynh, back in Ho Chi Minh, Vietnam, more than 12 years ago. He changed my mind to follow inorganic chemistry instead of information technology, which was a ‘hot’ college major back in 2003. This diversion helped me find the person within me. A mentor, he is more than a mentor. A great friend, he is more than a great friend. If someone truly understands me, at both my bad (definitely) and ‘acceptable’ (probably) corners, it is him. The influence he had on me was, and still is, tremendous. There were times where I did not think I could complete my studies, he always stood by my side and walked me through all that. “Follow your heart, everything else is just secondary,” he said to me. Yet, I cannot thank him enough for his belief in me, his constant support in everything I set my heart to and his relentless patience even at the time where I became impossible of being put up with. I understand I could certainly not have gone this far without him.

At last, but definitely not least, my deepest gratitude goes to my parents and my ‘little’ sister Truc for their support, love and encouragement. Without them, I would

probably not have written this dissertation, and even if I had this dissertation done, it would have had no meaning.

This work was supported by the United State Department of Energy – Basis Energy Sciences (DE-SC0005032) and the Welch Foundation (Grant E-1457). Also, it was in part supported by the Welch Foundation (E-1297), the State of Texas through the Texas Center for Superconductivity and the US AFOSR.

**SYNTHESIS AND STRUCTURE-PROPERTY RELATIONSHIPS OF A FEW
FLUORIDE COMPOUNDS: (I) MIXED-METAL FLUOROCARBONATES
AND (II) A REDUCED NIOBIUM OXYFLUORIDE**

An Abstract of a Dissertation

Presented to

the Faculty of the Department of Chemistry

University of Houston

In Partial Fulfillment

of the Requirements for the Degree

Doctor of Philosophy

By

Thanh Thao Tran

May 2015

ABSTRACT

This dissertation focuses on the synthesis and structure-property relationships of new complex metal fluorides of (i) alkaline-metal lead fluorocarbonates, alkaline-metal magnesium fluorocarbonates and (ii) a reduced niobium oxyfluoride. We have designed new structure building units, PbO_6F and PbO_6F_2 , in layered compounds of $\text{KPb}_2(\text{CO}_3)_2\text{F}$ and $\text{K}_{2.70}\text{Pb}_{5.15}(\text{CO}_3)_5\text{F}_3$, that were then developed to three-dimensional noncentrosymmetric RbPbCO_3F and CsPbCO_3F . Powder second-harmonic generation (SHG) measurements on $\text{K}_{2.70}\text{Pb}_{5.15}(\text{CO}_3)_5\text{F}_3$, RbPbCO_3F and CsPbCO_3F using 1064 nm radiation revealed SHG efficiencies of approximately 40, 250 and $300 \times \alpha\text{-SiO}_2$, respectively. The Mg^{2+} substitution of the Pb^{2+} cation in APbCO_3F (A = alkaline-metal) resulted in KMgCO_3F and RbMgCO_3F with unique coordination environments of magnesium, i.e., pentagonal arrangements in the *ab*-plane. These compounds are second-harmonic generation (SHG) phase-matching at both 1064 nm (120 and $160 \times \alpha\text{-SiO}_2$) and 532 nm (0.33 and $0.6 \times \beta\text{-BaB}_2\text{O}_4$) with short UV cut-off edges, below 200 and 190 nm for KMgCO_3F and RbMgCO_3F , respectively. These mixed-metal fluorocarbonates were also characterized by infrared spectroscopy, thermogravimetric and differential thermal analysis. In addition, we report a new highly correlated electron system, $\text{Nb}_2\text{O}_2\text{F}_3$. It is a new low-valent niobium (III/IV) oxyfluoride that features $[\text{Nb}_2\text{X}_{10}]$ units (X = O, F) with short ($2.5739(1)$ Å) Nb-Nb metal-metal bonds. The $[\text{Nb}_2\text{X}_{10}]$ units are connected through shared O/F vertices to form a 3D structure. $\text{Nb}_2\text{O}_2\text{F}_3$ undergoes a structural transition (below 90 K), from a monoclinic to a triclinic structure, which can be described as a

charge ordering or disproportionation of $[\text{Nb}_2]^{7+}$ dimers. That resulted in a doubly bonded ($2.5000(9) \text{ \AA}$) and a singly bonded ($2.6560(9) \text{ \AA}$) Nb_2 dimers. The structural change is associated with unusual field-independent 'spin-gap-like' magnetic and electronic phase transition.

TABLE OF CONTENTS

Chapter 1 General Introduction.....	1
1.1 Related Literature and Scope of the Study	1
1.2 Summary of Chapters	3
1.3 References.....	5
Chapter 2 Theoretical Background.....	7
2.1 Asymmetric Cation Coordination Environment	7
2.2 Functional Properties of Noncentrosymmetric Compounds.....	10
2.2.1 Second-Harmonic Generation (SHG)	11
2.2.2 Piezoelectricity.....	14
2.2.3 Pyroelectricity	15
2.2.4 Ferroelectricity.....	16
2.3 Physical Properties of Strongly Correlated Electron Systems	18
2.3.1 Magnetism.....	18
2.3.2 Mott-Hubbard Physics	21
2.3.3 Charge Order.....	23
2.3.4 Peierls-Instability and Density Waves	25
2.3.5 Electrical Conductivity	28
2.4 References.....	30

Chapter 3 Experiments.....	33
3.1 Synthesis	33
3.1.1 Solid-State Reactions	33
3.1.2 Hydrothermal Techniques.....	34
3.1.3 Flux Method.....	36
3.2 Characterizations.....	37
3.2.1 Single Crystal X-Ray Diffraction	37
3.2.2 Powder X-Ray Diffraction.....	38
3.2.3 Energy-Dispersive X-Ray Spectroscopy(EDS) Analysis.....	39
3.2.4 Thermal Analysis	39
3.2.5 Ultraviolet Visible (UV-Vis) Spectroscopy.....	39
3.2.6 Infrared (IR) Spectroscopy	40
3.2.7 Raman Scattering.....	40
3.3 Physical Property Measurements	41
3.3.1 Second-Harmonic Generation (SHG).....	41
3.3.2 Piezoelectric Measurements	41
3.3.3 Magnetic and Transport Measurements.....	42
3.3.4 Heat Capacity Measurements	42
3.4 Electronic Structure Calculations	42
3.5 References.....	44

Chapter 4 Layered Compounds of Potassium Lead Fluorocarbonates $\text{K}_2\text{Pb}_2(\text{CO}_3)_2\text{F}$ and $\text{K}_{2.70}\text{Pb}_{5.15}(\text{CO}_3)_5\text{F}_3$	45
4.1 Abstract.....	45
4.2 Introduction.....	46
4.3 Experiments	48
4.4 Results and Discussion	53
4.4.1 Structures	53
4.4.2 Infrared (IR) Spectroscopy	63
4.4.3 UV-Vis Diffuse Reflectance Spectroscopy	65
4.4.4 Thermal Analysis	67
4.4.5 Second-Harmonic Generation (SHG) and Piezoelectric Measurements	69
4.5 Conclusions.....	71
4.6 References.....	73
Chapter 5 Three-Dimensional Lead Fluorocarbonates RbPbCO_3F and CsPbCO_3F Exhibiting Large SHG Responses	79
5.1 Abstract.....	79
5.2 Introduction.....	80
5.3 Results and Discussion	82
5.3.1 Structures	82
5.3.2 Infrared (IR) Spectroscopy	93
5.3.3 UV-Vis Diffuse Reflectance Spectroscopy	95

5.3.4 Thermal Analysis	97
5.3.5 Second-Harmonic Generation (SHG) and Piezoelectric Measurements	99
5.3.6 Electronic Structure	102
5.4 Relationship between Electronic Structure, NCS Structures and Acentric Crystal Properties	103
5.5 Conclusions.....	111
5.6 References.....	112
Chapter 6 Deep Ultra-Violet Nonlinear Optical Alkali-Metal Magnesium Fluorocarbonates KMgCO_3F and RbMgCO_3F.....	119
6.1 Abstract.....	119
6.2 Introduction.....	120
6.3 Results and Discussion	122
6.3.1 Structures	122
6.3.2 Infrared (IR) Spectroscopy	135
6.3.3 UV-Vis Transmission Spectroscopy.....	137
6.3.4 Thermal Analysis	138
6.3.5 Second-Harmonic Generation (SHG) and Piezoelectric Measurements	140
6.3.6 Electronic Structure	144
6.4 Relationship between Electronic Structure, NCS Structures and Acentric Crystal Properties	145
6.5 Conclusions.....	148

6.6 References.....	149
Chapter 7 A Reduced Niobium (III/IV) Oxyfluoride Nb₂O₂F₃	153
7.1 Abstract.....	153
7.2 Introduction.....	154
7.3 Experiments	155
7.4 Results and Discussion	161
7.4.1 Structures	161
7.4.2 Energy-Dispersive X-Ray Spectroscopy (EDS) Analysis	163
7.4.3 Magnetic Properties	163
7.4.4 Transport Properties.....	168
7.4.5 Raman Scattering, Structural and Magnetic Phase Transition.....	169
7.4.6 Electronic Structure	172
7.5 Conclusions.....	174
7.6 References.....	175
Chapter 8 Concluding Remarks	178

FIGURES

Chapter 2 Theoretical Background

- Figure 2.1** A general molecular orbital diagram for octahedrally coordinated d^0 cations8
- Figure 2.2** Walsh diagram for pyramidalization in PH_3 . Note the break in the energy scale.....9
- Figure 2.3** Functional properties with respect to noncentrosymmetry10
- Figure 2.4** Examples of type I phase-matching (KDP, KTP and LiNbO_3) and non-phase-matching ($\alpha\text{-SiO}_2$ and BaTiO_3) materials13
- Figure 2.5** Example of displacement vs. applied voltage loop in $\text{K}_{2.70}\text{Pb}_{5.15}(\text{CO}_3)_5\text{F}_3$...14
- Figure 2.6** Example of polarization and pyroelectric coefficient of KH_2PO_415
- Figure 2.7** Example of ferroelectric hysteresis loop of BaTiO_3 16
- Figure 2.8** (a) Typical curves of the temperature dependence of magnetic susceptibility for paramagnetic (PM), ferromagnetic (FM), antiferromagnetic (AFM) and diamagnetic (DM) materials. (b) Illustration of the Curie-Weiss law; the inverse susceptibility is a linear function of temperature and the intercept with the x -axis gives the Weiss temperature θ20
- Figure 2.9** Charge order on a two dimensional Wigner crystal.....23
- Figure 2.10** Left: a metal with a homogeneous charge distribution, $\rho = \text{const}$ and a conduction band filled up to the Fermi energy. Right: The charge modulation with a wavelength π/k_F changes periodicity and thus reduces the

Brillouin zone, producing a gap at $\pm k_F$. The energy of the filled portion of the band is lowered and the system becomes insulating.....25

Figure 2.11 The charge and spin density distributions in the metallic (M), spin density wave (SDW), charge density wave (CDW) and bond density wave (BDW) states.....27

Figure 2.12 Schematic illustrations of the band structure in different types of materials. The classification is based on the band gap between valence band (blue) and conduction band (white).28

Chapter 4 Layered Compounds of Potassium Lead Fluorocarbonates $\text{KPb}_2(\text{CO}_3)_2\text{F}$ and $\text{K}_{2.70}\text{Pb}_{5.15}(\text{CO}_3)_5\text{F}_3$

Figure 4.1 Ball-and-stick representation of a single $\text{Pb}(\text{CO}_3)$ layer in the *ab*-plane and the K^+ cations beneath this layer (a). Ball-and-stick representations of $\text{KPb}_2(\text{CO}_3)_2\text{F}$ in the *bc*-plane (b). Note that the double-layers are staggered to possibly minimize lone-pair –lone-pair interactions.54

Figure 4.2 Ball-and-stick (a) and polyhedral (b) representations of $\text{K}_{2.70}\text{Pb}_{5.15}(\text{CO}_3)_5\text{F}_3$ in the *bc*-plane. Only one position of the disordered bridging fluoride in the triple layer is shown.56

Figure 4.3 ORTEP (50% probability ellipsoids) diagrams of $\text{KPb}_2(\text{CO}_3)_2\text{F}$ and $\text{K}_{2.70}\text{Pb}_{5.15}(\text{CO}_3)_5\text{F}_3$57

Figure 4.4 Ball-and-stick representation of (a) the double-layer unit consisting of two PbO_6F distorted hexagonal pyramids and (b) the triple-layer unit consisting

	of two PbO_6F distorted hexagonal pyramids alternating with one PbO_6F_2 distorted hexagonal bipyramid.....	59
Figure 4.5	ELF diagram, $\eta = 0.5$, of the double-layer in $\text{KPb}_2(\text{CO}_3)_2\text{F}$ (left) and the triple-layer in $\text{K}_{2.70}\text{Pb}_{5.15}(\text{CO}_3)_5\text{F}_3$ (right). Note that the central Pb^{2+} cation has an inert lone-pair, whereas the ‘capping’ Pb^{2+} cations exhibit a stereo-active lone-pair.....	60
Figure 4.6	IR spectra of $\text{KPb}_2(\text{CO}_3)_2\text{F}$ and $\text{K}_{2.70}\text{Pb}_{5.15}(\text{CO}_3)_5\text{F}_3$	64
Figure 4.7	UV-Vis diffuse reflectance spectra of $\text{KPb}_2(\text{CO}_3)_2\text{F}$ and $\text{K}_{2.70}\text{Pb}_{5.15}(\text{CO}_3)_5\text{F}_3$	66
Figure 4.8	Thermogravimetric analysis and differential thermal analysis diagram of $\text{KPb}_2(\text{CO}_3)_2\text{F}$ and $\text{K}_{2.70}\text{Pb}_{5.15}(\text{CO}_3)_5\text{F}_3$ under N_2	68
Figure 4.9	Powder second-harmonic generation for $\text{K}_{2.70}\text{Pb}_{5.15}(\text{CO}_3)_5\text{F}_3$. A curve is drawn to guide the eye and is not a fit to the data.....	69
Figure 4.10	Displacement vs. applied voltage for $\text{K}_{2.70}\text{Pb}_{5.15}(\text{CO}_3)_5\text{F}_3$	70
Chapter 5 Three-Dimensional Lead Fluorocarbonates RbPbCO_3F and CsPbCO_3F Exhibiting Large SHG Responses		
Figure 5.1	Ball-and-stick in the <i>ab</i> -plane (a), and polyhedral in the <i>bc</i> -plane (b) representations of RbPbCO_3F . Only one position of the disordered bridging fluoride in the structure is shown.....	86

Figure 5.2	ORTEP (50% probability ellipsoids) diagrams of RbPbCO ₃ F and CsPbCO ₃ F. Note that the F atoms, which were refined to be disordered, have well-behaved thermal parameters.....	87
Figure 5.3	Ball-and-stick in the <i>ab</i> -plane (a) and polyhedral in the <i>bc</i> -plane (b) representations of CsPbCO ₃ F. Only one position of the disordered bridging fluoride in the structure is shown.....	90
Figure 5.4	IR spectra of RbPbCO ₃ F and CsPbCO ₃ F	94
Figure 5.5	UV-Vis diffuse reflectance spectra of RbPbCO ₃ F and CsPbCO ₃ F	96
Figure 5.6	Thermogravimetric analysis and differential thermal analysis diagram of RbPbCO ₃ F and CsPbCO ₃ F under N ₂	98
Figure 5.7	Powder second-harmonic generation for RbPbCO ₃ F and CsPbCO ₃ F. Curves are drawn to guide the eye and are not a fit to the data.	100
Figure 5.8	Displacement vs. applied voltage for RbPbCO ₃ F and CsPbCO ₃ F	101
Figure 5.9	The electronic densities of states (DOS) for RbPbCO ₃ F and CsPbCO ₃ F decomposed by atomic site and orbital contributions.....	102
Figure 5.10	Reuleaux triangle projection overlaid on charge density contours of the ELF in the (001) plane about the Pb site in RbPbCO ₃ F. ELF plot in the ($\bar{1}20$) plane corresponding to a planar slice along the [210] direction intersecting the “vertex” of the Reuleaux triangle. The red, silver, brown, maroon spheres correspond to oxygen, fluorine, carbon, and lead atoms, respectively.	104

Figure 5.11 (a) Relationship between the alkali metal and divalent cations in three-dimensional fluorocarbonates and the specific acentric-mode displacements (SAMD). All structures exhibit the D_{3h} point symmetry, with the different symbols (colors) corresponding to compounds with $Z=1$ (circles, red) or $Z=3$ (squares, blue) separated by a vertical bar (gradient). The grey line is a linear least squares fit to the data ($R=0.82$). Insets depict the $[\text{CO}_3]^{2-}$ topology, other atoms omitted for clarity. SHG efficiency for the same compounds relative to (b) the total SAMD and (c) the projection of SAMD onto the $(2\bar{1}0)$ plane.108

Chapter 6 Deep Ultra-Violet Nonlinear Optical Alkali-Metal Magnesium Fluorocarbonates KMgCO_3F and RbMgCO_3F

Figure 6.1 Ball-and-stick in the ab -plane (a), and polyhedral in the bc -plane (b) representations of KMgCO_3F . Only one position of the disordered $[\text{CO}_3]^{2-}$ in the structure is shown.....128

Figure 6.2 Ball-and-stick in the ab -plane (a), and polyhedral in the bc -plane (b) representations of RbMgCO_3F . In (a) note that the Rb cations reside in pentagonal tunnels created by the Mg polyhedra. In (b) note that the Mg polyhedra are connected by bridging fluorine atoms.....129

Figure 6.3 ORTEP (50% ellipsoid probability) diagrams for KMgCO_3F and RbMgCO_3F . Note that only one position of the disordered $[\text{C}(1)\text{O}(1)_3]$ in KMgCO_3F is shown.....131

Figure 6.4	Different coordination denticities for B^{2+} cations ($B = \text{Mg, Ca, Sr}$) in $ABC\text{O}_3\text{F}$ materials ($A = \text{K, Rb, Cs}$). Note that unique to Mg^{2+} cation, two monodentate and one bidentate linkages are observed.	133
Figure 6.5	IR spectra of KMgCO_3F and RbMgCO_3F	136
Figure 6.6	UV-Vis transmission spectra of KMgCO_3F and RbMgCO_3F . The ‘spike’ at ~ 800 nm is artifact attributable to the detector change.	137
Figure 6.7	Thermogravimetric analysis and differential thermal analysis diagram of KMgCO_3F and RbMgCO_3F under N_2	139
Figure 6.8	Powder second-harmonic generation for KMgCO_3F and RbMgCO_3F at 1064 nm incident radiation. Curves are drawn to guide the eye, are not a fit to the data.	141
Figure 6.9	Powder second-harmonic generation for KMgCO_3F and RbMgCO_3F at 532 nm incident radiation. Curves are drawn to guide the eye, are not a fit to the data.	142
Figure 6.10	Displacement vs. applied voltage for KMgCO_3F and RbMgCO_3F	143
Figure 6.11	DOS for RbMgCO_3F decomposed by atomic site and orbital contributions. O(1) and O(2) correspond to Mg ligands which bond to monodentate and bidentate $[\text{CO}_3]^{2-}$ groups, respectively.....	144
Figure 6.12	Effect of Rb and B cation variance on the carbonate linkage in RbBCO_3F fluorocarbonates. The density of acentric displacements as parameterized in the SAMD value (see text) increases with the change in bonding of the B^{2+} cation with the carbonate group (top). The SHG response is anti-correlated	

with the cation variance for two and three bidentate carbonate groups (bottom), whereas the behaviour of RbMgCO_3F is found to be an outlier owing to reduced polarizable charge density in response to an electric-field. The inset depicts charge-density contours of the ELF in the (001) plane about the Mg site with the static asymmetry greater than that found for the other compounds. The Reuleaux triangle construction is highlighted and because of the bonding environment should be puckered (no longer regular) along the vertical direction indicated by the (blue) arrow.146

Chapter 7 A Reduced Niobium (III/IV) Oxyfluoride $\text{Nb}_2\text{O}_2\text{F}_3$

- Figure 7.1** ORTEP representation of the crystal structures of (a) monoclinic (M)- $\text{Nb}_2\text{O}_2\text{F}_3$ and (b) triclinic (T)- $\text{Nb}_2\text{O}_2\text{F}_3$. Ellipsoids are drawn at 90% probability.162
- Figure 7.2** (a) Magnetic susceptibility (χ) of $\text{Nb}_2\text{O}_2\text{F}_3$ upon field-cooling (FC) and field-warming (FW), $T = 2 - 150$ K, $H = 1000$ Oe; (b) the reciprocal of magnetic susceptibility ($\chi - \chi_0$) of $\text{Nb}_2\text{O}_2\text{F}_3$ as a function of temperature ($T > 90$ K), $H = 1$ T164
- Figure 7.3** Temperature dependence (2 K to 150 K) of heat capacity (C_p) of $\text{Nb}_2\text{O}_2\text{F}_3$ in the vicinity of the phase transitions166
- Figure 7.4** Time dependence (0 to 6000 seconds) of the magnetization of $\text{Nb}_2\text{O}_2\text{F}_3$ at 80, 75, 70, 55 and 45 K (T). The temperature was decreased very fast from 110 K to T K where the measurements were performed.167

Figure 7.5	Temperature dependence (5 to 100 K) of the magnetization of Nb ₂ O ₂ F ₃ after the relaxation.....	168
Figure 7.6	Plot of resistivity (ρ) of Nb ₂ O ₂ F ₃ as a function of temperature (T = 80 – 300 K). Inset: plot of ln(R) vs. 1/T	169
Figure 7.7	Raman scattering spectra of Nb ₂ O ₂ F ₃ at 295, 70 and 8 K. Note that the changes occur below 80 K (at 70 K).....	170
Figure 7.8	Temperature dependence (T = 8–295 K) of the frequencies of selected Raman-active modes of Nb ₂ O ₂ F ₃ . The phase transition below 90K is indicated by a dashed line.	171
Figure 7.9	The density of states (DOS) of (a) monoclinic (M)-Nb ₂ O ₂ F ₃ with the partial DOS for the Nb ₂ ⁷⁺ dimers and (b) the triclinic (T)-Nb ₂ O ₂ F ₃ with the partial DOS of the single bond Nb ₂ ⁸⁺ and double bond Nb ₂ ⁶⁺ shown. The respective Fermi levels (E _F) are set at 0 eV	173

TABLES

Chapter 3 Experiments

Table 3.1	Solid-state reactions for synthesizing $\text{KPb}_2(\text{CO}_3)_2\text{F}$, $\text{K}_{2.70}\text{Pb}_{5.15}(\text{CO}_3)_5\text{F}_3$, RbPbCO_3F , CsPbCO_3F , KMgCO_3F and RbMgCO_3F	34
Table 3.2	Hydrothermal reactions for growing crystals of $\text{KPb}_2(\text{CO}_3)_2\text{F}$, $\text{K}_{2.70}\text{Pb}_{5.15}(\text{CO}_3)_5\text{F}_3$, RbPbCO_3F , CsPbCO_3F , KMgCO_3F and RbMgCO_3F	35
Table 3.3	Details of single-crystal X-ray diffraction experiments for $\text{KPb}_2(\text{CO}_3)_2\text{F}$, $\text{K}_{2.70}\text{Pb}_{5.15}(\text{CO}_3)_5\text{F}_3$, RbPbCO_3F , CsPbCO_3F , KMgCO_3F , RbMgCO_3F and $\text{Nb}_2\text{O}_2\text{F}_3$	38

Chapter 4 Layered Compounds of Potassium Lead Fluorocarbonates $\text{KPb}_2(\text{CO}_3)_2\text{F}$ and $\text{K}_{2.70}\text{Pb}_{5.15}(\text{CO}_3)_5\text{F}_3$

Table 4.1	Crystallographic data for $\text{KPb}_2(\text{CO}_3)_2\text{F}$ and $\text{K}_{2.70}\text{Pb}_{5.15}(\text{CO}_3)_5\text{F}_3$	50
Table 4.2	Selected bond distances (Å) and angles (deg) for $\text{KPb}_2(\text{CO}_3)_2\text{F}$ and $\text{K}_{2.70}\text{Pb}_{5.15}(\text{CO}_3)_5\text{F}_3$	51
Table 4.3	Atomic coordinates and equivalent isotropic displacement parameters (Å ²) for $\text{KPb}_2(\text{CO}_3)_2\text{F}$	52
Table 4.4	Atomic coordinates and equivalent isotropic displacement parameters (Å ²) for $\text{K}_{2.70}\text{Pb}_{5.15}(\text{CO}_3)_5\text{F}_3$	52
Table 4.5	Bond valence analysis for $\text{KPb}_2(\text{CO}_3)_2\text{F}$ and $\text{K}_{2.70}\text{Pb}_{5.15}(\text{CO}_3)_5\text{F}_3$	62

Chapter 5 Three-Dimensional Lead Fluorocarbonates RbPbCO₃F and CsPbCO₃F Exhibiting Large SHG Responses

Table 5.1	Crystallographic data for RbPbCO ₃ F and CsPbCO ₃ F.....	84
Table 5.2	Selected bond distances (Å) and angles (deg) for RbPbCO ₃ F and CsPbCO ₃ F.....	85
Table 5.3	Atomic coordinates and equivalent isotropic displacement parameters (Å ²) for RbPbCO ₃ F	85
Table 5.4	Atomic coordinates and equivalent isotropic displacement parameters (Å ²) for CsPbCO ₃ F	85
Table 5.5	Bond valence analysis for RbPbCO ₃ F and CsPbCO ₃ F.....	92
Table 5.6	Born effective charges of RbPbCO ₃ F and CsPbCO ₃ F in units of electrons	105
Table 5.7	Summary of A-M-CO ₃ -F (A = Na, K, Rb or Cs) compounds.....	110

Chapter 6 Deep Ultra-Violet Nonlinear Optical Alkali-Metal Magnesium Fluorocarbonates KMgCO₃F and RbMgCO₃F

Table 6.1	Crystallographic data for KMgCO ₃ F and RbMgCO ₃ F.....	123
Table 6.2	Selected bond distances (Å) and angles (deg) for KMgCO ₃ F and RbMgCO ₃ F	124
Table 6.3	Atomic coordinates and equivalent isotropic displacement parameters (Å ²) for KMgCO ₃ F	125

Table 6.4	Atomic coordinates and equivalent isotropic displacement parameters (\AA^2) for RbMgCO_3F	125
Table 6.5	Bond valence analysis for KMgCO_3F and RbMgCO_3F	134
Chapter 7	A Reduced Niobium (III/IV) Oxyfluoride $\text{Nb}_2\text{O}_2\text{F}_3$	
Table 7.1	Crystallographic data for monoclinic (M)- $\text{Nb}_2\text{O}_2\text{F}_3$ and triclinic (T)- $\text{Nb}_2\text{O}_2\text{F}_3$	157
Table 7.2	Selected bond distances (\AA) and angles (deg) for monoclinic (M)- $\text{Nb}_2\text{O}_2\text{F}_3$ and triclinic (T)- $\text{Nb}_2\text{O}_2\text{F}_3$ (X = O/F)	158
Table 7.3	Atomic coordinates and equivalent isotropic displacement parameters (\AA^2) for monoclinic (M)- $\text{Nb}_2\text{O}_2\text{F}_3$ ($I2/a$) (X = O/F)	159
Table 7.4	Atomic coordinates and equivalent isotropic displacement parameters (\AA^2) for monoclinic (T)- $\text{Nb}_2\text{O}_2\text{F}_3$ (X = O/F)	149
Table 7.5	Bond valence analysis for monoclinic (M)- $\text{Nb}_2\text{O}_2\text{F}_3$ and (T)- $\text{Nb}_2\text{O}_2\text{F}_3$	160

ABBREVIATIONS

AFM	Antiferromagnetic
BVS	Bond Valence Sum
CBM	Conduction Band Minimum
CCD	Charge Coupled Device
CDW	Charge Density Wave
CO	Charge Ordering
CS	Centrosymmetric
COHP	Crystal Orbital Hamilton Population
DFT	Density Functional Theory
DM	Diamagnetic
DOS	Density of States
DTA	Differential Thermal Analysis
DUV	Deep Ultra-Violet
EDS	Energy-Dispersive X-ray Spectroscopy
ELF	Electron Localization Function
FM	Ferromagnetic
HOMO	Highest Occupied Molecular Orbital
IR	Infrared
KDP	KH_2PO_4 Potassium Dihydrogen Phosphate
LUMO	Lowest Unoccupied Molecular Orbital

MPMS	Magnetic Property Measurement System
NCS	Noncentrosymmetric
NLO	Nonlinear Optical
PAW	Project Augmented Wave
PBE	Perdew–Burke–Ernzerhof
PM	Paramagnetic
PPMS	Physical Property Measurement System
PXRD	Powder X-Ray Diffraction
SAMD	Specific Acentric-Mode Displacements
SDW	Spin Density Wave
SHG	Second-Harmonic Generation
SOJT	Second-Order Jahn Teller
XRD	X-Ray Diffraction
TGA	Thermogravimetric Analysis
UV-Vis	Ultra-Violet Visible
VASP	Vienna ab initio Simulation Package
VB	Valence Band
VBM	Valence Band Maximum

Chapter 1 General Introduction

This chapter contains a broad introduction into the compounds that will be discussed in this dissertation. A more detailed and specific introduction is also provided at the beginning of each chapter.

1.1 Related Literature and Scope of the Study

The design and synthesis of new materials with desired and tunable physical properties continue to be a major goal of synthetic chemists. Solid-state materials are of academic and technological interests attributable to the relevant functionalities including electronic, optical, magnetic, and Mott insulating properties. New compounds provide the foundation while the structure-property correlations contribute the framework to understand and exploit existing materials in emerging technologies. The range of applications of these materials is potentially as infinite and rich as their physical properties are. Yet, the design and synthesis of solid-state materials still remains an ongoing challenge. This dissertation was motivated by the synthesis and structure-property relationships of (i) nonlinear optical materials and (ii) highly correlated electron systems.

The nonlinear optical (NLO) compounds have been of interest attributable to the technological applications in laser science and photonic technology.¹⁻² A number of strategies to the synthesis of new noncentrosymmetric (NCS) materials have been reported,³⁻⁹ but NCS crystal design still remains difficult. NCS crystal engineering is

challenging because it involves multiple effects, such as steric hindrance, attraction or repulsion, that also occur in the formation of centrosymmetric structures. It is necessary for the inorganic-materials community to develop new strategies to create NCS materials and obtain desired functional properties. Fluorocarbonates have attracted considerable attention over the last ten years attributable to their polarizability.¹⁰⁻¹⁴ The large difference in polarizability between the carbonate group with a π -conjugated system and the isotropic fluoride ion could give rise to the formation of a macroscopically polar material. A few NCS fluorocarbonates have been reported.¹⁰⁻¹⁴ We were interested in investigating the association of mixed-metal and fluoride carbonate anions to the formation of new NCS materials.

Strongly correlated electron systems provide a foundation for diverse physics such as charge density wave (CDW), Mott insulator, and superconductivity. Low-dimensional metallic compounds are susceptible to electronic instabilities of the systems, that gives rise to a modulation of long-range order of spins or charges,¹⁵⁻¹⁶ and opens up new opportunities in a field of material engineering. On the basis of intrinsic physical behaviors, the compounds of niobium in low oxidation states have been of significant interest. There has been limited success to create and grow crystals of reduced niobium oxides/oxyfluorides using solid-state reactions from appropriate mixtures of Nb-based starting materials at very high temperatures, above 1300 K. Often the result is unintended changes to the highest oxidation state of Nb(V) and compositions of the products.¹⁷ A few low-valent niobates have been reported.¹⁸⁻²⁰ We also were motivated to study reduced niobium oxyfluorides, their diverse physics of charge density wave, Mott-

Hubbard insulating and magnetic properties, and possibilities for unconventional superconductors.

Given the dissimilarity of the two aforementioned material classes, it is necessary to find appropriate and accessible synthesis for each particular type of compounds. In addition, the correlations between crystal structures and physical properties of these materials were investigated. The foci of this dissertation are the synthesis and the structure-property relationships of (i) alkaline-metal lead fluorocarbonates, alkaline-metal magnesium fluorocarbonates – NLO materials and (ii) a reduced niobium (III/IV) oxyfluoride – highly correlated electron systems.

1.2 Summary of Chapters

The theoretical background of asymmetric cation coordination environment and physical properties used in this study, namely, (i) SHG, piezoelectricity, ferroelectricity and pyroelectricity and (ii) magnetism, Mott insulator, charge ordering (CDW), electrical conductivity, are presented in Chapter 2.

Chapter 3 presents the details of the experimental synthesis, characterizations and measurements for physical properties and theoretical calculations. The synthetic procedures involve conventional solid-state, hydrothermal and flux methods. The characterization involves single crystal X-ray diffraction, powder X-ray diffraction, thermal analysis, ultraviolet-visible (UV-Vis), infrared (IR) and Raman scattering spectroscopy. The physical properties include SHG, piezoelectricity, magnetic behavior, heat capacity and transport property.

In Chapter 4, two new layered compounds of potassium lead fluorocarbonates, $\text{K}\text{Pb}_2(\text{CO}_3)_2\text{F}$ and $\text{K}_{2.70}\text{Pb}_{5.15}(\text{CO}_3)_5\text{F}_3$, are discussed. Their synthesis, structures and functional properties are presented.

Chapter 5 extends new structural building units presented in Chapter 4 to three-dimensional compounds of rubidium (or cesium) lead fluorocarbonates – APbCO_3F (A = Rb or Cs) – with large SHG responses. The preparation, crystal architecture and functional properties are discussed.

In line with the enhanced SHG results discussed in Chapter 5, Chapter 6 takes NLO applications further to deep-UV noncentrosymmetric materials with two new potassium (or rubidium) magnesium fluorocarbonates – AMgCO_3F (A = K or Rb). Their synthesis, unique structures and functional properties are presented.

Chapter 7 features a new direction for the study in strongly correlated systems by presenting the results and understanding of a reduced niobium (III/IV) oxyfluoride – $\text{Nb}_2\text{O}_2\text{F}_3$. Discussed in detail are the synthetic aspects, crystal structures, magnetic and transport properties and electronic structure of the compound.

Chapter 8 summarizes overall results discussed in Chapter 4–7 and provides concluding remarks.

1.3 References

- (1) Mao, J.; Sun, C.; Hu, T.; Yang, B.; Pacificchem 2010. *International Chemical Congress of Pacific Basin Societies*, Honolulu HI, Dec 15 - 20, 2010; American Chemical Society: 2010, p INOR-558.
- (2) Wu, H.; Yu, H.; Yang, Z.; Hou, X.; Su, X.; Pan, S.; Poepelmeier, K. R.; Rondinelli, J. M. *J. Am. Chem. Soc.* **2013**, *135*, 4215.
- (3) Zhang, G.; Qin, J.; Liu, T.; Li, Y.; Wu, Y.; Chen, C. *Appl. Phys. Lett.* **2009**, *95*, 261104/1.
- (4) Wang, S.; Ye, N.; Li, W.; Zhao, D. *J. Am. Chem. Soc.* **2010**, *132*, 8779.
- (5) Gautier, R.; Norquist, A. J.; Poepelmeier, K. R. *Cryst. Growth Des.* **2012**, *12*, 6267.
- (6) Donakowski, M. D.; Gautier, R.; Yeon, J.; Moore, D. T.; Nino, J. C.; Halasyamani, P. S.; Poepelmeier, K. R. *J. Am. Chem. Soc.* **2012**, *134*, 7679.
- (7) Lu, H.; Gautier, R.; Donakowski, M. D.; Tran, T. T.; Edwards, B. W.; Nino, J. C.; Halasyamani, P. S.; Liu, Z.; Poepelmeier, K. R. *J. Am. Chem. Soc.* **2013**, *135*, 11942.
- (8) Wu, H.; Yu, H.; Yang, Z.; Hou, X.; Su, X.; Pan, S.; Poepelmeier, K. R.; Rondinelli, J. M. *J. Am. Chem. Soc.* **2013**, *135*, 4215.
- (9) Wu, H.; Pan, S.; Poepelmeier, K. R.; Li, H.; Jia, D.; Chen, Z.; Fan, X.; Yang, Y.; Rondinelli, J. M.; Luo, H. *J. Am. Chem. Soc.* **2011**, *133*, 7786.
- (10) Zou, G.; Ye, N.; Huang, L.; Lin, X. *J. Am. Chem. Soc.* **2011**, *133*, 20001.
- (11) Grice, J. D.; Maisonneuve, V.; Leblanc, M. *Chem. Rev.* **2007**, *107*, 114.

- (12) Ben, A. A.; Kodjikian, S.; Maisonneuve, V.; Leblanc, M. *Solid State Sci.* **2006**, *8*, 1322.
- (13) Ben, A. A.; Maisonneuve, V.; Smiri, L. S.; Leblanc, M. *Solid State Sci.* **2002**, *4*, 891.
- (14) Sun, Y. P.; Huang, Q. Z.; Wu, L.; He, M.; Chen, X. L. *J. Alloys Compd.* **2006**, *417*, 13.
- (15) Canadell, E.; Whangbo, M. H. *Chem. Rev.* **1991**, *91*, 965.
- (16) Si, Q.; Steglich, F. *Science* **2010**, *329*, 1161.
- (17) Koehler, J.; Svensson, G.; Simon, A. *Angew. Chem.* **1992**, *104*, 1463.
- (18) Geselbracht, M. J.; Richardson, T. J.; Stacy, A. M. *Nature* **1990**, *345*, 324.
- (19) Koehler, J.; Simon, A. *Z. Anorg. Allg. Chem.* **1989**, *572*, 7.
- (20) Cava, R. J.; Batlogg, B.; Krajewski, J. J.; Gammel, P.; Poulsen, H. F.; Peck, W. F., Jr.; Rupp, L. W., Jr. *Nature* **1991**, *350*, 598.

Chapter 2 Theoretical Background

2.1 Asymmetric Cation Coordination Environment

A number of approaches to the synthesis of new noncentrosymmetric materials have been reported.¹⁻⁴ We have focused on designing noncentrosymmetric materials by using cations susceptible to the second-order Jahn Teller (SOJT) distortions – asymmetric cation coordination environments.⁵⁻⁷ The SOJT effect is associated with the changes in structures attributable to a nondegenerate ground-state mixing with a low-energy excited state, the first-order Jahn Teller, on the other hand, is related with molecular distortions owing to degenerate electronic ground states.⁸⁻⁹ With respect to SOJT, a distortion occurs when the energy gap between the highest occupied molecular orbital (HOMO) and the lowest unoccupied molecular orbital (LUMO) is narrow and the symmetry allows for a distortion owing to interaction between the HOMO and LUMO states.^{8,10-13} If the HOMO and LUMO, for instance, have *a* and *e* symmetry, respectively, and the gap between the two orbitals is narrow, the LUMO (*e*) will be separated into *a* and *b* orbitals and the HOMO *a* will be interacted with the LUMO *a*. That lowers the energy and thus stabilizes the system (see Figure 2.1–2.2).

For d^0 octahedrally coordinated transition metal cations (e.g. Ti^{4+} , Nb^{5+} , Ta^{5+}), the interaction between the HOMO and LUMO is allowed in symmetry (see Figure 2.1) and the degree of mixing of the HOMO-LUMO has a tendency to increase with the ratio of charge to radius of the cations.¹⁰⁻¹¹ The d^0 cations in octahedral coordination environment can distort in three manners: (i) along the C_4 , (ii) along the C_2 or (iii) along the C_3 axis.¹³

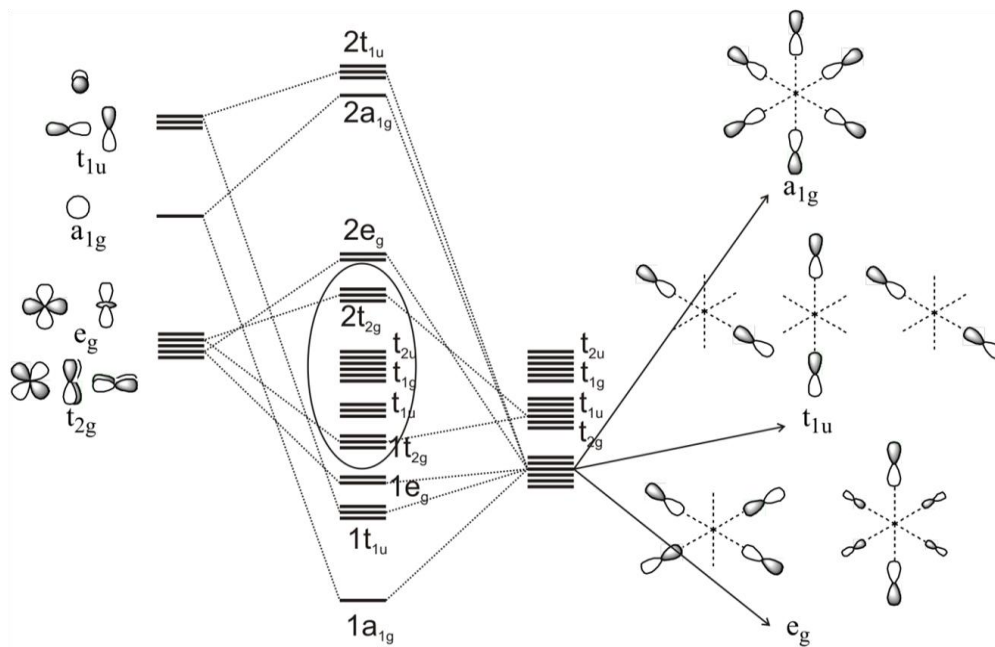


Figure 2.1 A general molecular orbital diagram for octahedrally coordinated d^0 cations¹²

With respect to the cations with non-bonded (s^2) electron pairs (e.g., P^{3+} , Sn^{2+} , Sb^{3+} , Te^{4+}), the Walsh diagram can be used to elucidate the distorted coordination environments.¹⁴⁻¹⁶ A three-coordinated P^{3+} cation in PH_3 , for example, might be expected to be in trigonal planar symmetry (D_{3h}) (see Figure 2.2).¹⁷ In this symmetry, however, a strong antibonding HOMO a_1^* is composed of the s^2 electron pair. As such, a distortion occurs to trigonal pyramidal symmetry (C_{3v}), that lowers the energy of the HOMO by interacting with the LUMO p-orbital (s - p mixing). As a result, the system is stabilized in energy and the electron lone pair becomes stereo-active.

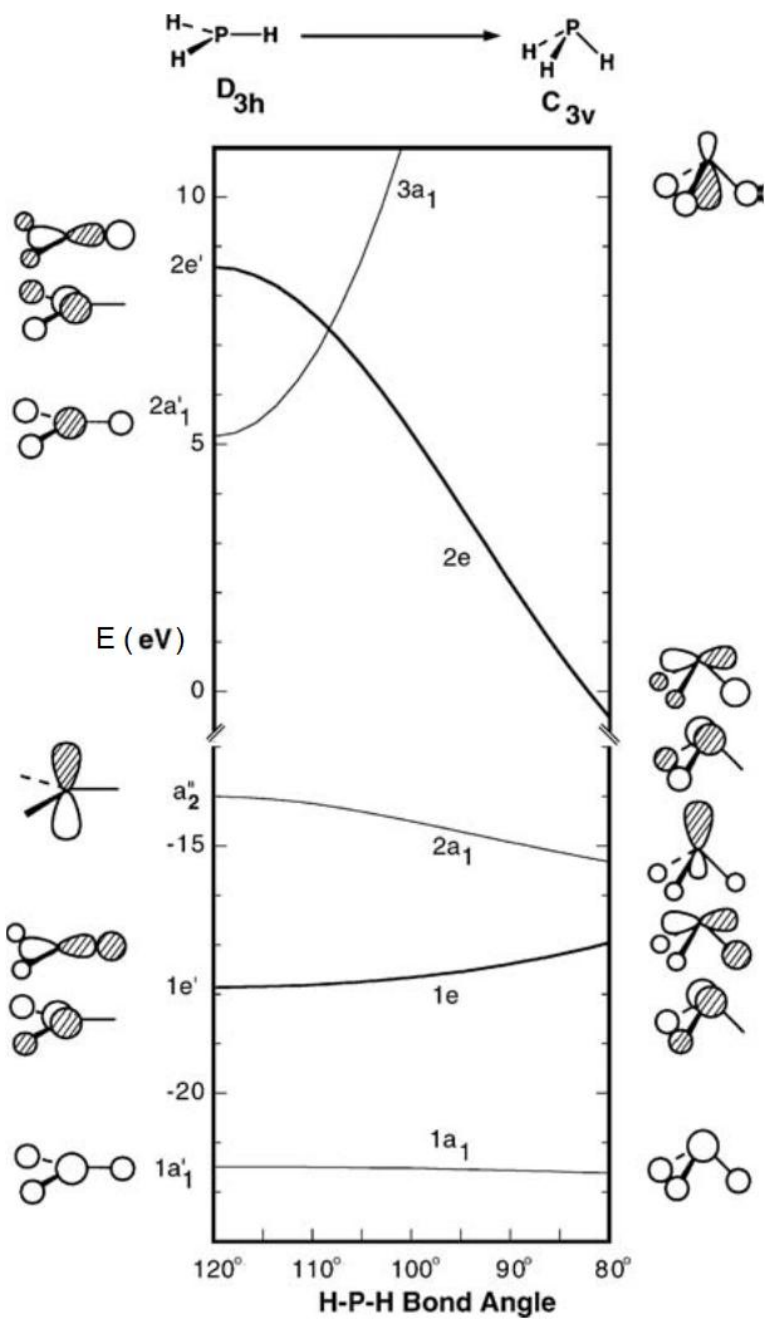


Figure 2.2 Walsh diagram for pyramidalization in PH_3 . Note the break in the energy scale¹⁷

2.2 Functional Properties of Noncentrosymmetric Compounds

Noncentrosymmetric (NCS) materials, which lack an inversion symmetry in their crystal structures, are of interest attributable to their structural chemistry as well as applications in important technologies. The functional properties include second-harmonic generation (SHG), piezoelectric, pyroelectric and ferroelectric-based systems.¹⁸⁻²¹ Polar compounds, that exhibit a dipole moment, is a subset of noncentrosymmetric materials. A compound is considered polar only if it crystallizes in one of the ten polar crystal classes: 1, 2, 3, 4, 6, m, mm2, 3m, 4mm or 6mm. A diagram depicting the relationship between acentric crystal classes and physical properties are presented as follows:²²

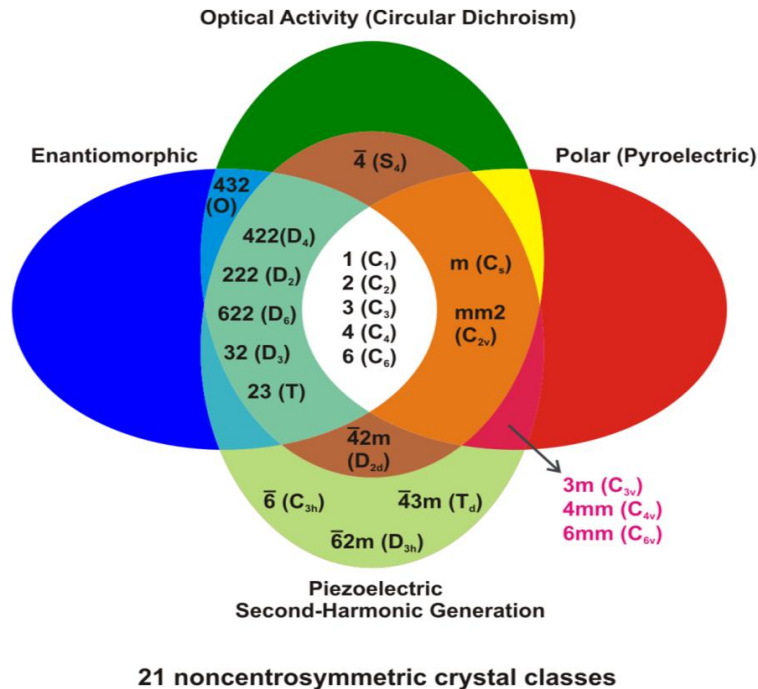


Figure 2.3 Functional properties with respect to noncentrosymmetry²³

2.2.1 Second-Harmonic Generation (SHG)

An electric field from a light source interacts with the molecule to induce a dipole, μ , proportional to the strength of the electric field E . The equation may be written as:

$$\mu = \mu_0 + \alpha E \quad (2-1)$$

where μ_0 is the static dipole of the material and α is the polarizability of the electrons in the molecule. For condensed materials, it is necessary to take into account the bulk polarization. The static polarization is observed in a few materials and the induced polarization is given as the equation follows:

$$P = \epsilon_0 \chi^{(1)} E \quad (2-2)$$

where $\chi^{(1)}$ is the linear susceptibility, i.e., a macroscopic average of the polarizability, and ϵ_0 is the permittivity in vacuum.²⁴

The development of high intensity lasers resulted in coherent light sources with sufficient intensity. This made a positive contribution to nonlinear spectroscopy. In nonlinear spectroscopy, the interaction of high intensity electric fields induces a polarization response, which is not linear, but has contributions from higher order terms as described in the equation:

$$P = P^{(1)} + P^{(2)} + P^{(3)} + \dots$$
$$P = \epsilon_0 \chi^{(1)} E + \epsilon_0 \chi^{(2)} EE + \epsilon_0 \chi^{(3)} EEE + \dots \quad (2-3)$$

where $\chi^{(2)}$ and $\chi^{(3)}$ are the second and third order susceptibilities.²⁴

This dissertation particularly focuses on the second-order responses to the polarization. In such cases, the second-order term $\chi^{(2)}$ is crucial because it only results in nonzero values of the susceptibility in media where inversion symmetry is lacking.

When the electric field ($E = E_1 \cos \omega t$) is taken into account, the second-order polarization can be expressed as the equation:

$$\begin{aligned} P^{(2)} &= \epsilon_0 \chi^{(2)} (E_1 \cos \omega t)^2 \\ &= \frac{1}{2} \epsilon_0 \chi^{(2)} E_1^2 (1 + \cos 2\omega t) \end{aligned} \quad (2-4)$$

where ω is the angular frequency of the light. In a case wherein the dipole oscillates at twice the frequency of the incident light, 2ω , a phenomenon is known as second harmonic generation (SHG). For a particular experimental geometry, this approach also results in the idea of an effective SHG coefficient $d_{\text{eff}} = \frac{1}{2} \chi^{(2)}$.²⁴

The fundamental and second-harmonic waves will travel at different speeds attributed to the inverses of their respective refractive indices. To maximize SHG efficiency, geometries are required to match the wave-vectors and the phases of fundamental and harmonic beams. For collinear harmonic and fundamental waves, type I phase-matching can be obtained when an extraordinary (or ordinary) beam at the harmonic frequency is formed by adding two ordinary (or extraordinary) beams at the fundamental frequency. This can be described as the equation follows:

$$n_{2\omega} = n_{\omega} \quad (2-5)$$

where n is the refractive index and ω is the frequency

For type II phase-matching, it can be achieved when an extraordinary (or ordinary) beam at the harmonic frequency is formed by adding one ordinary (^o) and extraordinary (^e) beam at the fundamental frequency. The condition can be written as the equation:

$$2n_{2\omega} = n_{\omega}^o + n_{\omega}^e \quad (2-6)$$

SHG was first studied on single crystals.²⁵ A powder technique to evaluate the SHG behavior of materials was proposed by Kurtz and Perry in 1968.²⁶ Phase-matching occurs when the phase velocity of the fundamental radiation equals to the second harmonic. With the powder SHG technique, when phase-matching occurs the SHG efficiency increase with the particle size and reach to plateau. The non-phase-matching is observed when the SHG efficiency reaches a maximum and then decreases as particle size increases. The powder needs to be sieved into different sizes in the range of 20–150 μm for SHG measurements. The SHG efficiency of new NCS material may be compared with those of standard materials, i.e., $\alpha\text{-SiO}_2$, KH_2PO_4 (KDP), KTiOPO_4 (KTP), BaTiO_3 , LiNbO_3 (1064 nm output) and LiB_2O_5 (LBO), $\beta\text{-BaB}_2\text{O}_4$ ($\beta\text{-BBO}$) (532 nm output).

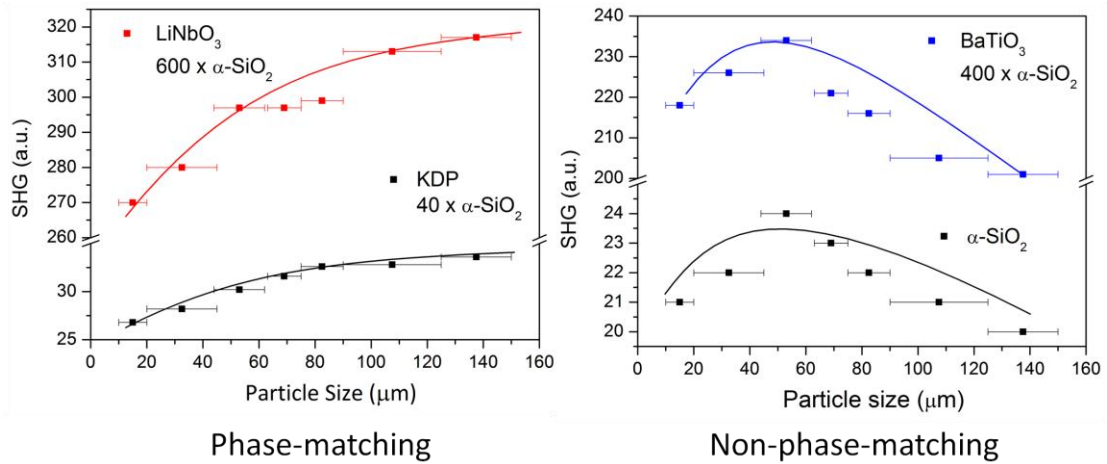


Figure 2.4 Examples of type I phase-matching (KDP and LiNbO_3) and non-phase-matching ($\alpha\text{-SiO}_2$ and BaTiO_3) materials²²

2.2.2 Piezoelectricity

The direct piezoelectric effect was first discovered in 1880 by J. Curie and P. Curie.²⁷ It was observed that some materials become electrically polarized when subjected to a mechanical force. The converse effect was discovered wherein the application of a voltage resulted in a macroscopic strain.²⁸ Thus with piezoelectricity, two effects are possible: direct and converse. For the direct effect, a change in polarization, P_i , can be expressed as $P_i = d_{ijk}\sigma_{jk}$, where d_{ijk} is the piezoelectric charge coefficient, whereas for the converse effect, a strain, ε_{jk} , can be expressed as $\varepsilon_{jk} = d_{ijk}E_i$, where d_{ijk} is the piezoelectric strain coefficient.

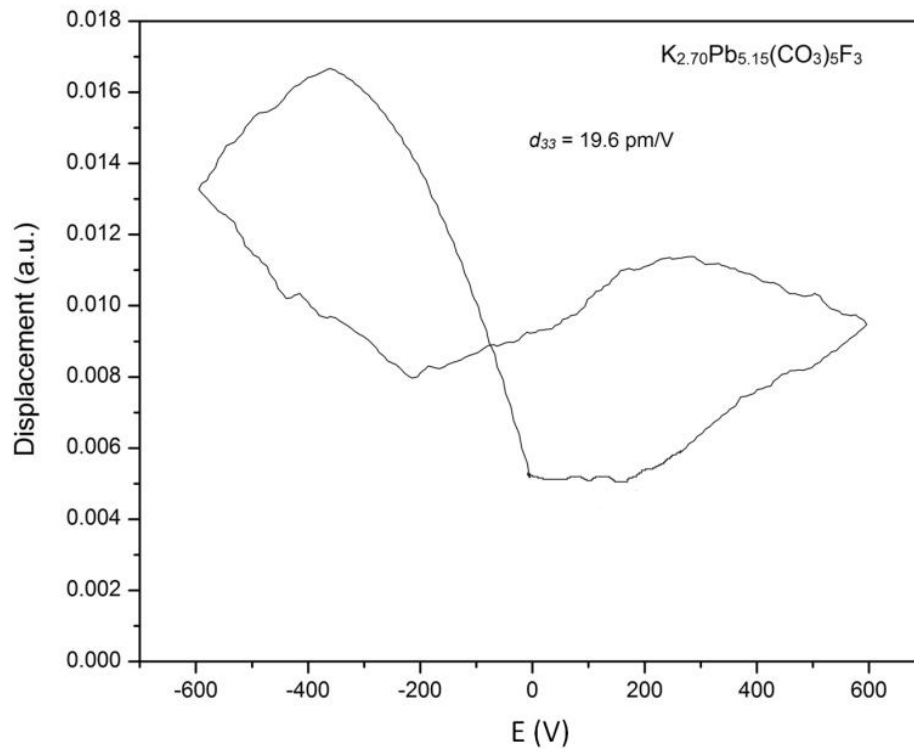


Figure 2.5 Displacement vs. applied voltage loop in $K_{2.70}Pb_{5.15}(CO_3)_5F_3$ ²⁹

2.2.3 Pyroelectricity

The pyroelectric effect may be defined as the change in spontaneous polarization, P_s , as a function of temperature.³⁰⁻³¹ The pyroelectric coefficient, p , a vector, in units of $\mu C m^{-2} K$, can be defined in the equation as follows:

$$p = \left(\frac{\partial P_s}{\partial T} \right)_{E,S} \quad (2-7)$$

where P_s is the spontaneous polarization in units of $\mu C m^{-2}$ and T is the temperature (K). The constraints are constant electric field (E) and constant elastic stress (S). Constant stress indicates that the material is free to thermally expand or contract. The primary pyroelectric coefficient is derived if the material is rigidly fixed as the measurements are being performed. The secondary pyroelectric coefficient is associated with the additional change in polarization attributable to the volume change as changing temperature. Practically, the unclamped measurements, however, result in the combination of the primary and secondary coefficients.

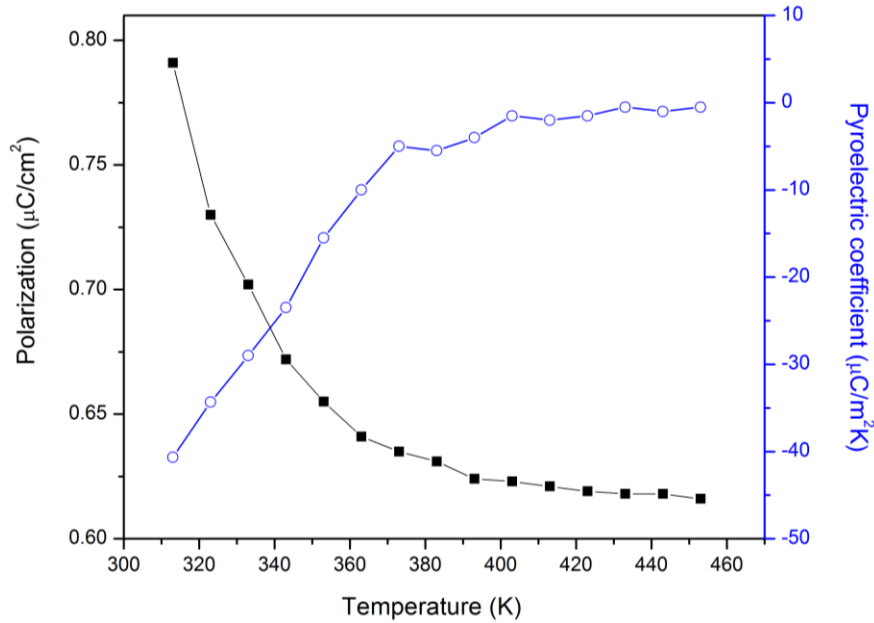


Figure 2.6 Polarization and pyroelectric coefficient of KH_2PO_4 ²²

2.2.4 Ferroelectricity

Ferroelectric materials can be defined as pyroelectric materials exhibiting a spontaneous electric polarization that can be reversed by an applied external electric field.^{21,32} Ferroelectricity is typically represented by a hysteresis loop showed in the Figure 2.7. The loop is characterized by the spontaneous polarization, P_s , the remnant polarization, P_r , and the coercive field, E_C . Each ferroelectric material possesses a Curie temperature, T_C , at which the phase transition occurs between centrosymmetric and noncentrosymmetric structures. Above T_C , the polarization of the material is a linear function of the applied electrical field. The dielectric susceptibility in the paraelectric state follows the equation:

$$\varepsilon = \varepsilon_0 + C_P(T - T_C) \quad (2-8)$$

where C_P is the paraelectric Curie constant, T_C is the Curie temperature and ε is the electrical polarizability.

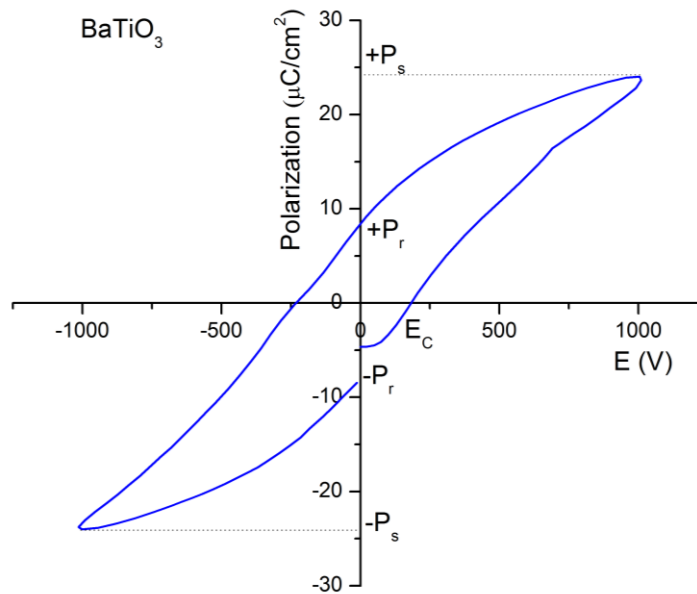


Figure 2.7 Ferroelectric hysteresis loop of BaTiO₃²²

Generally, ferroelectrics can be classified as ‘displacive’ and ‘order-disorder’. Displacive ferroelectrics exhibit a correlated shift of ions away from the centrosymmetric positions (i.e., BaTiO_3 and $\text{Ba}_2\text{KNb}_5\text{O}_{15}$). In ‘order-disorder’ material (i.e., KH_2PO_4 and $\text{K}_3\text{Fe}_5\text{F}_{15}$), randomly oriented dipoles become ordered. The phase transitions, however, often possess a combined character.³³

Ferroic materials are of technological importance and application as ‘smart materials’, for example as infrared detectors (pyroelectrics), actuators, positioners and micromotors (piezoelectrics), modulators (electro-optic), non-volatile direct random access memory and ferroelectric field-effect transistors (ferroelectrics).³²

2.3 Functional Properties of Strongly Correlated Electron Systems

2.3.1 Magnetism

Magnetic phenomena in solids are associated with the magnetic moments of its components. From classical electrodynamics, moving charged particles generate magnetic dipole moment. Magnetism is also a quantum mechanical phenomenon. Many elementary particles, such as electron, protons, neutrons and muons, have a characteristic magnetic moment, correlated to their intrinsic spin and orbital angular momentum S and L , through the gyromagnetic ratio (g - or Lande-factor).³⁴ For an electron in a certain orbit:

$$\mu_J = \frac{-g_J \mu_B J}{\hbar} \quad (2-9)$$

where J is the total angular momentum $J = S + L$, μ_B is the Bohr magneton $\mu_B = e\hbar/2m$, and g_J is the Lande g -factor given by:

$$g_J = \frac{3}{2} + \frac{S(S+1) - L(L+1)}{2J(J+1)} \approx 2 \quad (2-10)$$

The macroscopic magnetization observed for a material is the combination of the magnetic moments of all its components. However, the majority of the contributions cancel each other out (i.e., paired spins in closed shells), and magnetic ordering phenomena are mainly correlated to the collective interaction of unpaired d and f electrons of transition metals and lanthanides, respectively. Depending on the spin order, different types of magnetism can be classified: diamagnetic materials where all electrons are paired and aligned antiparallel; para-, ferro- and antiferromagnetism are referred to the random, parallel and antiparallel orientation of unpaired spins, respectively. Para- and

antiferromagnetic (PM, AFM) materials do not exhibit net magnetism, whereas ferromagnets (FM) possess a spontaneous magnetic moment. Also, the antiparallel order of moments of different magnitude (i.e. arising from different ionic species) gives rise to a net magnetization, and is known as ferrimagnetism.³⁵

Magnetic interactions can be probed from responses of a material with the presence of an external magnetic field.³⁴ The applied magnetic field H induces a magnetization M , which is a function of the magnetic susceptibility χ :

$$M = \chi H \quad (2-11)$$

Diamagnetic materials are repelled by a magnetic field resulting in small and negative χ . Superconducting materials are perfect diamagnets ($\chi = -1$) and expel magnetic flux from their interior (Meissner-Ochsenfeld effect). The unpaired spins of PM have a tendency to align with an external magnetic field, and thus PMs have small positive χ . However, thermal activation does not favor the spin-alignment, and gives rise to a temperature dependence of χ , expressed in the Curie law as follows:

$$\chi = C/T \quad (2-12)$$

with the Curie constant C , defined as:

$$C = \frac{N_A \mu_{eff}^2 \mu_B}{3k_B} \quad (2-13)$$

where N_A is Avogadro's number, k_B is Boltzmann constant and μ_{eff} is the effective magnetic moment:

$$\mu_{eff} = g_J \sqrt{J(J+1)} \approx g_J \sqrt{S(S+1)} \quad (2-14)$$

and can be approximated as the spin-only value in transition metals as the orbital moment is quenched by crystal field effects. Also AFM and FM materials have positive χ , where $\chi_{\text{AFM}} \lesssim \chi_{\text{PM}}$ and $\chi_{\text{FM}} \gg 1$. Ordering phenomena occur below a critical temperature, which can be determined from the temperature dependence of the magnetic susceptibility χ , i.e., for AFM, χ decreases below the Néel temperature T_N , while χ increases in a FM below the Curie temperature T_C . Above the ordering temperatures, AFM and FM follow the Curie-Weiss law:

$$\chi = C/(T - \theta) \quad (2-15)$$

where the Weiss constant θ is negative for AFM and positive for FM. Typical magnetic susceptibility curves as a function of temperature are shown in Figure 2.8.

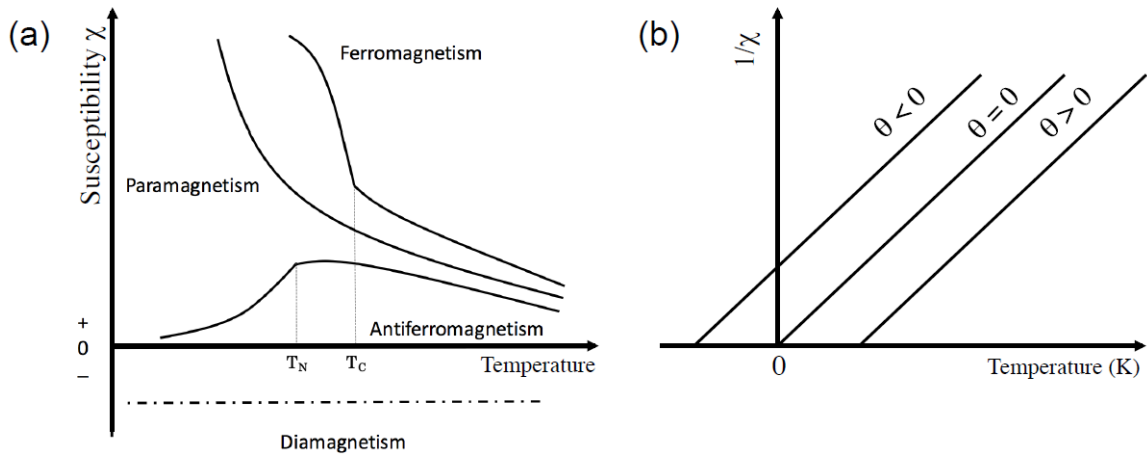


Figure 2.8 (a) Typical curves of the temperature dependence of magnetic susceptibility for paramagnetic (PM), ferromagnetic (FM), antiferromagnetic (AFM) and diamagnetic (DM) materials. (b) Illustration of the Curie-Weiss law; the inverse susceptibility is a linear function of temperature and the intercept with the x -axis gives the Weiss temperature θ .³⁴

2.3.2 Mott-Hubbard Physics

The strongly correlated systems were first investigated in the 1930s.^{36,37} The band theory of solids had successes in predicting properties of many materials, yet in some other cases, this was ineffective. Various transition metal oxides, which were half-filled and thus expected to be metallic, were found to be insulating instead.³⁸ It was suggested that the insulating state may be explained by taking into account Coulomb interactions between electrons. The classical example of a Mott insulator is nickel oxide, NiO. It was proposed that NiO should be insulating and the conduction occurs through hopping mechanism:



and the d -band splits owing to the Coulomb repulsion.

It was observed that the simplest band theories, based on the independent-electron approximation, are not sufficient for understanding and describing magnetic properties of transition metals and their compounds. The outer electronic shells, partially unfilled, fundamentally define the behavior of transition metals and their related compounds. They give rise to the strong electronic correlations which cannot be described by the Hartree-Fock approach. It was recognized that these systems should be investigated by more advanced theoretical tools. Mott and Hubbard were the main contributors to the development of the theoretical modeling in this scenario.³⁹⁻⁴⁰

The strong electronic correlations in the undoped cuprates (mother compounds of high T_c superconductors) cause the metallic phase vanished and give rise to an insulating antiferromagnetic ground state – a Mott insulator. The half-filled system, which can be

insulating, is implausible in Bloch theory of electron bands. The simplest model is given by the Hubbard Hamiltonian:⁴⁰

$$\mathcal{H} = -t \sum_{\langle ij \rangle} \sum_{\sigma} (c_{i\sigma}^{\dagger} c_{j\sigma} + c_{j\sigma}^{\dagger} c_{i\sigma}) + U \sum_i \hat{n}_{i\uparrow} \hat{n}_{i\downarrow} \quad (2-16)$$

In this equation, $c_{i\sigma}^{\dagger}$ creates an electron with spin σ on the lattice site i , and $\hat{n}_{i\sigma} = c_{i\sigma}^{\dagger} c_{i\sigma}$ is the corresponding number operator. Parameter t is the transfer integral, and obtained from the overlap of two atomic orbitals. Hubbard U is the Coulomb repulsion of two electrons on the same site.

Hubbard Hamiltonian is the minimal many-body Hamiltonian, that concerns the fundamental nature of the competition between two mutually antagonistic phenomena. If the electrons are delocalized, the kinetic energy is gained and the metallic state is present. If the electron-electron repulsion becomes significant, the electrons localize onto atomic sites and the system becomes a Mott insulator.⁴¹

Metallic state can become unstable in other ways as well. As the temperature is decreased, electron charge and spin may order owing to correlations. In some other cases, several different interactions compete. In the following sections, a briefly review of the most relevant types of instabilities is presented.

2.3.3 Charge Order

Wigner was the first to introduce the concept of charge ordering.³⁶ It was reported that if the density of the electronic gas is sufficiently low, the Coulomb repulsion will dominate over the electron delocalization. At low temperatures, Coulomb interaction produces a long range ordered charge pattern of localized electrons arranged into a hexagonal lattice, as depicted in Figure 2.9.

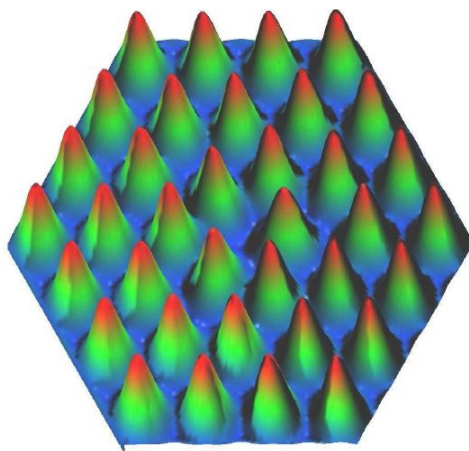


Figure 2.9 Charge order on a two dimensional Wigner crystal³⁶

Charge ordering is a common occurrence in transition metal compounds with a discrete underlying atomic lattice. The presence of reasonably localized d orbitals, with small interatomic overlap, enhances the effect of the short-range Coulomb repulsion between electrons on different lattice sites. As a result, charge order occurs at much higher electron densities, and it must be commensurate with the atomic lattice.³⁷

The elementary Hamiltonian, which describes charge ordering, needs to take into account Coulomb interaction not only within the same site (U), but also between neighboring sites (V_{ij}). A Hamiltonian represents what is known as the extended Hubbard

model where the Coulombic V_{ij} term is crucial for understanding the charge ordered states: ⁴²

$$\mathcal{H} = -t \sum_{\langle ij \rangle} \sum_{\sigma} (c_{i\sigma}^{\dagger} c_{j\sigma} + c_{j\sigma}^{\dagger} c_{i\sigma}) + U \sum_i \hat{n}_{i\uparrow} \hat{n}_{i\downarrow} + \sum_{\langle ij \rangle \sigma \sigma'} V_{ij} \hat{n}_{i\sigma} \hat{n}_{j\sigma'} \quad (2-17)$$

When a complete charge order occurs, the system becomes insulating. The nature of the instability is electronically driven, however, a slight deformation of the underlying lattice is also observed. Yet, it is not completely understood how the structural changes are strongly correlated to other physical phenomena. In many cases, the dramatic changes are observed in the conductivity and other physical properties of the charge-ordering system only below the temperature where a symmetry break occurs in the lattice. ⁴³

2.3.4 Peierls-Instability and Density Waves

Charge order is a phenomenon occurring in a real-space. A similar effect of long range charge modulation in a metal can be observed through an entirely distinct mechanism, which occurs in the reciprocal space (Figure 2.10). In this case, the geometry of the Fermi surface produces the charge modulation and correlations are not required.

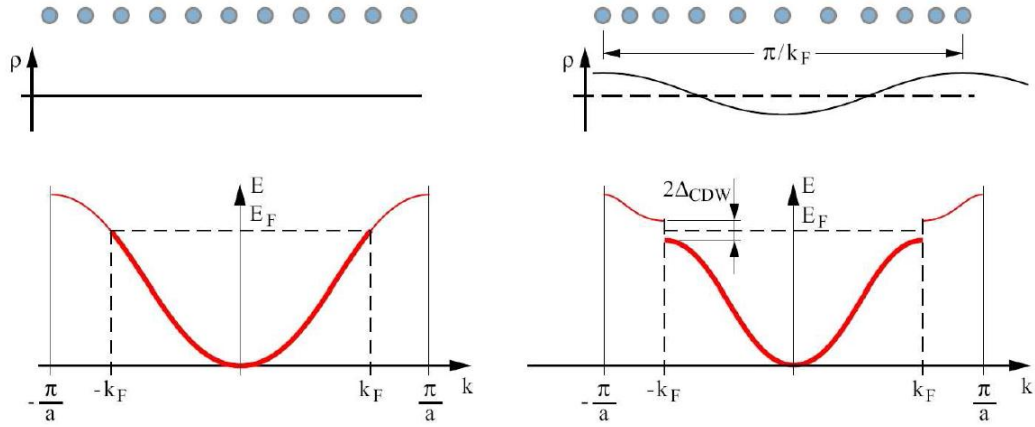


Figure 2.10 Left: a metal with a homogeneous charge distribution, $\rho = \text{const}$ and a conduction band filled up to the Fermi energy. Right: The charge modulation with a wavelength π/k_F changes periodicity and thus reduces the Brillouin zone, producing a gap at $\pm k_F$. The energy of the filled portion of the band is lowered and the system becomes insulating.⁴⁴

The charge instability, a charge density wave (CDW), is driven by the minimization of the kinetic energy of the conduction electrons, that gives rise to a reconstruction of the Fermi surface and results in the Peierls transition. This is observed in many materials with a highly anisotropic band structure, such as blue bronze $\text{K}_{0.3}\text{MoO}_3$, NbSe_3 or $(\text{TaSe}_4)_2\text{I}$.

If an electron-phonon interaction is present, it may be energetically favorable that a periodic lattice distortion occurs.⁴⁵ The wavelength is related to the Fermi wave vector, as depicted in Figure 2.10, and does not necessarily have to be commensurate to the lattice. The important condition is that the original Fermi surface has to be nesting. The nesting parts are connected by a vector Q which determines the wavelength and the direction of the charge density modulation.³⁷ Finally, the gain in electronic energy has to compensate for the energy of the lattice modulation.

A Hamiltonian, which describes the main features of the Peierls transition and the collective mode, is concerned with the electron-phonon interaction:⁴⁵

$$\mathcal{H} = \sum_{\langle k, \sigma \rangle} \epsilon_k c_{k\sigma}^\dagger c_{k\sigma} + \sum_{\langle q, \sigma \rangle} \hbar \omega_q^0 b_q^\dagger b_q + \sum_{\langle k, q, \sigma \rangle} g(k) c_{k+q, \sigma}^\dagger c_{k, \sigma} (b_q + b_{-q}^\dagger) \quad (2-18)$$

In this equation, c_k^\dagger and b_q^\dagger create an electron and phonon with moment k and q ; ϵ_k and ω_q^0 are electron and phonon dispersions; $g(k)$ is the electron-phonon coupling constant. The system is a metal above the temperature at which the transition occurs. Below that temperature, the system becomes semiconducting with a band gap which increases as decreasing temperature.

An analogous modulation of density in the spin can also take place without changing the charge distribution.⁴⁴ This gives rise to an antiferromagnetic ground state described in a spin density wave (SDW). The distributions of charge and spin density in the metallic (M) state, SDW, CDW and bond density wave (BDW) states are depicted in Figure 2.11.⁴⁶ The magnitude of the up-spin and down-spin electron density on a lattice site is described by the length of the upward and downward arrow, respectively. The bond order magnitude between neighboring sites is represented by the height of the dashed line. As

presented in Figure 2.11, the SDW and CDW possess spin density and charge density alternation, respectively. The bond orders of the BDW exhibit magnitude alternation, whereas those of SDW and CDW states remain identical. The CDW can be differentiated from the BDW by the location of the density alternation, i.e., the density alternation occurs at on-site and inter-site electron density for CDW and BDW, respectively.

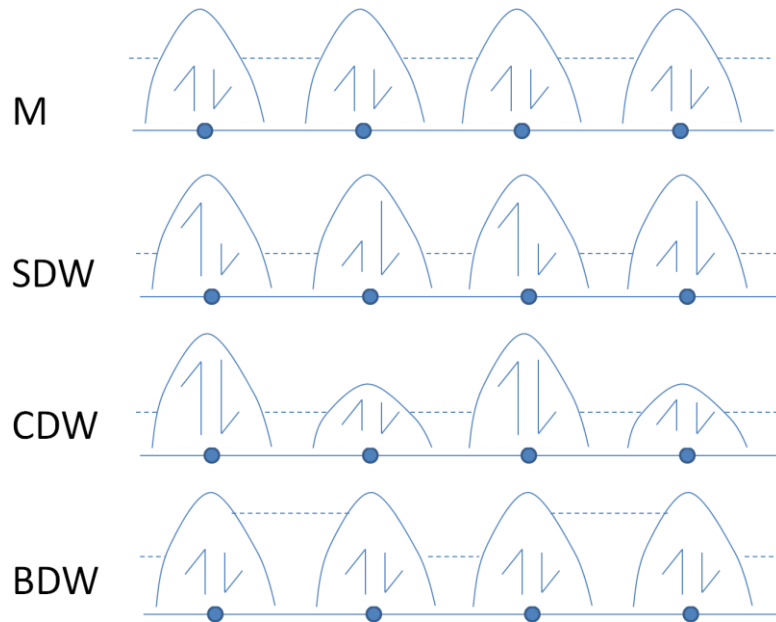


Figure 2.11 The charge and spin density distributions in the metallic (M), spin density wave (SDW), charge density wave (CDW) and bond density wave (BDW) states ⁴⁶

2.3.5 Electrical Conductivity

The electrical transport properties of a solid can be understood from the electronic band structure. The energy bands of a condensed material consist of an infinite number of overlapping atomic orbitals, wherein the filled orbitals form the valence band and the empty orbitals form the conduction band separated by a band gap. The different types of electrical behavior, depicted in Figure 2.12, can be classified attributable to the separation of the band gap ΔE : materials with $\Delta E > 2.5$ eV are insulators, $0 < \Delta E < 2.5$ eV are semiconductors and $\Delta E = 0$ eV are metals.⁴⁷

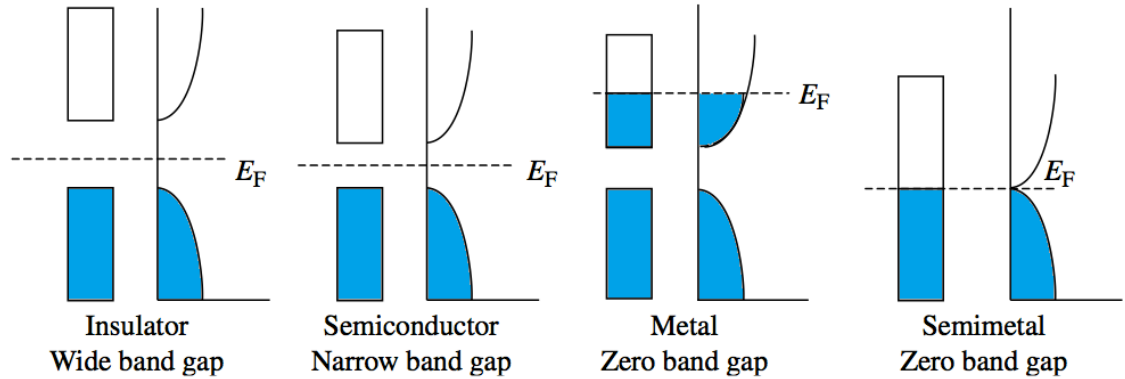


Figure 2.12 Schematic illustrations of the band structure in different types of materials. The classification is based on the band gap between valence band (blue) and conduction band (white).

Semiconductors and insulators are distinguished by the width of the band gap. In narrow-gap semiconducting materials, electrons can be thermally excited into the conduction band, and charge carriers in both bands (i.e., holes in the valence and electrons in the conduction band) give electrical conduction.³⁴

The temperature dependence of the conductivity in semiconductors arises primarily from the changes in the number of charge carriers as a function of temperature. This is observed owing to a finite energy gap. Carriers are much more dilute than in metals, approximately 10^{19} cm^{-3} electrons or holes. The mobilities of carriers, nonetheless, are typically greater than those in a metal, approximately two or three orders of magnitude. The conduction occurs when carriers (electrons and holes) are thermally activated out of filled bands.⁴⁸ The conductivity can be described as the equation:

$$\sigma = \sigma_0 \exp \frac{-1/2\epsilon_g}{k_B T} \quad (2-19)$$

where ϵ_g is the energy gap between the highest occupied valence bands and the lowest empty conduction bands, $\epsilon_g = \epsilon_C - \epsilon_V$

Compared with metals, an additional feature in semiconductors is the occurrence of a mechanism alternative to transport property. The presence of localized charge carriers, owing to impurities, gives rise to hopping. Also, the exponential temperature dependence is observed to be more dominated at low temperatures.

2.4 References

- (1) Wu, H.; Yu, H.; Yang, Z.; Hou, X.; Su, X.; Pan, S.; Poeppelmeier, K. R.; Rondinelli, J. M. *J. Am. Chem. Soc.* **2013**, *135*, 4215.
- (2) Zhang, G.; Li, Y.; Jiang, K.; Zeng, H.; Liu, T.; Chen, X.; Qin, J.; Lin, Z.; Fu, P.; Wu, Y.; Chen, C. *J. Am. Chem. Soc.* **2012**, *134*, 14818.
- (3) Gautier, R.; Norquist, A. J.; Poeppelmeier, K. R. *Cryst. Growth Des.* **2012**, *12*, 6267.
- (4) Lu, H.; Gautier, R.; Donakowski, M. D.; Tran, T. T.; Edwards, B. W.; Nino, J. C.; Halasyamani, P. S.; Liu, Z.; Poeppelmeier, K. R. *J. Am. Chem. Soc.* **2013**, *135*, 11942.
- (5) Yeon, J.; Kim, S.-H.; Hayward, M. A.; Halasyamani, P. S. *Inorg. Chem.* **2011**, *50*, 8663.
- (6) Nguyen, S. D.; Yeon, J.; Kim, S.-H.; Halasyamani, P. S. *J. Am. Chem. Soc.* **2011**, *133*, 12422.
- (7) Kim, S.-H.; Yeon, J.; Halasyamani, P. S. *Chem. Mater.* **2009**, *21*, 5335.
- (8) Opik, U.; Pryce, M. H. L. *Proc. R. Soc. London, Ser. A* **1957**, *238*, 425.
- (9) Jahn, H. A.; Teller, E. *Proc. R. Soc. London, Ser. A* **1937**, *161*, 220.
- (10) Pearson, R. G. *J. Amer. Chem. Soc.* **1969**, *91*, 4947.
- (11) Pearson, R. G. *J. Mol. Struct.: THEOCHEM* **1983**, *12*, 25.
- (12) Wheeler, R. A.; Whangbo, M. H.; Hughbanks, T.; Hoffmann, R.; Burdett, J. K.; Albright, T. A. *J. Am. Chem. Soc.* **1986**, *108*, 2222.
- (13) Goodenough, J. B. *Annu. Rev. Mater. Sci.* **1998**, *28*, 1.
- (14) Reinen, D.; Atanasov, M. *NATO Sci. Ser., II* **2001**, *39*, 83.

- (15) Atanasov, M.; Reinen, D. *J. Phys. Chem. A* **2001**, *105*, 5450.
- (16) Atanasov, M.; Reinen, D. *Inorg. Chem.* **2004**, *43*, 1998.
- (17) Albright, T. A.; Burdett, J. K.; Whangbo, M.-H. *Orbital Interactions in Chemistry*; Second ed.; Hoboken, pp 185-186, New Jersey : Wiley, 2013.
- (18) Nalwa, H. S. *Handbook of Advanced Electronic and Photonic Materials and Device*; Academic Press: San Diego, 2001.
- (19) Jona, F.; Shirane, G. *Ferroelectric Crystals*; Pergamon Press: Oxford, 1962.
- (20) Auciello, O.; Scott, J. F.; Ramesh, R. *Phys. Today* **1998**, *51*, 22.
- (21) Haertling, G. H. *J. Am. Ceram. Soc.* **1999**, *82*, 797.
- (22) Ok, K. M.; Chi, E. O.; Halasyamani, P. S. *Chem. Soc. Rev.* **2006**, *35*, 710.
- (23) Halasyamani, P. S. *Chem. Mater.* **2004**, *16*, 3586.
- (24) Munn, R. W. I., C. N. *Principles and Applications of Nonlinear Optical Materials*; CRC Press Inc.: Florida, 1993.
- (25) Franken, P. A.; Hill, A. E.; Peters, C. W.; Weinreich, G. *Phys. Rev. Lett.* **1961**, *7*, 118.
- (26) Kurtz, S. K.; Perry, T. T. *J. Appl. Phys.* **1968**, *39*, 3798.
- (27) Curie, J.; Curie, P. *Bull. Soc. Min de France* **1880**, *3*, 90.
- (28) Cady, W. G. *Piezoelectricity; an Introduction to the Theory and Applications of Electromechanical Phenomena in Crystals*; Dover: New York, 1964.
- (29) Tran, T. T.; Halasyamani, P. S. *Inorg. Chem.* **2013**, *52*, 2466.
- (30) Lang, S. B. *Sourcebook of Pyroelectricity*; Gordon and Breach, 1974.
- (31) Lang, S. B. *Phys. Today* **2005**, *58*, 31.

- (32) Ravez, J. *Comptes Rendus de l'Académie des Sciences - Series IIC - Chemistry* **2000**, *3*, 267.
- (33) Blinc, R. *Ferroelectrics* **2004**, *301*, 3.
- (34) Kittel, C. *Introduction to Solid State Physics*; Hoboken, NJ : Wiley, 2005.
- (35) Goodenough, J. B. *Magnetism and the Chemical Bond*; New York: Interscience Publishers, 1963.
- (36) Wigner, E. *Phys. Rev.* **1934**, *46*, 1002.
- (37) Fulde, P.; Thalmeier, P.; Zwicknagl, G. *Solid State Phys.* **2006**, *60*, 1.
- (38) deBoer, J. H.; Verwey, E. J. W. *Proc. Phys. Soc., London* **1937**, *49*, 59.
- (39) Mott, N. F. *Metal-insulator Transitions*; London, New York : Taylor & Francis, 1990.
- (40) Hubbard, J. *Proc. R. Soc. London, Ser. A* **1963**, *276*, 238.
- (41) Fazekas, P. *Lecture Notes on Electron Correlation and Magnetism*; World Scientific, 1999.
- (42) Seo, H.; Hotta, C.; Fukuyama, H. *Chem. Rev.* **2004**, *104*, 5005.
- (43) Dressel, M.; Drichko, N. *Chem. Rev.* **2004**, *104*, 5689.
- (44) Dressel, M. *Naturwissenschaften* **2007**, *94*, 527.
- (45) Grüner, G. *Rev. Mod. Phys.* **1988**, *60*, 1129.
- (46) Whangbo, M. H. *Acc. Chem. Res.* **1983**, *16*, 95.
- (47) Lalena, J. N.; Cleary, D. A. *Principles of Inorganic Materials Design*; Hoboken, N.J. : John Wiley, 2010.
- (48) Chambers, R. *Electrons in Metals and Semiconductors*; Chapman and Hall, 1990.

Chapter 3 Experiments

3.1 Synthesis

Conventional solid-state reactions, hydrothermal techniques and flux methods were used to synthesize polycrystalline samples and grow crystals of the materials discussed in this dissertation.

3.1.1 Solid-State Reactions

The polycrystalline materials discussed in this dissertation have been synthesized through solid-state routes. Solid-state reactions are governed by mobility and diffusion, thus the experiments were performed at appropriately high temperatures. Nevertheless, reactions are relatively slow and often require long annealing times to obtain pure products. The starting materials were thoroughly ground to maximize the surface available for reaction and the mixing between different grains. The contact between grains was improved by pressing the powder into pellets. The pellets were placed in alumina boats that were heated to reaction temperature in flowing CO₂ gas, held for several days and then cooled to room temperature at a programmed rate of 180°C h⁻¹. Details of experiments of solid-state reactions for synthesizing the materials discussed in this dissertation are summarized in Table 3.1. The separation of product and by-products is often not feasible and thus the synthetic conditions have to be adjusted to obtain the desired materials in pure phases. The progress and success of reactions were monitored by powder X-ray diffraction.

Table 3.1 Solid-state reactions for synthesizing $\text{KPb}_2(\text{CO}_3)_2\text{F}$, $\text{K}_{2.70}\text{Pb}_{5.15}(\text{CO}_3)_5\text{F}_3$, RbPbCO_3F , CsPbCO_3F , KMgCO_3F and RbMgCO_3F

Compound	Starting materials	Temperature, °C	Time, days
$\text{KPb}_2(\text{CO}_3)_2\text{F}$	KF 0.116g (2.00×10^{-3} mol) PbCO ₃ 1.07g (4.00×10^{-3} mol)	250	2
$\text{K}_{2.70}\text{Pb}_{5.15}(\text{CO}_3)_5\text{F}_3$	KF 0.126g (2.16×10^{-3} mol) PbCO ₃ 1.07g (4.00×10^{-3} mol) PbF ₂ 0.029g (0.12×10^{-3} mol)	270	3
RbPbCO_3F	RbF 0.418g (4.00×10^{-3} mol) PbCO ₃ 1.07g (4.00×10^{-3} mol)	280	3
CsPbCO_3F	CsF 0.608g (4.00×10^{-3} mol) PbCO ₃ 1.07g (4.00×10^{-3} mol)	270	3
KMgCO_3F	KF 0.232g (4.00×10^{-3} mol) MgCO ₃ 0.337g (4.00×10^{-3} mol)	330	7
RbMgCO_3F	RbF 0.418g (4.00×10^{-3} mol) MgCO ₃ 0.337g (4.00×10^{-3} mol)	330	5

3.1.2 Hydrothermal Techniques

Hydrothermal techniques provide a synthetic manner wherein crystals of new systems can be grown. For hydrothermal methods, the appropriate reagents and solvents are combined in 23-ml Teflon-lined autoclaves. The autoclaves were subsequently closed, gradually heated to reaction temperatures, held for several days, and cooled slowly to room temperature at a rate of 6°C h^{-1} . The mother liquor was decanted, and the products were recovered by vacuum filtration and then washed with ethanol. Details of

hydrothermal reactions for growing crystals of the materials discussed in this dissertation are summarized in Table 3.2.

Table 3.2 Hydrothermal reactions for growing crystals of $\text{KPb}_2(\text{CO}_3)_2\text{F}$, $\text{K}_{2.70}\text{Pb}_{5.15}(\text{CO}_3)_5\text{F}_3$, RbPbCO_3F , CsPbCO_3F , KMgCO_3F and RbMgCO_3F

Compound	Starting materials and solvents	T (°C)	Time, day(s)
$\text{KPb}_2(\text{CO}_3)_2\text{F}$ $\text{K}_{2.70}\text{Pb}_{5.15}(\text{CO}_3)_5\text{F}_3$ (co-crystallizing)	$\text{Pb}(\text{OAc})_2 \cdot 3\text{H}_2\text{O}$ 0.379 g (1.00×10^{-3} mol) KF 0.232g (4.00×10^{-3} mol) CH_3OH 1.50 mL (3.71×10^{-2} mol) CF_3COOH 1.50 mL (1.94×10^{-2} mol)	180	1
RbPbCO_3F	$\text{Pb}(\text{OAc})_2 \cdot 3\text{H}_2\text{O}$ 0.379 g (1.00×10^{-3} mol) RbF 0.627g (6.00×10^{-3} mol) CH_3OH 1.00 mL (2.47×10^{-2} mol) CF_3COOH 1.00 mL (1.29×10^{-2} mol)	180	1
CsPbCO_3F	$\text{Pb}(\text{OAc})_2 \cdot 3\text{H}_2\text{O}$ 0.379 g (1.00×10^{-3} mol) CsF 0.608g (4.00×10^{-3} mol) CH_3OH 1.25 mL (3.09×10^{-2} mol) CF_3COOH 1.25 mL (1.61×10^{-2} mol)	180	1
KMgCO_3F	KF 0.017g (0.30×10^{-3} mol) KMgCO_3F 0.426g (3.00×10^{-3} mol) H_2O 2 mL (0.11×10^{-3} mol)	230	9
RbMgCO_3F	RbF 0.031g (0.30×10^{-3} mol) RbMgCO_3F 0.566g (3.00×10^{-3} mol) H_2O 2 mL (0.11×10^{-3} mol)	200	7

3.1.3 Flux Method

The synthesis of materials containing low-valent transition metal is known to be challenging and flux method under inert atmosphere is essential for discovering new synthetic routes. A reduced niobium (III/IV) oxyfluoride, $\text{Nb}_2\text{O}_2\text{F}_3$, was synthesized through the reaction of Nb, SnF_2 and SnO in Sn flux (4:4:3:8 molar ratio) in welded Nb containers within evacuated quartz jacket. The reaction was performed at 600 °C for 7 days, followed by slowly cooling (3 °C/hour) to 400 °C. The reaction charge was then centrifuged while at 400 °C to separate the crystals from the Sn flux, and then air-quenched to room temperature. Black and shiny crystals, subsequently determined to be $\text{Nb}_2\text{O}_2\text{F}_3$, were obtained. The compound is relatively stable to air and moisture. No traces or any changes in chemical and physical properties were observed if the $\text{Nb}_2\text{O}_2\text{F}_3$ crystals were exposed to the air for a few days. All experimental manipulations and handling were performed under inert conditions: within a purified Ar-atmosphere glovebox with total H_2O and O_2 levels of < 0.1 ppm. The products were stored in a glovebox, leaving the fresh and pure sample for further characterization. All polycrystalline samples (ground crystals) used in physical and chemical property measurements were determined to be phase pure by X-ray powder diffraction.

3.2 Characterizations

3.2.1 Single-Crystal X-Ray Diffraction

Crystals with appropriate sizes and decent quality were selected for single-crystal diffraction analysis. Data were collected on a Bruker platform diffractometer equipped with a 4K CCD APEX II detector using graphite-monochromated Mo-K α radiation at room temperature or low temperature utilizing liquid nitrogen (for air/moisture-sensitive samples and structural phase transition studies). A hemisphere of data (at 6 cm detector distance) was collected using a narrow-frame algorithm with scan widths of 0.30° in omega and an exposure time of 20 – 90 seconds per frame. The data were integrated using the SAINT-V7.23A program,¹ with the intensities corrected for Lorentz factor, polarization, air absorption, and absorption attributable to the variation in the path length through the detector faceplate. TWINABS or SADABS absorption corrections were applied based on the entire data sets collected.¹ Redundant reflections were averaged. Final cell constants were refined using orientation reflections having $I > 10\sigma(I)$. Details of experiments of single-crystal X-ray diffraction for elucidating the crystal structures of the materials discussed in this dissertation are summarized in Table 3.3.

The positions of the heavy atoms were determined by Direct methods using SHELXS-97,² and the remaining atoms were located by difference Fourier maps and least-squares cycles utilizing SHELXL-97.³ All calculations were performed using SHELXL-97 crystallographic software package.^{3,4} For all of the structural figures, the program VESTA was used.⁵

Table 3.3 Details of single-crystal X-ray diffraction experiments for $\text{K}\text{Pb}_2(\text{CO}_3)_2\text{F}$, $\text{K}_{2.70}\text{Pb}_{5.15}(\text{CO}_3)_5\text{F}_3$, RbPbCO_3F , CsPbCO_3F , KMgCO_3F , RbMgCO_3F and $\text{Nb}_2\text{O}_2\text{F}_3$

Compound	Selected crystal	Exposure time, s/frame	T (K)
$\text{K}\text{Pb}_2(\text{CO}_3)_2\text{F}$	A colorless hexagonal plate crystal $0.10 \times 0.10 \times 0.03 \text{ mm}^3$	90	293(2)
$\text{K}_{2.70}\text{Pb}_{5.15}(\text{CO}_3)_5\text{F}_3$	A colorless block crystal $0.10 \times 0.10 \times 0.05 \text{ mm}^3$	50	293(2)
RbPbCO_3F	A colorless trigonal prism crystal $0.20 \times 0.12 \times 0.12 \text{ mm}^3$	35	213(2)
CsPbCO_3F	A colorless plate crystal $0.20 \times 0.12 \times 0.08 \text{ mm}^3$	35	213(2)
KMgCO_3F	A colorless block crystal $0.09 \times 0.08 \times 0.07 \text{ mm}^3$	60	293(2)
RbMgCO_3F	A colorless block crystal $0.10 \times 0.08 \times 0.07 \text{ mm}^3$	60	293(2)
$\text{Nb}_2\text{O}_2\text{F}_3$	A black plate crystal $0.20 \times 0.20 \times 0.08 \text{ mm}^3$	20	293(2) 83(2)

3.2.2 Powder X-Ray Diffraction

Powder X-ray diffraction (PXRD) experiments for all of the materials in this thesis were performed using a PANalytical X'Pert PRO diffractometer equipped with Cu $\text{K}\alpha$ radiation. The data were collected in the 2θ range of 5° - 90° with a step size of 0.008° and a scan time of 0.3s. No impurities were observed and the experimental and calculated PXRD are in excellent agreement.

3.2.3 Energy-Dispersive X-Ray Spectroscopy (EDS) Analysis

A JEOL JSM 6330F field emission scanning electron microscope equipped with an electron dispersive spectrometer was used to determine the metal ratios in $\text{K}_{2.70}\text{Pb}_{5.15}(\text{CO}_3)_5\text{F}_3$, RbPbCO_3F , CsPbCO_3F , KMgCO_3F , RbMgCO_3F and the presence of Nb, O and F and confirm the absence of Sn above ≈ 0.03 wt.% level in $\text{Nb}_2\text{O}_2\text{F}_3$. The data crystals of $\text{K}_{2.70}\text{Pb}_{5.15}(\text{CO}_3)_5\text{F}_3$, RbPbCO_3F , CsPbCO_3F , KMgCO_3F and RbMgCO_3F were mounted separately on one flat face and coated with 25 nm carbon. Intensity data were processed by EDAX TEAM software. Analyses on these samples were obtained with a focused beam of 15 keV accelerating voltage and 12 μA emission current.

3.2.4 Thermal Analysis

Thermogravimetric analysis was performed on an EXSTAR TG/DTA 6300 instrument. Approximately 20 mg of each compound, namely, $\text{KPb}_2(\text{CO}_3)_2\text{F}$, $\text{K}_{2.70}\text{Pb}_{5.15}(\text{CO}_3)_5\text{F}_3$, RbPbCO_3F , CsPbCO_3F , KMgCO_3F , RbMgCO_3F were placed in a platinum pan and heated at a rate of $10^\circ\text{C min}^{-1}$ from room temperature to 900°C under flowing N_2 .

3.2.5 Ultraviolet-Visible (UV-Vis) Spectroscopy

UV-Vis reflectance data of $\text{KPb}_2(\text{CO}_3)_2\text{F}$, $\text{K}_{2.70}\text{Pb}_{5.15}(\text{CO}_3)_5\text{F}_3$, RbPbCO_3F , CsPbCO_3F were collected by Dr. Martin Donakowski in the Kenneth R. Peoppelmeier group (Northwestern University) on a Varian Cary 500 Scan UV-vis-NIR spectrophotometer over the 200–2000 nm spectral range at room temperature. Poly(tetrafluoroethylene) was used as a diffuse reflectance standard.

UV-Vis transmission data of KMgCO_3F and RbMgCO_3F were collected on a Cary 5000 UV-vis-NIR spectrophotometer over the 175–2000 nm range at room temperature.

3.2.6 Infrared (IR) Spectroscopy

The Fourier transform infrared spectroscopy (FTIR) spectra of $\text{KPb}_2(\text{CO}_3)_2\text{F}$, $\text{K}_{2.70}\text{Pb}_{5.15}(\text{CO}_3)_5\text{F}_3$, RbPbCO_3F , CsPbCO_3F , KMgCO_3F and RbMgCO_3F were collected by Dr. Martin Donakowski and Dr. Shichao Wang in the Kenneth R. Peoppelmeier group (Northwestern University) on a Bruker Tensor 37 FTIR with the use of a KBr pellet pressed at 15000 PSI. A total of 64 scans were recorded and a background spectrum was subtracted.

3.2.7 Raman Scattering

Raman scattering spectra of $\text{Nb}_2\text{O}_2\text{F}_3$ were measured by Dr. Alexander P. Litvinchuk using the triple spectrometer Jobin-Yvon T64000, equipped with an optical microscope and charge-coupled-device detector. A 100 \times objective was used to both focus the incident laser beam into a spot of about 2 micrometer in diameter and collect the scattered light in the backward scattering geometry. The 514.5 nm Ar^+ laser line was used for the excitation. Laser power did not exceed 0.5 mW in order to avoid heating of the sample. The spectral resolution did not exceed 1.5 cm^{-1} . Sample was mounted on a cold finger of a helium flow cryostat (Microstat, Oxford) and temperature was control to within 0.1K.

3.3 Physical Property Measurements

3.3.1 Second-Harmonic Generation (SHG)

Powder SHG measurements were performed on a modified Kurtz-nonlinear optical (NLO) system using a pulsed Nd:YAG laser with a wavelength of 1064 nm and 532 nm. A detailed description of the equipment and methodology has been published.⁶ As the powder SHG efficiency has been shown to strongly depend on particle size,⁷ $\text{K}_{2.70}\text{Pb}_{5.15}(\text{CO}_3)_5\text{F}_3$, RbPbCO_3F , CsPbCO_3F , KMgCO_3F and RbMgCO_3F were ground and sieved into distinct particle size ranges (<20, 20–45, 45–63, 63–75, 75–90, >90 μm). Relevant comparisons with known SHG materials were made by grinding and sieving crystalline $\alpha\text{-SiO}_2$, LiNbO_3 and $\beta\text{-BaB}_2\text{O}_4$ into the same particle size ranges. No index matching fluid was used in any of the experiments.

3.3.2 Piezoelectric Measurements

Converse piezoelectric measurements were performed using a Radiant Technologies RT66A piezoelectric test system with a TREK (model 609E-6) high voltage amplifier, Precision Materials Analyzer, Precision High Voltage Interface and MTI 2000 Fotonic Sensor. $\text{K}_{2.70}\text{Pb}_{5.15}(\text{CO}_3)_5\text{F}_3$, RbPbCO_3F , CsPbCO_3F , KMgCO_3F and RbMgCO_3F were pressed separately into pellets (~1.2 cm diameter, ~ 0.7 mm thickness) and sintered at 260–330°C for 3 days. Silver paste was applied to both sides of the pellets, and the pellets were cured at 250°C for 12 hours.

3.3.3 Magnetic and Transport Measurements

The magnetic and transport measurements were performed by Dr. Bernd Lorenz and Dr. Melissa Gooch. The magnetic properties of $\text{Nb}_2\text{O}_2\text{F}_3$ were studied in a Magnetic Property Measurement System (MPMS, Quantum Design) in magnetic fields up to 5 Tesla and temperatures between 2 K and room temperature (~ 300 K). Several single crystals with random orientations were used for magnetization measurements. The resistivity (transport) measurements for $\text{Nb}_2\text{O}_2\text{F}_3$ were performed on a compressed polycrystalline pellet using the standard four-probe method, employing a Keithley 220 dc current source and a Keithley 182 nano voltmeter. Thin platinum wires were attached to the sample using silver paint.

3.3.4 Heat Capacity Measurements

The heat capacity measurements were performed by Dr. Bernd Lorenz and Dr. Melissa Gooch. The heat capacity was measured using a relaxation method implemented as an option into the Physical Property Measurement System (PPMS, Quantum Design). Several crystals of $\text{Nb}_2\text{O}_2\text{F}_3$ with a total mass of a few milligrams were mounted on the sample platform for measurement.

3.4 Electronic Structure Calculations

First-principles density functional theory (DFT) calculations for $\text{KPb}_2(\text{CO}_3)_2\text{F}$, $\text{K}_{2.70}\text{Pb}_{5.15}(\text{CO}_3)_5\text{F}_3$ (Chapter 4), RbPbCO_3F , CsPbCO_3F (Chapter 5), RbMgCO_3F (Chapter 6) and $\text{Nb}_2\text{O}_2\text{F}_3$ (Chapter 7) were carried out using the Vienna ab initio Simulation Package (VASP).^{8,9}

For $\text{KPb}_2(\text{CO}_3)_2\text{F}$, $\text{K}_{2.70}\text{Pb}_{5.15}(\text{CO}_3)_5\text{F}_3$, RbPbCO_3F , CsPbCO_3F and RbMgCO_3F , the calculations were performed by Dr. Jiangang He and Dr. James M. Rondinelli (Northwestern University) using the PBEsol¹⁰ generalized-gradient approximation for the exchange-correlation potential with a planewave cutoff of 540 eV. The electron and ion interaction was described within the projector augmented wave (PAW) method.^{11,12} The k-space sampling and integration were done by adopting $8 \times 8 \times 8$ (for RbPbCO_3F and CsPbCO_3F), $6 \times 6 \times 14$ (for RbMgCO_3F) Gamma-centred k-mesh and using the linear tetrahedron method with Blöchl correction, respectively.¹³ All DFT calculations are performed on ordered fluorine structural variants (100% occupancy) with an averaged atomic position $(2/3, 1/3, 0)$ for RbPbCO_3F and $(0, 0, 1/2)$ for CsPbCO_3F .

For $\text{Nb}_2\text{O}_2\text{F}_3$, the calculations were performed by Dr. Jakoah Brgoch. The spin-polarized electronic structure was calculated for the monoclinic and triclinic structures. Exchange and correlation was described by the screened hybrid functional, HSE06,¹⁴ with the calculations employing Gamma-centered k-mesh grids of $6 \times 6 \times 4$ and $6 \times 6 \times 6$ for the monoclinic and triclinic structures, respectively, and a cutoff energy for the plane-wave basis set of 500 eV for both structures.

3.5 References

- (1) SAINT; 7.23A ed.; Bruker AXS Inst. Inc.: Madison, WI: 2005.
- (2) Sheldrick, G. M. In *Program for Solution of Crystal Structures*; University of Gottingen, Germany: 1997.
- (3) Sheldrick, G. M. In *Program for Refinement of Crystal Structures*; University of Gottingen, Germany: 1997.
- (4) Sheldrick, G. M. *Acta Crystallogr., Sect. A: Found. Crystallogr.* **2008**, *64*, 112.
- (5) Momma, K.; Izumi, F. *J. Appl. Crystallogr.* **2011**, *44*, 1272.
- (6) Ok, K. M.; Chi, E. O.; Halasyamani, P. S. *Chem. Soc. Rev.* **2006**, *35*, 710.
- (7) Kurtz, S. K.; Perry, T. T. *J. Appl. Phys.* **1968**, *39*, 3798.
- (8) Kresse, G.; Hafner, J. *Phys. Rev. B: Condens. Matter* **1993**, *47*, 558.
- (9) Kresse, G.; Furthmüller, J. *Computational Materials Science* **1996**, *6*, 15.
- (10) Perdew, J. P.; Ruzsinszky, A.; Csonka, G. I.; Vydrov, O. A.; Scuseria, G. E.; Constantin, L. A.; Zhou, X.; Burke, K. *Phys. Rev. Lett.* **2008**, *100*, 136406/1.
- (11) Blochl, P. E. *Phys. Rev. B: Condens. Matter* **1994**, *50*, 17953.
- (12) Kresse, G.; Joubert, D. *Phys. Rev. B: Condens. Matter Mater. Phys.* **1999**, *59*, 1758.
- (13) Blochl, P. E.; Jepsen, O.; Andersen, O. K. *Phys. Rev. B: Condens. Matter* **1994**, *49*, 16223.
- (14) Heyd, J.; Scuseria, G. E.; Ernzerhof, M. *J. Chem. Phys.* **2003**, *118*, 8207.

Chapter 4 Layered Compounds of Potassium Lead Fluorocarbonates $\text{KPb}_2(\text{CO}_3)_2\text{F}$ and $\text{K}_{2.70}\text{Pb}_{5.15}(\text{CO}_3)_5\text{F}_3$

This chapter is based on the results that has been published in “Tran, T. T.; Halasyamani, P. S., New Fluoride Carbonates: Centrosymmetric $\text{KPb}_2(\text{CO}_3)_2\text{F}$ and Noncentrosymmetric $\text{K}_{2.70}\text{Pb}_{5.15}(\text{CO}_3)_5\text{F}_3$, *Inorg. Chem.* **2013**, 52, 2466.”

4.1 Abstract

Two new layered potassium lead fluorocarbonates, $\text{KPb}_2(\text{CO}_3)_2\text{F}$ and $\text{K}_{2.70}\text{Pb}_{5.15}(\text{CO}_3)_5\text{F}_3$, have been synthesized and characterized. The materials were synthesized through solvothermal and conventional solid-state techniques. $\text{KPb}_2(\text{CO}_3)_2\text{F}$ and $\text{K}_{2.70}\text{Pb}_{5.15}(\text{CO}_3)_5\text{F}_3$ were structurally characterized by single crystal X-ray diffraction and exhibit two-dimensional crystal structures consisting of corner-shared PbO_6F and PbO_6F_2 polyhedra. $\text{K}_{2.70}\text{Pb}_{5.15}(\text{CO}_3)_5\text{F}_3$ is noncentrosymmetric, and crystallizes in the *achiral* and *non-polar* space group $P\bar{6}m2$ (crystal class $\bar{6}2m$). Powder second-harmonic generation measurements using 1064nm radiation revealed a SHG efficiency of approximately $40 \times \alpha\text{-SiO}_2$, whereas a charge constant, d_{33} , of approximately 20 pm/V was obtained through converse piezoelectric measurements. For the reported materials, infrared, UV-Vis, thermogravimetric and differential thermal analysis measurements were performed.

4.2 Introduction

Noncentrosymmetric (NCS) polar compounds have been of significant interest attributable to their technologically important properties such as ferroelectricity and pyroelectricity.¹⁻⁴ Other interesting functional properties of NCS but not necessarily polar structures are second-harmonic generation (SHG) and piezoelectricity.⁵⁻⁸ A number of approaches to the design and synthesis of new NCS materials have been reported.⁹⁻³³ We have focused on designing new NCS materials³⁴⁻⁴⁵ by using cations susceptible to second-order Jahn-Teller (SOJT) distortions: octahedrally coordinated d^0 transition-metal cations and lone-pair cations.⁴⁶⁻⁵⁰ Both families of cations are in asymmetric and locally polar coordination environments attributable to SOJT effects. With respect to contribution of anions to NCS structure, fluorocarbonates have attracted considerable attention over the last ten years as a result of the polarizability of the carbonate groups.⁵¹⁻⁵⁹ The polarizability of anisotropic carbonate group with a π -conjugated system is approximately five times greater than that of isotropic fluoride ion.⁶⁰⁻⁶¹ The difference in polarizability between these two anions could give rise to the formation of a macroscopically polar material.

A few NCS fluorocarbonates have been reported.^{51,62} SHG has been observed in $K_4Ln_2(CO_3)_3F_4$ (where Ln =Nd, Sm, Eu and Gd),⁶² with the largest efficiency reported for $K_4Eu_2(CO_3)_3F_4$. In addition, a family of NCS alkaline – alkaline-earth fluorocarbonates, $KSrCO_3F$, $RbSrCO_3F$, $KCaCO_3F$, $RbCaCO_3F$, $CsCaCO_3F$ and $Cs_3Ba_4(CO_3)_3F_5$ were reported recently.^{51,58} Of these materials, only $Cs_3Ba_4(CO_3)_3F_5$ is polar, whereas the others are non-polar and achiral. These materials have a wide

transparency in the UV, in the range of 200 – 800 nm, except for $\text{Cs}_3\text{Ba}_4(\text{CO}_3)_3\text{F}_5$ with a UV cut-off at approximately 210 nm. The alkaline – alkaline-earth fluorocarbonates are SHG active with efficiencies of $1 - 3 \times \text{KDP}$ ($40 - 120 \times \alpha\text{-SiO}_2$). Finally, transition metal fluorocarbonates, KCuCO_3F ,⁶³ BaMCO_3F_2 (where $\text{M} = \text{Mn}, \text{Cu}$ and Zn)^{56,64} and $\text{Ba}_2\text{Co}(\text{CO}_3)_2\text{F}_2$ ⁵⁴ have also been reported. Of these materials, only KCuCO_3F is NCS and polar, whereas the others are centrosymmetric. No SHG, piezoelectric, or polarization properties have been reported for KCuCO_3F .

We have been interested in investigating the association of a lone-pair cation, Pb^{2+} , and carbonate fluoride anions to couple their acentric features and thereby enhance the formation of a new NCS material. To date, no material in the $\text{A}^+ - \text{Pb}^{2+} - \text{CO}_3^{2-} - \text{F}^-$ system (where $\text{A}^+ = \text{Li}^+, \text{Na}^+, \text{K}^+, \text{Rb}^+$ or Cs^+) has been reported. Our investigation of $\text{K} - \text{Pb} - \text{CO}_3 - \text{F}$ system resulted in two new potassium lead fluorocarbonates, $\text{KPb}_2(\text{CO}_3)_2\text{F}$ and $\text{K}_{2.70}\text{Pb}_{5.15}(\text{CO}_3)_5\text{F}_3$. $\text{K}_{2.70}\text{Pb}_{5.15}(\text{CO}_3)_5\text{F}_3$ is NCS and crystallizes in achiral and non-polar space group $P\bar{6}m2$. In this chapter, the crystal structures, characterization and structure–property relationships of both materials are discussed. In addition, for $\text{K}_{2.70}\text{Pb}_{5.15}(\text{CO}_3)_5\text{F}_3$ we investigate its functional properties – SHG and piezoelectricity.

4.3 Experiments

Details of the synthesis and characterizations are presented in Chapter 3. Special descriptions of experiments for the $\text{KPb}_2(\text{CO}_3)_2\text{F}$ and $\text{K}_{2.70}\text{Pb}_{5.15}(\text{CO}_3)_5\text{F}_3$ materials are discussed in this section. Through hydrothermal reactions, colorless hexagonal plate-like crystals and block-shaped crystals, subsequently determined to be $\text{KPb}_2(\text{CO}_3)_2\text{F}$ and $\text{K}_{2.70}\text{Pb}_{5.15}(\text{CO}_3)_5\text{F}_3$, respectively, were obtained as a mixture in which the latter is the major phase - approximately 70%. The reported compounds are slightly hygroscopic, thus the products were stored in a vacuum desiccator. Polycrystalline $\text{KPb}_2(\text{CO}_3)_2\text{F}$ and $\text{K}_{2.70}\text{Pb}_{5.15}(\text{CO}_3)_5\text{F}_3$ were synthesized separately by conventional solid-state techniques. The materials were determined to be pure by powder X-ray diffraction.

There are some unusual features in the structure of $\text{K}_{2.70}\text{Pb}_{5.15}(\text{CO}_3)_5\text{F}_3$. The F(1) atom was found to be disordered about a $3m$ site. Initially the material was thought to be $\text{K}_3\text{Pb}_5(\text{CO}_3)_5\text{F}_3$, however the anisotropic displacement parameters of the K(2) cation in the double layer consistently refined to a non-positive definite value. Since K and Pb are the only heavy elements present, it was clear that there had to be a mix of these two elements at this position. Furthermore, since Pb^{2+} has twice the charge of K^+ there had to be a vacancy present for each Pb^{2+} cation in order to maintain charge balance. When a mixed occupancy model of 70(3)% K^+ /15(3)% Pb^{2+} /15(3)% vacancy was placed at the original 'K(2)' site, the overall model refined very nicely, resulting in a formula of $\text{K}_{2.70}\text{Pb}_{5.15}(\text{CO}_3)_5\text{F}_3$. Changing the amount of Pb present from 5 to 5.15 represents only a 3% increase, which is quite plausible under the reaction conditions. Also, this model results in a Pb:K ratio of 1.9 in $\text{K}_{2.70}\text{Pb}_{5.15}(\text{CO}_3)_5\text{F}_3$, that is not very different from the

ratio of 2.0 found in the co-crystallizing material $\text{KPb}_2(\text{CO}_3)_2\text{F}$. For verification purposes we collected data on a second crystal from the same batch, and the results of the two refinements were identical.

The semi-quantitative EDS measurements were taken three times from the same $\text{K}_{2.70}\text{Pb}_{5.15}(\text{CO}_3)_5\text{F}_3$ crystal that was used for X-ray diffraction analysis. The average Pb:K ratio of 1.94(3) found by EDS is in excellent agreement with the value of 1.91 determined by least squares refinement of the X-ray data. By contrast, if this site were fully occupied by K^+ , the Pb:K ratio would be 1.67.

With regard to the non-stoichiometric formula for $\text{K}_{2.70}\text{Pb}_{5.15}(\text{CO}_3)_5\text{F}_3$, there is precedence for partial substitution of Pb^{2+} at K^+ sites.⁶⁵⁻⁶⁶ Pb^{2+} has a six-coordinate effective ionic radius of 1.19 Å, that is only 10% smaller than K^+ (1.38 Å).⁸³ Thus both cations may occupy the same crystallographic site. Site disorder between Pb^{2+} and K^+ has been reported in KPb_2Cl_5 and $\text{Na}_{2-x}\text{K}_x\text{Pb}_{11}\text{F}_{18}\text{X}_6$ ($\text{X}=\text{Cl}, \text{Br}$).⁶⁵⁻⁶⁶ There is also no structural issue with having a partial vacancy at this site since the double-layer skeleton, composed of planes of $\text{Pb}(\text{CO}_3)$ linked by F, is quite rigid (Figure 4.2). The double-layer framework is not perturbed in any significant way by the absence of a cation in the cavities 15% of the time, as evidenced by comparison with the fully occupied double-layer in $\text{KPb}_2(\text{CO}_3)_2\text{F}$. Note that the *a* and *b* unit cell dimensions in both materials are virtually identical (5.3000(2) Å vs. 5.3123(5) Å) - a function of the $\text{Pb}(\text{CO}_3)$ bonding pattern (see Figure 4.1a) - and the Pb-F distances in the double-layers are also essentially the same (2.3327(3) Å vs. 2.3478(8) Å). The thermal displacement parameters of our structure refinement are represented in Figure 4.3.

Relevant crystallographic data, selected bond distances and angles, atomic coordinates and equivalent isotropic displacement parameters for $\text{KPb}_2(\text{CO}_3)_2\text{F}$ and $\text{K}_{2.70}\text{Pb}_{5.15}(\text{CO}_3)_5\text{F}_3$ are given in Tables 4.1 – 4.4.

Table 4.1 Crystallographic data for $\text{KPb}_2(\text{CO}_3)_2\text{F}$ and $\text{K}_{2.70}\text{Pb}_{5.15}(\text{CO}_3)_5\text{F}_3$

	$\text{KPb}_2(\text{CO}_3)_2\text{F}$	$\text{K}_{2.70}\text{Pb}_{5.15}(\text{CO}_3)_5\text{F}_3$
M/gmol ⁻¹	592.50	1529.65
T/K	296(2)	301(2)
$\lambda/\text{Å}$	0.71073	0.71073
Crystal system	Hexagonal	Hexagonal
Space group	$P6_3/mmc$ (No. 194)	$P\bar{6}m2$ (No. 187)
$a/\text{Å}$	5.3000(2)	5.3123(5)
$b/\text{Å}$	5.3000(2)	5.3123(5)
$c/\text{Å}$	13.9302(8)	18.6203(17)
α/deg	90	90
β/deg	90	90
γ/deg	120	120
$V/\text{Å}^3$	338.88(3)	455.07(7)
Z	2	1
d_c/gcm^{-3}	5.807	5.582
μ/mm^{-1}	50.237	48.194
$2\theta_{\text{max}}/^\circ$	58.48	54.70
R_{int}	0.0471	0.0478
GOF	1.340	1.159
$R(\text{F})^a$	0.0187	0.0207
$R_w(\text{F}_o^2)^b$	0.0512	0.0598
Flack parameter	N/A	0.012(18)

$$^a R(\text{F}) = \frac{\sum ||F_o| - |F_c||}{\sum |F_o|}$$

$$^b R_w(\text{F}_o^2) = \left[\frac{\sum w(\text{F}_o^2 - \text{F}_c^2)^2}{\sum w(\text{F}_o^2)^2} \right]^{1/2}$$

Table 4.2 Selected bond distances (Å) and angles (deg) for $\text{KPb}_2(\text{CO}_3)_2\text{F}$ and $\text{K}_{2.70}\text{Pb}_{5.15}(\text{CO}_3)_5\text{F}_3$

$\text{KPb}_2(\text{CO}_3)_2\text{F}$		$\text{K}_{2.70}\text{Pb}_{5.15}(\text{CO}_3)_5\text{F}_3$	
Pb(1) – O(1) × 6	2.6829(6)	Pb(1) – O(1) × 6	2.6668(9)
Pb(1) – F(1)	2.3327(3)	Pb(1) – F(1) × 2	2.454(9)
C(1) – O(1) × 3	1.277(3)	Pb(2) – O(2) × 6	2.6918(11)
O(1) – Pb(1) – O(1)	48.68(15)	Pb(2) – F(1)	2.254(10)
O(1) – Pb(1) – O(1)	70.28(15)	Pb(3) – O(3) × 6	2.6926(11)
F(1) – Pb(1) – O(1)	82.86(9)	Pb(3) – F(2)	2.3478(8)
Pb(1) – F(1) – Pb(1)	180.00	C(1) – O(1) × 3	1.296(9)
		C(2) – O(2) × 3	1.293(7)
		C(3) – O(3) × 3	1.282(7)
		O(1) – Pb(1) – O(1)	49.8(4)
		O(1) – Pb(1) – O(1)	70.2(4)
		F(1) – Pb(1) – O(1)	89.55(7)
		F(1) – Pb(1) – F(1)	175.0(7)
		O(2) – Pb(2) – O(2)	49.2(3)
		O(2) – Pb(2) – O(2)	69.6(3)
		F(1) – Pb(2) – O(2)	81.76(15)
		O(3) – Pb(3) – O(3)	48.7(3)
		O(3) – Pb(3) – O(3)	70.1(3)
		F(2) – Pb(3) – O(3)	82.25(14)
		Pb(1) – F(1) – Pb(2)	169.5(16)

Table 4.3 Atomic coordinates and equivalent isotropic displacement parameters (\AA^2) for $\text{KPb}_2(\text{CO}_3)_2\text{F}$.

Atom	x	y	z	U_{eq}^a
K	0.6667	0.3333	0.2500	0.017(1)
Pb	0.3333	0.6667	0.4175(1)	0.017(1)
C	0.0000	0.0000	0.3926(5)	0.017(1)
O	0.2782(7)	0.1391(4)	0.3935(3)	0.022(1)
F	0.3333	0.6667	0.2500	0.025(2)

^a U_{eq} is defined as one-third of the trace of the orthogonalized U_{ij} tensor

Table 4.4 Atomic coordinates and equivalent isotropic displacement parameters (\AA^2) for $\text{K}_{2.70}\text{Pb}_{5.15}(\text{CO}_3)_5\text{F}_3$

Atom	x	y	z	S.O.F	U_{eq}^a
K(1)	0.3333	0.6667	0.3796(2)	1.0	0.021(1)
Pb(1)	0.6667	0.3333	0.5000	1.0	0.015(1)
Pb(2)	0.6667	0.3333	0.2482(1)	1.0	0.015(1)
Pb(3)	0.3333	0.6667	0.1261(1)	1.0	0.017(1)
K(2)/ Pb(4)	0.6667	0.3333	0.0000	0.70(3)/ 0.15(3)	0.020(1)
C(1)	1.0000	0.0000	0.5000	1.0	0.022(9)
C(2)	1.0000	0.0000	0.2666(11)	1.0	0.011(4)
C(3)	0.0000	1.0000	0.1077(12)	1.0	0.015(5)
O(1)	1.1408(10)	0.2816(20)	0.5000	1.0	0.025(2)
O(2)	1.1405(7)	0.2811(15)	0.2678(3)	1.0	0.023(2)
O(3)	-0.1393(7)	0.7214(15)	0.1066(3)	1.0	0.022(2)
F(1)	0.6433(30)	0.3567(30)	0.3687(5)	1.0	0.025(5)
F(2)	0.3333	0.6667	0.0000	1.0	0.020(3)

^a U_{eq} is defined as one-third of the trace of the orthogonalized U_{ij} tensor.

4.4 Results and Discussion

4.4.1 Structures

KPb₂(CO₃)₂F exhibits a two-dimensional crystal structure that consists of double-layers of Pb(CO₃)₃F polyhedra (see Figure 4.1). The Pb²⁺ cations are connected by carbonate groups in the *ab*-plane, whereas along the *c*-axis direction the connectivity is through a bridging fluoride. The K⁺ cations are located in the cavities formed between Pb(CO₃)₃F polyhedral blocks. The double-layers are staggered about the *c*-axis to minimize Pb²⁺ lone-pair – lone-pair interactions. In connectivity terms, the material may be written as {2[PbO_{6/3}F_{1/2}]^{5/2-} 2[CO_{3/3}]²⁺}¹⁻, with charge balance maintained by one K⁺ cation. Each Pb²⁺ cation in PbO₆F is bonded to six oxygen atoms and one fluorine atom in a distorted hexagonal pyramidal coordination environment, with Pb–O distances of 2.6829(6) Å and a Pb–F distance 2.3327(3) Å. The carbonate C–O distance is 1.277(3) Å. The K⁺ cation is surrounded by six oxygen atoms with K–O distances of 2.679(4) Å. Bond valence calculations resulted in values of 1.36, 1.72, and 4.05 for K⁺, Pb²⁺, and C⁴⁺, respectively (Table 4.5).⁶⁷⁻⁶⁸ The thermal displacement parameters of KPb₂(CO₃)₂F are represented in Figure 4.3.

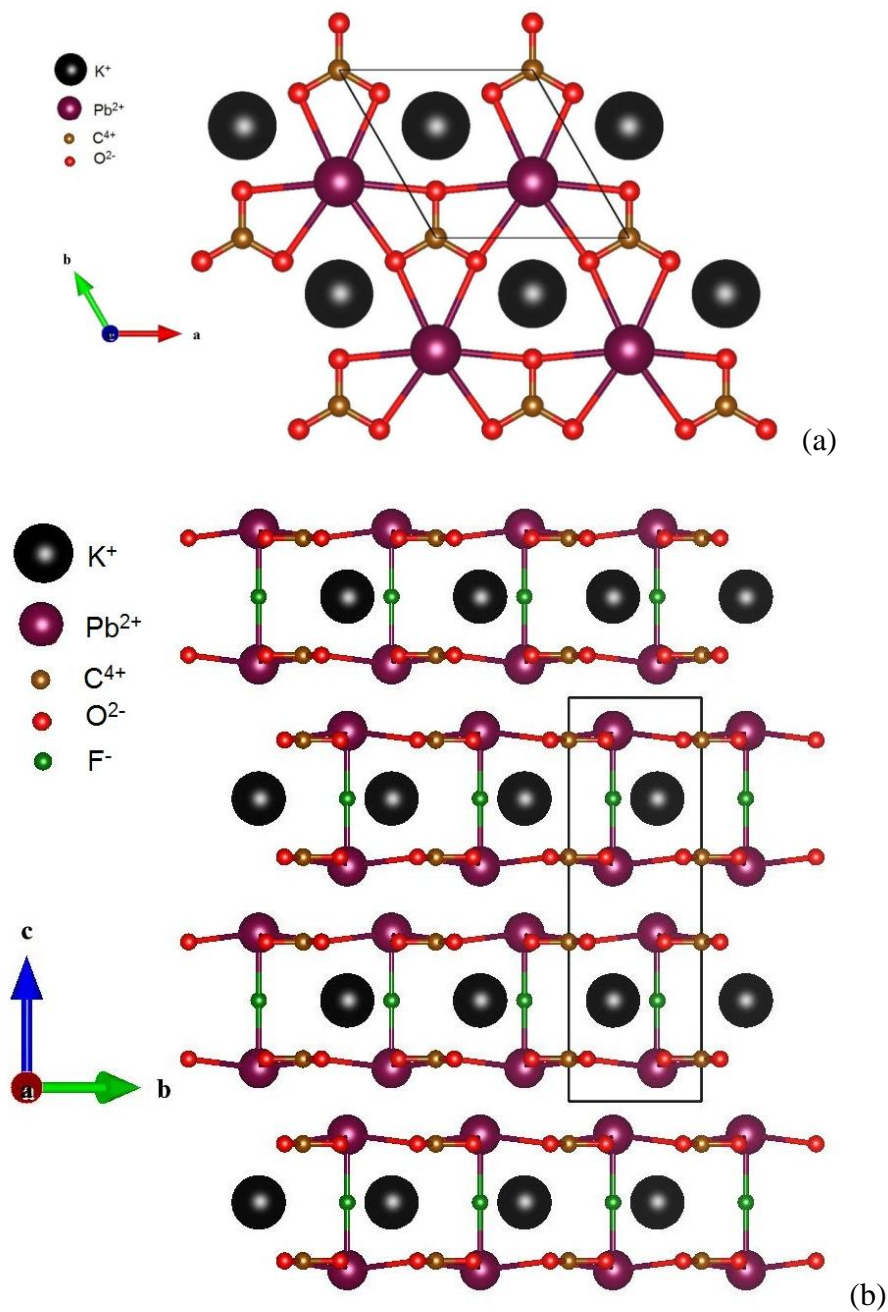


Figure 4.1 Ball-and-stick representation of a single $\text{Pb}(\text{CO}_3)$ layer in the ab -plane and the K^+ cations beneath this layer (a). Ball-and-stick representations of $\text{KPb}_2(\text{CO}_3)_2\text{F}$ in the bc -plane (b). Note that the double-layers are staggered to possibly minimize lone-pair – lone-pair interactions.

$\text{K}_{2.70}\text{Pb}_{5.15}(\text{CO}_3)_5\text{F}_3$ also exhibits a two-dimensional structure that consists of double-layers of $\text{Pb}(\text{CO}_3)_3\text{F}$ polyhedra and triple-layers of $\text{Pb}(\text{CO}_3)_3\text{F}$ and $\text{Pb}(\text{CO}_3)_3\text{F}_2$ polyhedra (see Figure 4.2). The double-layer alternates with the triple-layer, stacking along the c direction. The Pb^{2+} cations are connected by carbonate groups in the ab -plane, and along the c -axis direction the connectivity is through a bridging fluoride. In the triple-layer, the K^+ cations are located in cavities formed between the $\text{Pb}(\text{CO}_3)_3\text{F}$ and $\text{Pb}(\text{CO}_3)_3\text{F}_2$ polyhedral blocks. In the double-layer the bridging fluoride F(2) is ordered, whereas in the triple layer the bridging fluoride F(1) is statistically disordered with a Pb–F–Pb angle of $169.5(16)^\circ$. The $\text{Pb}(2)^{2+}$ and $\text{Pb}(3)^{2+}$ cations in PbO_6F are in distorted hexagonal pyramidal coordination environments with Pb(2)–O(2) (Pb(3)–O(3)) distances of $2.6918(11)\text{Å}$ ($2.6926(11)\text{Å}$), and Pb(2)–F(1) (Pb(3)–F(2)) distances $2.254(10)\text{Å}$ ($2.3478(8)\text{Å}$). The $\text{Pb}(1)^{2+}$ cation in PbO_6F_2 is found in a distorted hexagonal bipyramidal environment with Pb(1)–O(1) distances of $2.6668(9)\text{Å}$ and Pb(1)–F(1) distances $2.454(9)\text{Å}$. As would be expected, the outer Pb(2)–F(1) distance is considerably shorter than the central Pb(1)–F(1) distance. The K^+ cations are surrounded by six oxygen atoms with K–O distances that range between $2.669(7)\text{Å}$ and $2.858(7)\text{Å}$. The C–O bond distances range from $1.282(7)$ to $1.296(9)\text{Å}$. Bond valence sum calculations resulted in values of 1.01, 1.67 – 1.97, and 3.87 – 4.02 for K^+ , Pb^{2+} and C^{4+} , respectively (Table 4.6).⁶⁷⁻⁶⁸ The thermal displacement parameters of $\text{K}_{2.70}\text{Pb}_{5.15}(\text{CO}_3)_5\text{F}_3$ are represented in Figure 4.3.

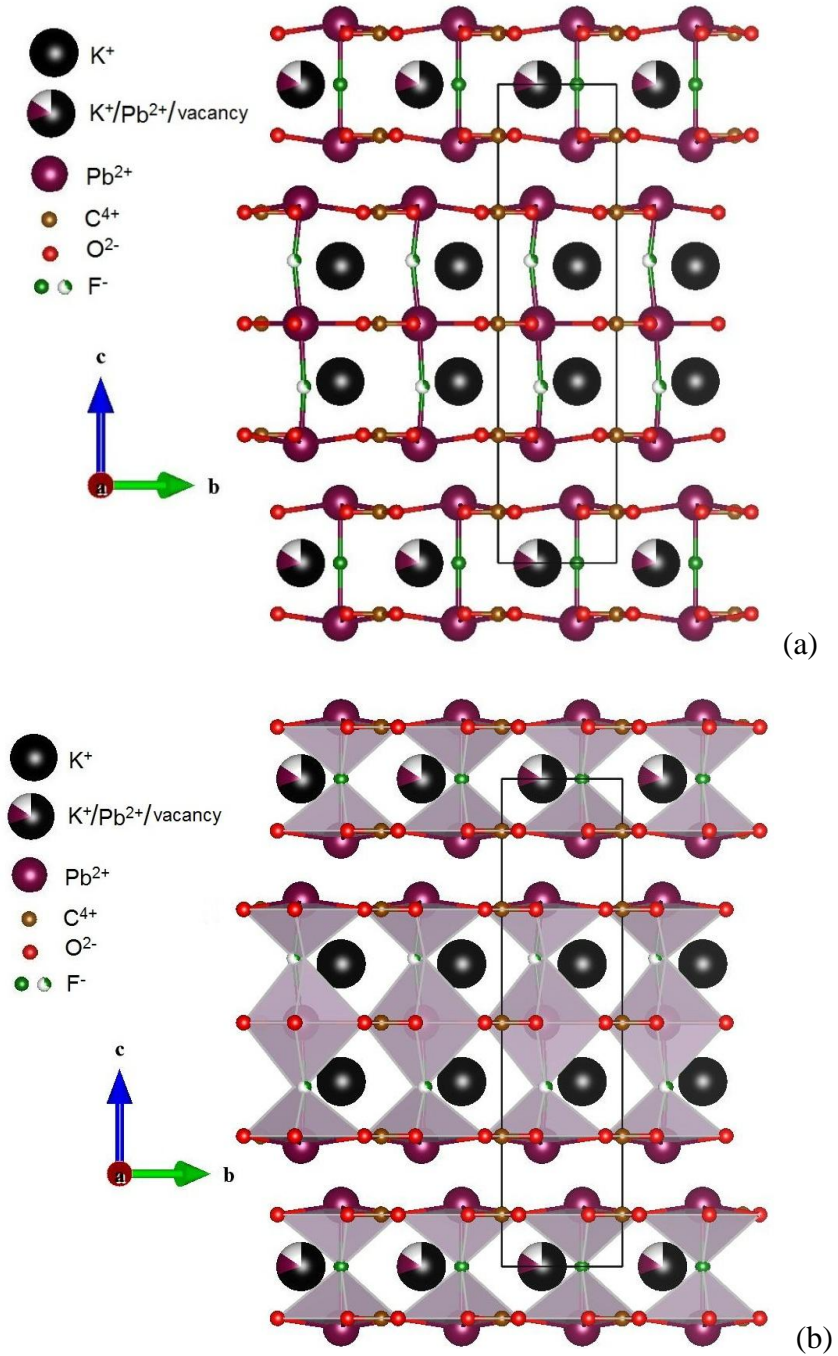


Figure 4.2 Ball-and-stick (a) and polyhedral (b) representations of $\text{K}_{2.70}\text{Pb}_{5.15}(\text{CO}_3)_5\text{F}_3$ in the bc -plane. Only one position of the disordered bridging fluoride in the triple layer is shown.

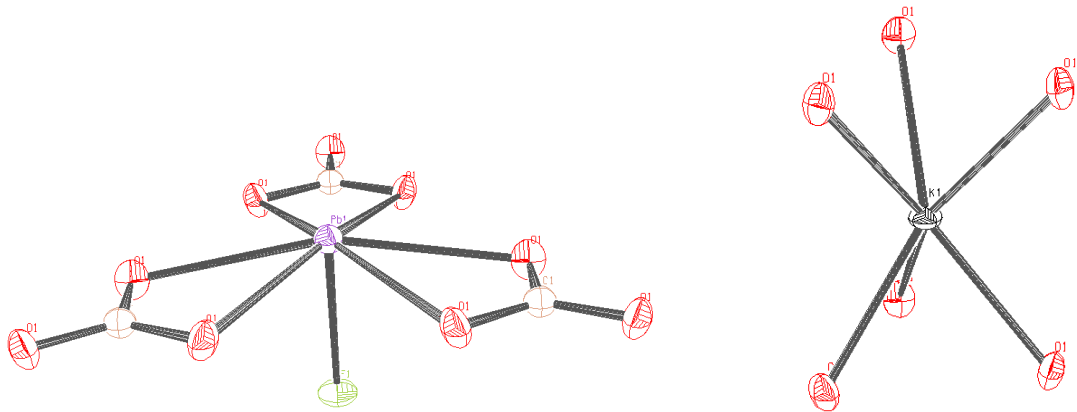


Figure 4.3 ORTEP (50% probability ellipsoids) diagrams of $\text{KPb}_2(\text{CO}_3)_2\text{F}$

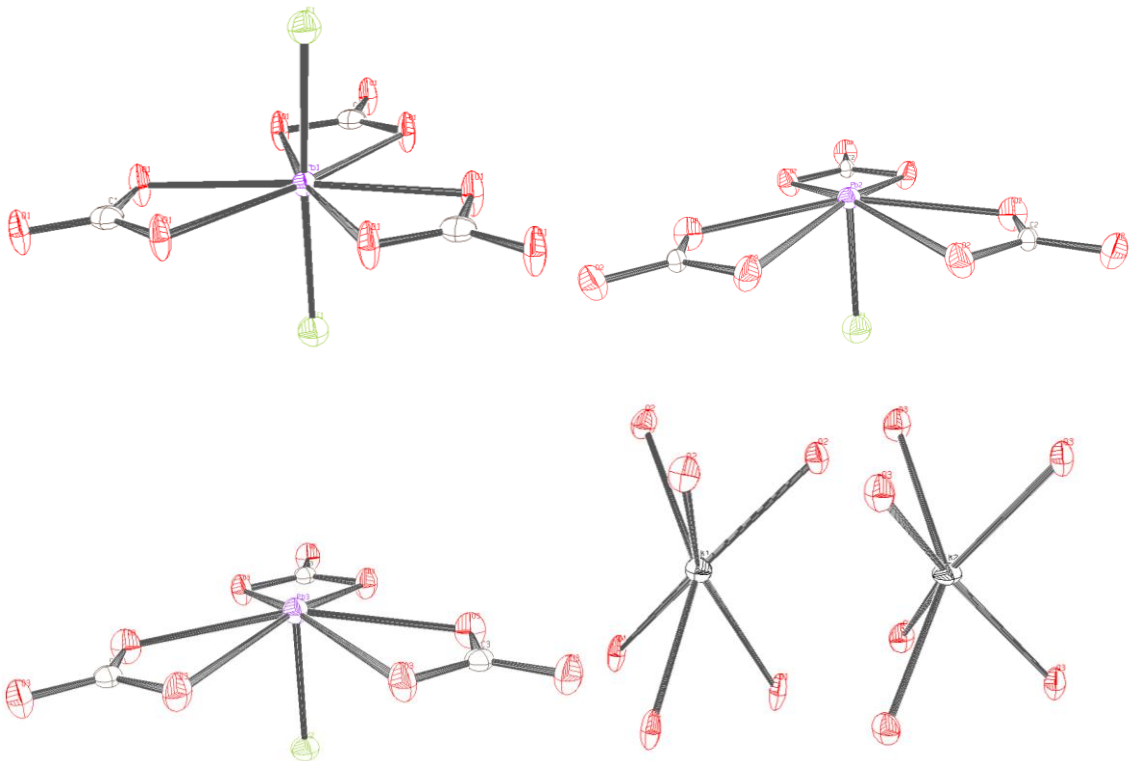


Figure 4.3 ORTEP (50% probability ellipsoids) diagrams of $\text{K}_{2.70}\text{Pb}_{5.15}(\text{CO}_3)_5\text{F}_3$

The role of the planar carbonate group with respect to the rest of the structure has been described earlier.⁶⁹⁻⁷¹ In fluorocarbonates, the carbonate group may be flat (parallel) or inclined (on-edge) with respect to the overall structure. In both $\text{KPb}_2(\text{CO}_3)_2\text{F}$ and $\text{K}_{2.70}\text{Pb}_{5.15}(\text{CO}_3)_5\text{F}_3$, the planar carbonate groups are parallel to the structural layers. This is similar to other reported fluoride carbonates such as $\text{NaBaCe}_2(\text{CO}_3)_4\text{F}$ ⁷² and $\text{BaCe}(\text{CO}_3)_2\text{F}$.⁷³ Along the *c*-axis, the planar carbonate groups are eclipsed within the double ($\text{KPb}_2(\text{CO}_3)_2\text{F}$) and triple-layer ($\text{K}_{2.70}\text{Pb}_{5.15}(\text{CO}_3)_5\text{F}_3$) blocks, but are staggered between blocks. One interesting feature of the outer $\text{Pb}(\text{CO}_3)\text{F}$ layers is that the CO_3 groups are not in the plane of the Pb atoms, but instead are pushed in towards the interior of the layers (see Figure 4.4). The CO_3 planes are offset by about 0.36 Å from the Pb planes. This is most likely caused by steric repulsion from the lone-pair of electrons on the Pb atoms. The Pb–O distances in the outer $\text{Pb}(\text{CO}_3)\text{F}$ layers are longer than that in the central $\text{Pb}(\text{CO}_3)_2\text{F}$ layers in $\text{K}_{2.70}\text{Pb}_{5.15}(\text{CO}_3)_5\text{F}_3$ attributable to the offset position of the CO_3 groups.

In both materials the asymmetric coordination environments of the outer Pb^{2+} atoms of each layer are polar, *i.e.*, each PbO_6F polyhedron exhibits a local dipole moment. Since both double-layers and triple-layers are composed of PbO_6F polyhedra with equal and opposite polarizations, the net dipole moments in $\text{KPb}_2(\text{CO}_3)_2\text{F}$ and $\text{K}_{2.70}\text{Pb}_{5.15}(\text{CO}_3)_5\text{F}_3$ are zero. Therefore, the structures are macroscopically not polar.

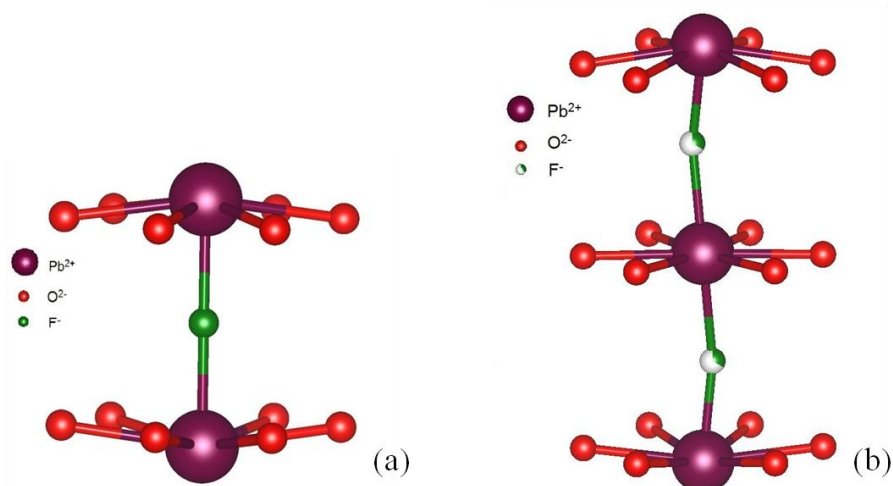


Figure 4.4 Ball-and-stick representation of (a) the double-layer unit consisting of two PbO_6F distorted hexagonal pyramids and (b) the triple-layer unit consisting of two PbO_6F distorted hexagonal pyramids alternating with one PbO_6F_2 distorted hexagonal bipyramid.

A common feature for $\text{KPb}_2(\text{CO}_3)_2\text{F}$ and $\text{K}_{2.70}\text{Pb}_{5.15}(\text{CO}_3)_5\text{F}_3$ is the occurrence of double-layers of PbO_6F distorted hexagonal pyramidal polyhedra (see Figure 4.4a). Although single-layer PbO_6F distorted hexagonal pyramidal polyhedra have been previously observed in $\text{BaPb}_2(\text{CO}_3)_2\text{F}_2$,^{52,59} the materials in this report are the first examples of double-layer and triple-layer polyhedra composed of distorted hexagonal pyramidal PbO_6F and distorted hexagonal bipyramidal PbO_6F_2 (see Figure 4.4). Analogous distorted hexagonal bipyramidal AO_6F_2 ($\text{A} = \text{Sr}^{2+}$ or Ca^{2+}) polyhedra have been observed previously in KSrCO_3F , RbSrCO_3F , and KCaCO_3F .⁵¹⁻⁵² Thus, the central Pb^{2+} cation in the triple-layer may be considered to have an inert rather than stereo-active lone-pair, *i.e.*, the lone-pair is more spherical. A stereo-active lone-pair on Pb^{2+} can be found in the double-layer in both materials, as well as in the outer distorted hexagonal pyramidal PbO_6F polyhedra of the triple-layer. In order to visualize the lone-pair on the

Pb^{2+} cations, ELF calculations were performed using the VASP package⁷⁴⁻⁷⁵ with PBE exchange-correlation functional,⁷⁶ and an $\eta = 0.5$ (see Figure 4.5).⁷⁴

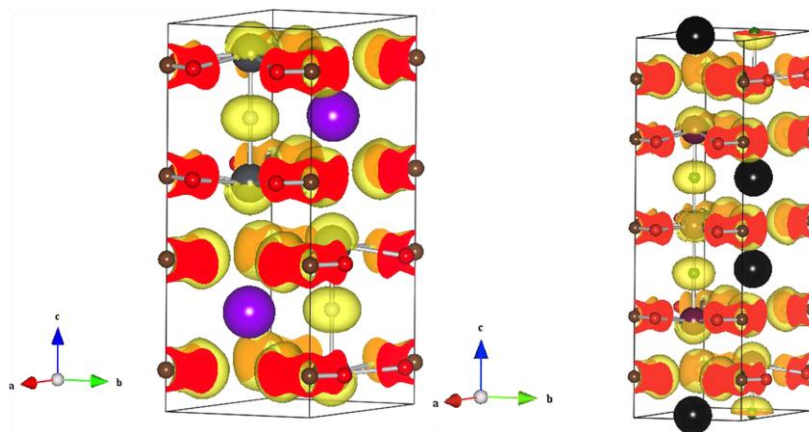


Figure 4.5 ELF diagram, $\eta = 0.5$, of the double-layer in $\text{KPb}_2(\text{CO}_3)_2\text{F}$ (left) and the triple-layer in $\text{K}_{2.70}\text{Pb}_{5.15}(\text{CO}_3)_5\text{F}_3$ (right). Note that the central Pb^{2+} cation has an inert lone-pair, whereas the ‘capping’ Pb^{2+} cations exhibit a stereo-active lone-pair.

The double-layer units in both $\text{KPb}_2(\text{CO}_3)_2\text{F}$ and $\text{K}_{2.70}\text{Pb}_{5.15}(\text{CO}_3)_5\text{F}_3$ are structurally the same, consisting of two nearly planar arrangements of $\text{Pb}(\text{CO}_3)$ linked by bridging F atoms. The CO_3 groups in each layer are in an eclipsed configuration when viewed down the c -axis, which is necessitated by the large cations in the cavities between layers. Careful inspection of this eclipsed double-layer structure indicates that it is not possible for this building unit to reside on an inversion center since the F and K atoms have trigonal symmetry in the ab -plane with respect to each other. Thus it is impossible for an ordered arrangement to have an inversion center at any site in this plane. Similarly the triple-layer unit in $\text{K}_{2.70}\text{Pb}_{5.15}(\text{CO}_3)_5\text{F}_3$ cannot possibly reside on an inversion center since the central Pb and C atoms have trigonal symmetry in the ab -plane. The double and

triple-layers that comprise both of these compounds are inherently NCS. Therefore the only way for these materials to pack in a centrosymmetric arrangement is for there to be an inversion center between the individual multi-layer sheets. In $\text{KPb}_2(\text{CO}_3)_2\text{F}$ there is an inversion center between each of the double-layers, and the space group is centrosymmetric – $P6_3/mmc$. However there is no way to form an inversion center between the alternating double and triple-layers of $\text{K}_{2.70}\text{Pb}_{5.15}(\text{CO}_3)_5\text{F}_3$, and therefore this material necessarily crystallizes in a NCS space group – $P\bar{6}m2$.

Table 4.5 Bond valence analysis for $\text{KPb}_2(\text{CO}_3)_2\text{F}^a$

Atom	O	F	Σ cations
K	0.226 ^[×6]		1.36
Pb	0.214 ^[×6]	0.441 ^[×2]	1.72
C	1.35 ^[×3]		4.05
Σanions	1.79	0.882	

^a Bond valence sums calculated with the formula: $S_i = \exp[(R_0 - R_i)/B]$, where S_i =valence of bond “ i ” and $B=0.37$.

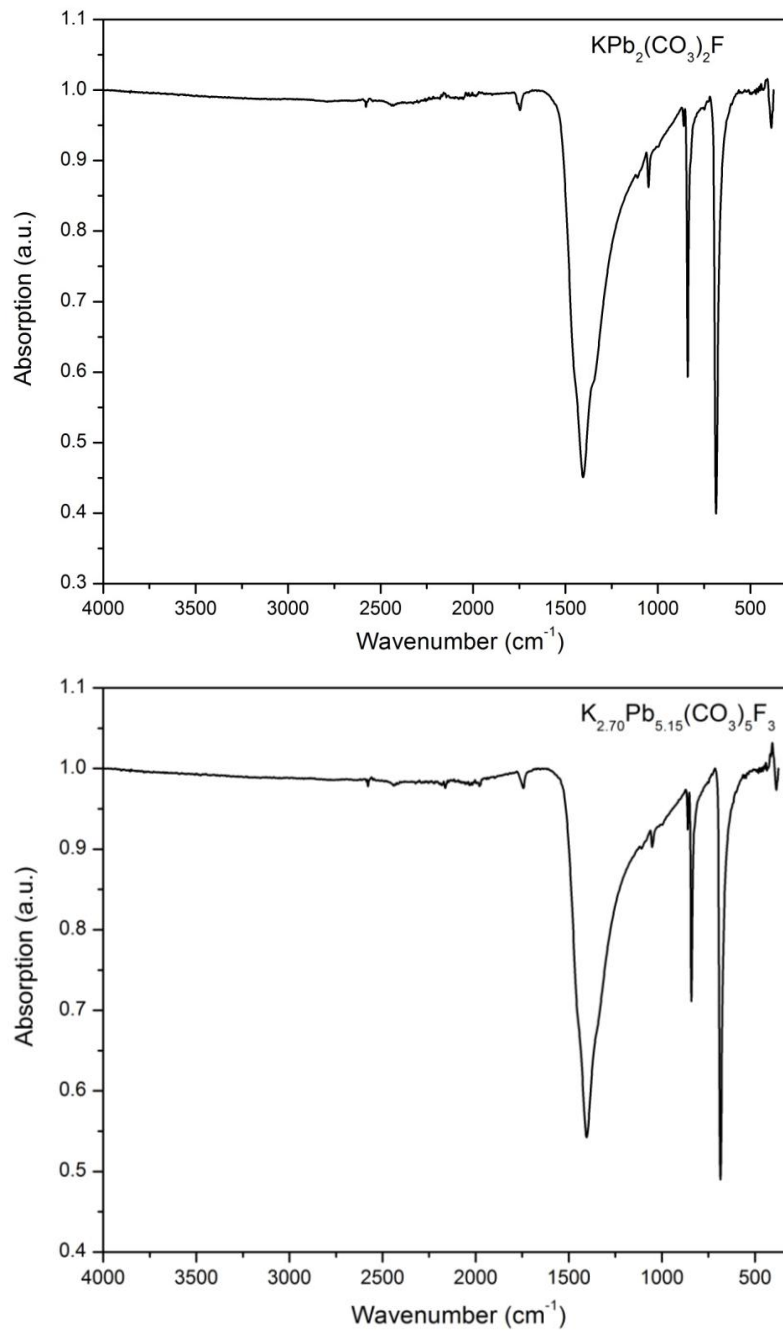
Table 4.5 Bond valence analysis for $\text{K}_{2.70}\text{Pb}_{5.15}(\text{CO}_3)_5\text{F}_3^a$

Atom	O(1)	O(2)	O(3)	F(1)	F(2)	Σ cations
K(1)	0.141 ^[×3]	0.196 ^[×3]				1.01
K(2) 70%			0.234 ^[×6]			1.18
Pb(4) 15%			0.222 ^[×6]			
Pb(1)	0.223 ^[×6]			0.318 ^[×2]		1.97
Pb(2)		0.209 ^[×6]		0.546		1.80
Pb(3)			0.208 ^[×6]		0.424 ^[×2]	1.67
C(1)	1.29 ^[×3]					3.87
C(2)						3.90
C(3)		1.30 ^[×3]	1.34 ^[×3]			4.02
Σanions	1.65	1.70	1.74	0.864	0.848	

^a Bond valence sums calculated with the formula: $S_i = \exp[(R_0 - R_i)/B]$, where S_i =valence of bond “ i ” and $B=0.37$.

4.4.2 Infrared (IR) Spectroscopy

The IR spectra of $\text{KPb}_2(\text{CO}_3)_2\text{F}$ and $\text{K}_{2.70}\text{Pb}_{5.15}(\text{CO}_3)_5\text{F}_3$ revealed C–O vibrations between $1400 - 680 \text{ cm}^{-1}$. The strong broad bands observed at 1398 and 1400 cm^{-1} can be assigned to the stretching C–O vibrations. The out-of-plane vibration, $\delta(\text{OCO})$, is observed in the range of $850 - 830 \text{ cm}^{-1}$ as a medium band, and the bending vibration, $\delta(\text{OCO})$, should appear at $720 - 680 \text{ cm}^{-1}$ as a medium weak band.⁷⁷⁻⁸⁰ A strong band, however, was observed in the range of $720 - 680 \text{ cm}^{-1}$ which can be attributed to the overlap between the bending vibration, $\delta(\text{OCO})$, and the stretching vibration, $\nu(\text{Pb-O})$.⁷⁹⁻
⁸⁰ The $\nu(\text{Pb-F})$ vibration is observed at $\sim 400 \text{ cm}^{-1}$.⁸⁰ The infrared spectra are depicted in the Figure 4.6.



	$\nu(\text{C-O})$	$\delta(\text{OCO})$	$\nu(\text{Pb-F})$
$\text{KPb}_2(\text{CO}_3)_2\text{F}$	1398, 1041	845, 692	407
$\text{K}_{2.70}\text{Pb}_{5.15}(\text{CO}_3)_5\text{F}_3$	1400, 1037	836, 680	402

Figure 4.6 IR spectra of $\text{KPb}_2(\text{CO}_3)_2\text{F}$ and $\text{K}_{2.70}\text{Pb}_{5.15}(\text{CO}_3)_5\text{F}_3$

4.4.3 UV-Vis Diffuse Reflectance Spectroscopy

The UV-Vis diffuse reflectance spectra revealed that the absorption energies for $\text{KPb}_2(\text{CO}_3)_2\text{F}$ and $\text{K}_{2.70}\text{Pb}_{5.15}(\text{CO}_3)_5\text{F}_3$ are approximately 3.9 eV and 3.8 eV, respectively. This is consistent with the white color of the materials. Absorption (K/S) data were calculated from the Kubelka-Munk function.⁸¹⁻⁸²

$$F(R) = \frac{(1-R)^2}{2R} = \frac{K}{S}$$

where R represents the reflectance, K the absorption coefficient, and S the scattering factor. In a K/S versus E (eV) plot, extrapolating the linear part of the rising curve to zero resulted the onset of absorption at 3.9 eV and 3.8 eV. The UV-Vis diffuse reflectance spectra are presented in Figure 4.7.

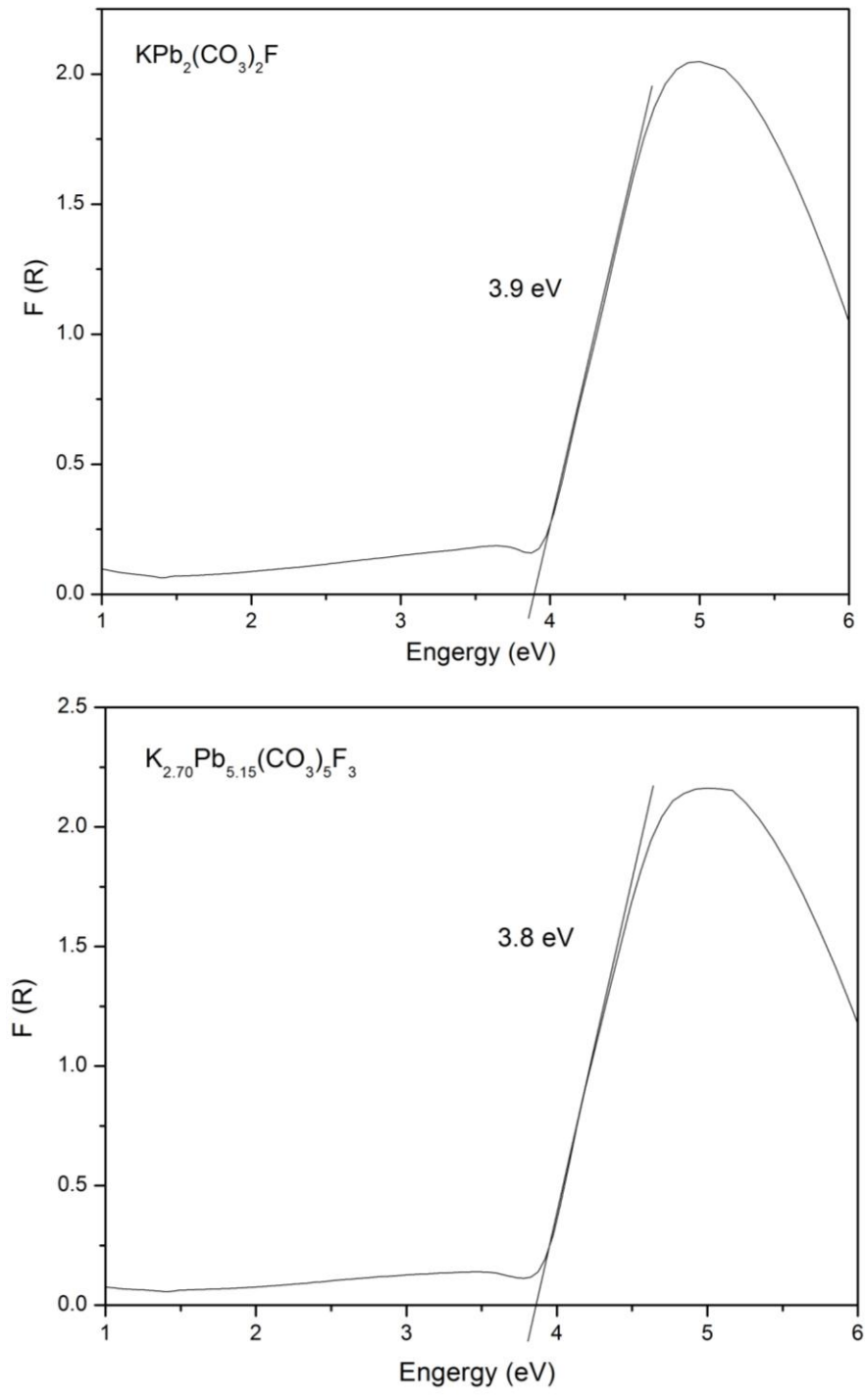


Figure 4.7 UV-Vis diffuse reflectance spectra of $\text{KPb}_2(\text{CO}_3)_2\text{F}$ and $\text{K}_{2.70}\text{Pb}_{5.15}(\text{CO}_3)_5\text{F}_3$

4.4.4 Thermal Analysis

The thermal behaviors of $\text{KPb}_2(\text{CO}_3)_2\text{F}$ and $\text{K}_{2.70}\text{Pb}_{5.15}(\text{CO}_3)_5\text{F}_3$ were investigated using thermogravimetric analysis (TGA) and differential thermal analysis (DTA) under N_2 atmosphere. The decomposition of both materials begins at approximately 290°C , corresponding to the loss of CO_2 . The experimental weight loss is in good agreement with the calculated weight loss. The endothermic peaks in the heating curve are consistent with the decomposition of the materials. The exothermic peaks in the cooling cycle indicate re-crystallization of the residues. At approximately 830°C , weight loss was observed that is likely attributable to the loss of fluorides. Powder XRD data of the residuals revealed PbO and unidentified phases. The DTA/TGA diagrams for $\text{KPb}_2(\text{CO}_3)_2\text{F}$ and $\text{K}_{2.70}\text{Pb}_{5.15}(\text{CO}_3)_5\text{F}_3$ are depicted in Figure 4.8.

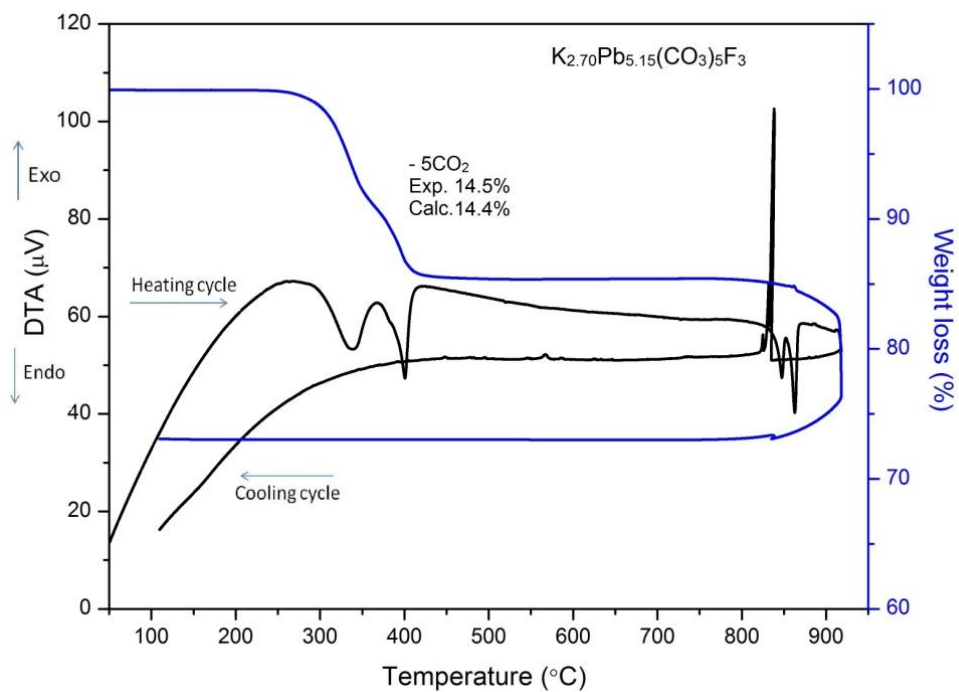
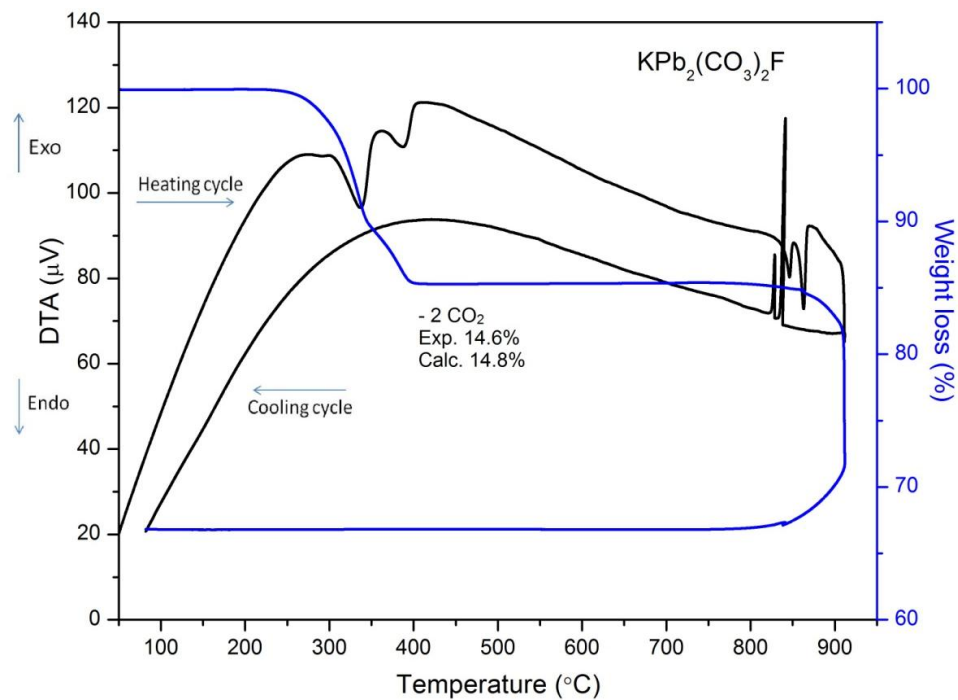


Figure 4.8 Thermogravimetric analysis and differential thermal analysis diagram of $\text{KPb}_2(\text{CO}_3)_2\text{F}$ and $\text{K}_{2.70}\text{Pb}_{5.15}(\text{CO}_3)_5\text{F}_3$ under N_2

4.4.5 Second-Harmonic Generation (SHG) and Piezoelectric Measurements

Since $\text{K}_{2.70}\text{Pb}_{5.15}(\text{CO}_3)_5\text{F}_3$ crystallizes in the NCS space group $P\bar{6}m2$, we investigated the SHG and piezoelectric properties. Powder SHG measurements using 1064nm radiation revealed a SHG efficiency of approximately $40 \times \alpha\text{-SiO}_2$ ($1 \times \text{KDP}$) in the 45–63 μm particle size range. Additional SHG measurements, particle size vs. SHG efficiency, indicate $\text{K}_{2.70}\text{Pb}_{5.15}(\text{CO}_3)_5\text{F}_3$ exhibits type 1 phase-matching behavior. As such $\text{K}_{2.70}\text{Pb}_{5.15}(\text{CO}_3)_5\text{F}_3$ falls into the class B category of SHG materials, as defined by Kurtz and Perry (see Figure 4.9).⁶⁴ Converse piezoelectric measurements were also performed and a piezoelectric charge constant, d_{33} , of approximately 20 pm/V was determined (see Figure 4.10).

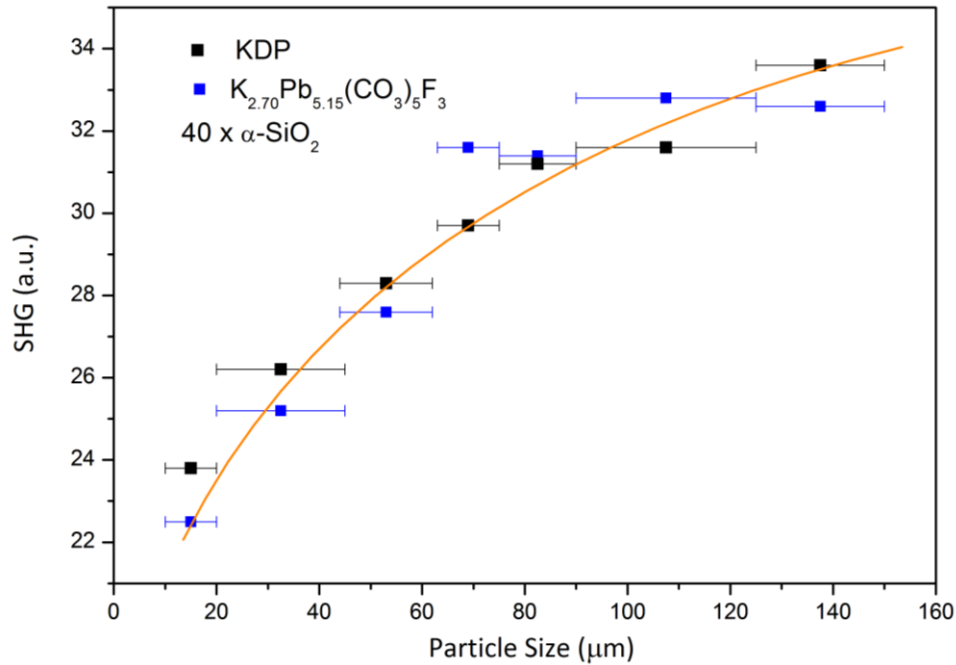


Figure 4.9 Powder second-harmonic generation for $\text{K}_{2.70}\text{Pb}_{5.15}(\text{CO}_3)_5\text{F}_3$. A curve is drawn to guide the eye and is not a fit to the data.

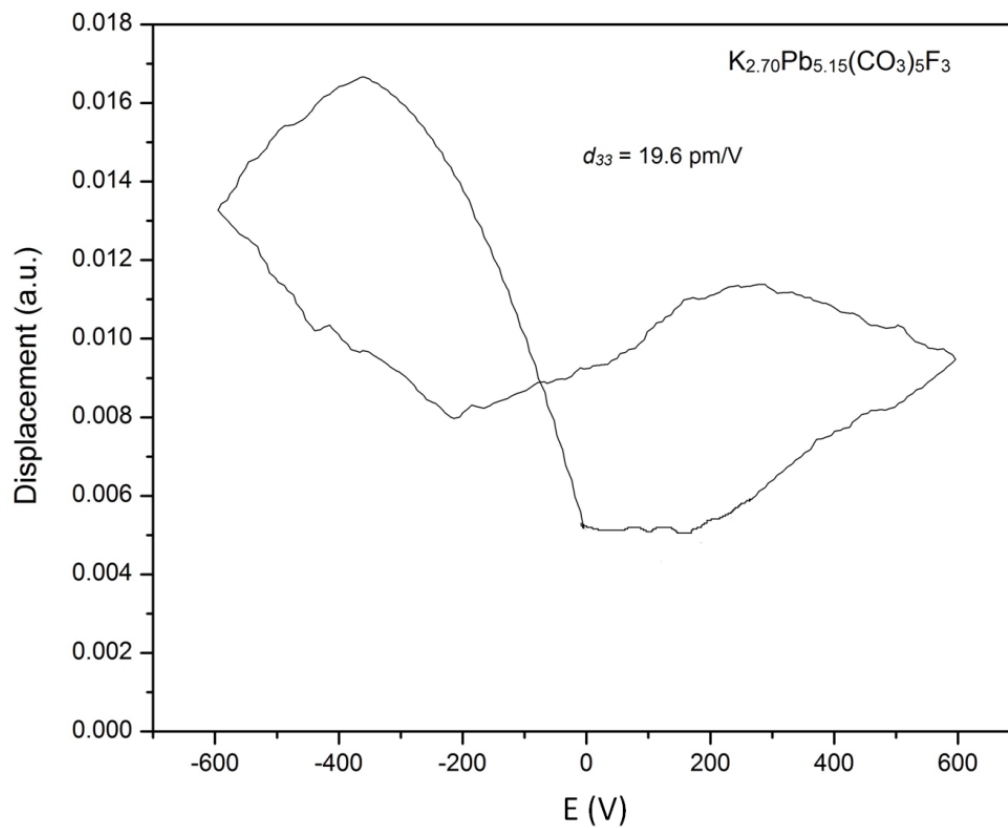


Figure 4.10 Displacement vs. applied voltage for $K_{2.70}Pb_{5.15}(CO_3)_5F_3$

4.5 Conclusions

We have synthesized and characterized two new fluorocarbonates, $\text{KPb}_2(\text{CO}_3)_2\text{F}$ and $\text{K}_{2.70}\text{Pb}_{5.15}(\text{CO}_3)_5\text{F}_3$. Both materials exhibit two-dimensional layered structures. $\text{KPb}_2(\text{CO}_3)_2\text{F}$ consists of double-layers of $\text{Pb}(\text{CO}_3)_3\text{F}$ polyhedra, whereas $\text{K}_{2.70}\text{Pb}_{5.15}(\text{CO}_3)_5\text{F}_3$ consists of double-layers of $\text{Pb}(\text{CO}_3)_3\text{F}$ polyhedra that alternate with triple-layers of $\text{Pb}(\text{CO}_3)_3\text{F}-\text{Pb}(\text{CO}_3)_3\text{F}_2-\text{Pb}(\text{CO}_3)_3\text{F}$ polyhedra. This results in nearly planar sheets of $\text{Pb}(\text{CO}_3)_3\text{F}$ joined together by bridging fluorides. Both of these double and triple-layer structural units are inherently noncentrosymmetric, since they are comprised entirely of elements possessing trigonal symmetry in the *ab*-plane. The stacked double-layer units in $\text{KPb}_2(\text{CO}_3)_2\text{F}$ crystallize with inversion centers between them, resulting in a centrosymmetric space group. The alternating double and triple-layer units in $\text{K}_{2.70}\text{Pb}_{5.15}(\text{CO}_3)_5\text{F}_3$ cannot accommodate inversion centers between them and the space group is therefore noncentrosymmetric. The rigid $\text{Pb}(\text{CO}_3)_3\text{F}$ frameworks form large internal cavities which contain the potassium cations. In $\text{KPb}_2(\text{CO}_3)_2\text{F}$ these cavities are fully occupied. However, in $\text{K}_{2.70}\text{Pb}_{5.15}(\text{CO}_3)_5\text{F}_3$ the cavities in the double-layers are only 70(3)% occupied by K^+ , with the remaining 30(3)% populated half the time with Pb^{2+} and half the time vacant.

The intrinsically asymmetric structures of the double and triple-layers in $\text{KPb}_2(\text{CO}_3)_2\text{F}$ and $\text{K}_{2.70}\text{Pb}_{5.15}(\text{CO}_3)_5\text{F}_3$ make a positive contribution to NCS material engineering. Understanding the crystallographic architecture of these two materials opens up the possibility of controlling the packing and polar directionality of these new

structural building blocks. We intend to investigate this family of compounds further by changing alkaline metals to create other novel NCS materials.

4.6 References

- (1) Nalwa, H. S. *Handbook of Advanced Electronic and Photonic Materials and Devices*; Academic Press: San Diego, 2001.
- (2) Jona, F.; Shirane, G. *Ferroelectric Crystals*; Pergamon Press: Oxford, New York, 1962.
- (3) Auciello, O.; Scott, J. F.; Ramesh, R. *Phys. Today* **1998**, *51*, 22.
- (4) Haertling, G. H. *J. Am. Ceram. Soc.* **1999**, *82*, 797.
- (5) Cady, W. G. *Piezoelectricity; an Introduction to the Theory and Applications of Electromechanical Phenomena in Crystals*; Dover: New York, 1964.
- (6) Jaffe, B.; Cook, W. R.; Jaffe, H. L. C. *Piezoelectric Ceramics*; R.A.N. Publishers: Marietta, Ohio, 1990.
- (7) Munn, R. W. I., C. N. *Principles and Applications of Nonlinear Optical Materials*; CRC Press Inc.: Florida, 1993.
- (8) Rieckhoff, K. E.; Peticolas, W. L. *Science* **1965**, *147*, 610.
- (9) Donakowski, M. D.; Gautier, R.; Yeon, J.; Moore, D. T.; Nino, J. C.; Halasyamani, P. S.; Poepelmeier, K. R. *J. Am. Chem. Soc.* **2012**, *134*, 7679.
- (10) Pinlac, R. A. F.; Stern, C. L.; Poepelmeier, K. R. *Crystals* **2011**, *1*, 3.
- (11) Pinlac, R. A. F.; Marvel, M. R.; Lesage, J. J. M.; Poepelmeier, K. R. *Mater. Res. Soc. Symp. Proc.* **2008**, *1148E*, 01.
- (12) Pan, S.; Smit, J. P.; Marvel, M. R.; Stampler, E. S.; Haag, J. M.; Baek, J.; Halasyamani, P. S.; Poepelmeier, K. R. *J. Solid State Chem.* **2008**, *181*, 2087.

- (13) Marvel, M. R.; Pinlac, R. A. F.; Lesage, J.; Stern, C. L.; Poeppelmeier, K. R. *Z. Anorg. Allg. Chem.* **2009**, *635*, 869.
- (14) Marvel, M. R.; Lesage, J.; Baek, J.; Halasyamani, P. S.; Stern, C. L.; Poeppelmeier, K. R. *J. Am. Chem. Soc.* **2007**, *129*, 13963.
- (15) Halasyamani, P. S.; Poeppelmeier, K. R. *Chem. Mater.* **1998**, *10*, 2753.
- (16) Hu, T.; Hu, C.-L.; Kong, F.; Mao, J.-G.; Mak, T. C. W. *Inorg. Chem.* **2012**, *51*, 8810.
- (17) Mao, J.; Sun, C.; Hu, T.; Yang, B.; Pacificchem 2010. *International Chemical Congress of Pacific Basin Societies*, Honolulu HI, Dec 15 - 20, 2010; American Chemical Society: 2010, p INOR-558.
- (18) Sun, C.-F.; Hu, C.-L.; Xu, X.; Yang, B.-P.; Mao, J.-G. *J. Am. Chem. Soc.* **2011**, *133*, 5561.
- (19) Zhang, J.-H.; Hu, C.-L.; Xu, X.; Kong, F.; Mao, J.-G. *Inorg. Chem.* **2011**, *50*, 1973.
- (20) Sun, C.-F.; Hu, C.-L.; Xu, X.; Ling, J.-B.; Hu, T.; Kong, F.; Long, X.-F.; Mao, J.-G. *J. Am. Chem. Soc.* **2009**, *131*, 9486.
- (21) Fry, A. M.; Seibel, H. A.; Lokuhewa, I. N.; Woodward, P. M. *J. Am. Chem. Soc.* **2012**, *134*, 2621.
- (22) Garcia-Martin, S.; King, G.; Urones-Garrote, E.; Nenert, G.; Woodward, P. M. *Chem. Mater.* **2011**, *23*, 163.
- (23) Muller, E. A.; Cannon, R. J.; Sarjeant, A. N.; Ok, K. M.; Halasyamani, P. S.; Norquist, A. J. *Cryst. Growth Des.* **2005**, *5*, 1913.

- (24) Zhang, G.; Li, Y.; Jiang, K.; Zeng, H.; Liu, T.; Chen, X.; Qin, J.; Lin, Z.; Fu, P.; Wu, Y.; Chen, C. *J. Am. Chem. Soc.* **2012**, *134*, 14818.
- (25) West, J. P.; Sulejmanovic, D.; Hwu, S.-J.; He, J.; VanDerveer, D.; Johnson, B. K. *Inorg. Chem.* **2012**.
- (26) Wu, H.; Pan, S.; Poeppelmeier, K. R.; Li, H.; Jia, D.; Chen, Z.; Fan, X.; Yang, Y.; Rondinelli, J. M.; Luo, H. *J. Am. Chem. Soc.* **2011**, *133*, 7786.
- (27) Zhang, G.; Qin, J.; Liu, T.; Li, Y.; Wu, Y.; Chen, C. *Appl. Phys. Lett.* **2009**, *95*, 261104/1.
- (28) Luo, J.; Pan, S.; Li, H.; Zhou, Z.; Yang, Z. *J. Mater. Sci.* **2011**, *46*, 7443.
- (29) Wang, L.; Pan, S.; Chang, L.; Hu, J.; Yu, H. *Inorg. Chem.* **2012**, *51*, 1852.
- (30) Yu, H.; Pan, S.; Wu, H.; Zhao, W.; Zhang, F.; Li, H.; Yang, Z. *J. Mater. Chem.* **2012**, *22*, 2105.
- (31) Huang, H.; Yao, J.; Lin, Z.; Wang, X.; He, R.; Yao, W.; Zhai, N.; Chen, C. *Chem. Mater.* **2011**, *23*, 5457.
- (32) Ren, P.; Qin, J.; Chen, C. *Inorg. Chem.* **2002**, *42*, 8.
- (33) Zhang, G.; Qin, J.; Liu, T.; Zhu, T.; Fu, P.; Wu, Y.; Chen, C. *Crystal Growth & Design* **2008**, *8*, 2946.
- (34) Chang, H. Y.; Kim, S. W.; Halasyamani, P. S. *Chem. Mater.* **2010**, *22*, 3241.
- (35) Yeon, J.; Kim, S.-H.; Nguyen, S. D.; Lee, H.; Halasyamani, P. S. *Inorg. Chem.* **2012**, *51*, 609.
- (36) Yeon, J.; Kim, S.-H.; Nguyen, S. D.; Lee, H.; Halasyamani, P. S. *Inorg. Chem.* **2012**, *51*, 2662.

- (37) Nguyen, S. D.; Kim, S.-H.; Halasyamani, P. S. *Inorg. Chem.* **2011**, *50*, 5215.
- (38) Chang, H.-Y.; Kim, S.-H.; Ok, K. M.; Halasyamani, P. S. *J. Am. Chem. Soc.* **2009**, *131*, 6865.
- (39) Chang, H. Y.; Sivakumar, T.; Ok, K. M.; Halasyamani, P. S. *Inorg. Chem.* **2008**, *47*, 8511.
- (40) Kim, S.-H.; Yeon, J.; Halasyamani, P. S. *Chem. Mater.* **2009**, *21*, 5335.
- (41) Kim, J.-H.; Halasyamani, P. S. *J. Solid State Chem.* **2008**, *181*, 2108.
- (42) Yeon, J.; Kim, S.-H.; Halasyamani, P. S. *J. Solid State Chem.* **2009**, *182*, 3269.
- (43) Yeon, J.; Kim, S.-H.; Halasyamani, P. S. *Inorg. Chem.* **2010**, *49*, 6986.
- (44) Yeon, J.; Kim, S.-H.; Hayward, M. A.; Halasyamani, P. S. *Inorg. Chem.* **2011**, *50*, 8663.
- (45) Halasyamani, P. S. *Chem. Mater.* **2004**, *16*, 3586.
- (46) Opik, U.; Pryce, M. H. L. *Proc. R. Soc. London, Ser. A* **1957**, *238*, 425.
- (47) Pearson, R. G. *J. Amer. Chem. Soc.* **1969**, *91*, 4947.
- (48) Pearson, R. G. *J. Mol. Struct.: THEOCHEM* **1983**, *12*, 25.
- (49) Wheeler, R. A.; Whangbo, M. H.; Hughbanks, T.; Hoffmann, R.; Burdett, J. K.; Albright, T. A. *J. Am. Chem. Soc.* **1986**, *108*, 2222.
- (50) Goodenough, J. B. *Annu. Rev. Mater. Sci.* **1998**, *28*, 1.
- (51) Zou, G.; Ye, N.; Huang, L.; Lin, X. *J. Am. Chem. Soc.* **2011**, *133*, 20001.
- (52) Grice, J. D.; Maisonneuve, V.; Leblanc, M. *Chem. Rev.* **2007**, *107*, 114.
- (53) Ben, A. A.; Kodjikian, S.; Maisonneuve, V.; Leblanc, M. *Solid State Sci.* **2006**, *8*, 1322.

- (54) Ben, A. A.; Maisonneuve, V.; Kodjikian, S.; Smiri, L. S.; Leblanc, M. *Solid State Sci.* **2002**, *4*, 503.
- (55) Ben, A. A.; Maisonneuve, V.; Leblanc, M. *Solid State Sci.* **2002**, *4*, 1367.
- (56) Ben, A. A.; Maisonneuve, V.; Smiri, L. S.; Leblanc, M. *Solid State Sci.* **2002**, *4*, 891.
- (57) Chen, X. L.; He, M.; Xu, Y. P.; Li, H. Q.; Tu, Q. Y. *Acta Crystallogr., Sect. E: Struct. Rep. Online* **2004**, *E60*, i50.
- (58) Sun, Y. P.; Huang, Q. Z.; Wu, L.; He, M.; Chen, X. L. *J. Alloys Compd.* **2006**, *417*, 13.
- (59) Weil, M. *Acta Crystallogr., Sect. C: Cryst. Struct. Commun.* **2002**, *C58*, i132.
- (60) Jaswal, S. S.; Sharma, T. P. *J. Phys. Chem. Solids* **1973**, *34*, 509.
- (61) Kinase, W.; Tanaka, M.; Nomura, H. *J. Phys. Soc. Jpn.* **1979**, *47*, 1375.
- (62) Mercier, N.; Leblanc, M.; Durand, J. *Eur. J. Solid State Inorg. Chem.* **1997**, *34*, 241.
- (63) Mercier, N.; Leblanc, M. *Eur. J. Solid State Inorg. Chem.* **1994**, *31*, 423.
- (64) Leblanc, M.; Mercier, N.; Atfield, J. P. *Eur. J. Solid State Inorg. Chem.* **1995**, *32*, 535.
- (65) Brown, I. D.; Altermatt, D. *Acta Crystallogr., Sect. B: Struct. Sci.* **1985**, *B41*, 244.
- (66) Brown, I. D. *The Chemical Bond in Inorganic Chemistry*; Oxford University Press: New York, 2002; Vol. 12.
- (67) Grice, J. D.; Van, V. J.; Gault, R. A. *Can. Mineral.* **1994**, *32*, 405.
- (68) Grice, J. D.; Gault, A.; Van, V. J. *Can. Mineral.* **1997**, *35*, 181.

- (69) Grice, J. D.; Chao, G. Y. *Am. Mineral.* **1997**, 82, 1255.
- (70) Fu, P.; Kong, Y.; Gong, G.; Shao, M.; Qian, J. *Kuangwu Xuebao* **1987**, 7, 298.
- (71) Yang, Z.; Pertlik, F. *Neues Jahrb. Mineral., Monatsh.* **1993**, 163.
- (72) Kresse, G.; Hafner, J. *Phys. Rev. B: Condens. Matter* **1993**, 48, 13115.
- (73) Kresse, G.; Furthmüller, J. *Computational Materials Science* **1996**, 6, 15.
- (74) Perdew, J. P.; Burke, K.; Ernzerhof, M. *Phys. Rev. Lett.* **1996**, 77, 3865.
- (75) Kubel, F.; Rief, A. *Zeitschrift für Kristallographie* **2006**, 221, 600.
- (76) Velazquez, M.; Ferrier, A.; Perez, O.; Pechev, S.; Gravereau, P.; Chaminade, J.-P.; Moncorge, R. *Eur. J. Inorg. Chem.* **2006**, 4168.
- (77) Donoghue, M.; Hepburn, P. H.; Ross, S. D. *Spectrochim. Acta. A* **1971**, 27, 1065.
- (78) Andersen, F. A.; Brecevic, L. *Acta Chem. Scand.* **1991**, 45, 1018.
- (79) Refat, M. S.; Elsabawy, K. M. *Bull. Mater. Sci.* **2011**, 34, 873.
- (80) Nakamoto, K.; Wiley online, I. *Infrared and Raman Spectra of Inorganic and Coordination Compounds*; Wiley ; John Wiley Hoboken, N.J. : Chichester, 2007.
- (81) M.Kubelka, P.; Munk, F. Z. *Tech. Phys.* **1931**, 12, 593.
- (82) Tauc, J. *Mater. Res. Bull.* **1970**, 5, 721.

Chapter 5 Three-Dimensional Lead Fluorocarbonates RbPbCO₃F and CsPbCO₃F Exhibiting Large SHG Responses

This chapter is based on the results that has been published in “Tran, T. T.; Rondinelli, J. M.; Halasyamani, P. S., Role of Acentric Displacements on the Crystal Structure and Second-Harmonic Generating Properties of RbPbCO₃F and CsPbCO₃F, *Inorg. Chem.* **2014**, 53, 6241.”

5.1 Abstract

Two lead fluoro-carbonates, RbPbCO₃F and CsPbCO₃F, have been synthesized and characterized. The materials were synthesized through solvothermal and conventional solid-state techniques. RbPbCO₃F and CsPbCO₃F were structurally characterized by single crystal X-ray diffraction and exhibit three-dimensional (3D) crystal structures consisting of corner-shared PbO₆F₂ distorted hexagonal bipyramidal polyhedra. For RbPbCO₃F, infrared, UV-Vis, thermogravimetric and differential thermal analysis measurements were performed. RbPbCO₃F is a new noncentrosymmetric material and crystallizes in the achiral and non-polar space group $P\bar{6}m2$ (crystal class $\bar{6}2m$). Powder second-harmonic generation measurements on RbPbCO₃F and CsPbCO₃F using 1064nm radiation revealed a SHG efficiency of approximately 250 and 300 × α -SiO₂, respectively. Charge constants, d_{33} , of approximately 72 and 94 pm/V were obtained for RbPbCO₃F and CsPbCO₃F, respectively, through converse piezoelectric measurements. Electronic structure calculations indicate that the non-linear optical response originates from the distorted PbO₆F₂ polyhedra, because of the even-odd parity mixing of the O 2p

states with the nearly spherically symmetric $6s$ electrons of Pb^{2+} . The degree of inversion symmetry breaking is quantified using a mode-polarization vector analysis, and is correlated with cation size mismatch from which it is possible to deduce the acentric properties of 3D alkal-metal fluoro-carbonates.

5.2 Introduction

Noncentrosymmetric (NCS) materials, i.e., compounds that do not possess a crystallographic inversion center, are of technological interest owing to their functional ferroelectric, pyroelectric, piezoelectric, non-linear optical (NLO), and multi-ferroic behavior.¹⁻⁹ The design and synthesis of NCS materials remains an ongoing challenge as competing bonding forces often result in centrosymmetric structures. Nonetheless, a number of design strategies towards the creation of new NCS materials have been reported.^{1-3,6,10-35}

We have focused on designing new NCS compounds³⁶⁻⁴³ by using cations susceptible to second-order Jahn–Teller (SOJT) distortion: octahedrally coordinated d^0 transition-metal cations and lone-pair cations.⁴⁴⁻⁴⁷ In order to achieve and enhance acentric polyhedra and inversion symmetry lifting distortions in crystalline materials, anionic substitution was developed.⁴⁸ Because fluorocarbonates constructed from $[(\text{CO}_3)_x\text{F}_y]^{n-}$ polyhedral are known to naturally occur in minerals,⁴⁹ they have garnered considerable attention owing to accessible hydrothermal synthetic methods. Second-harmonic generation (SHG) has been observed in rare earth fluoro-carbonates $\text{Na}_8\text{Lu}_2(\text{CO}_3)_6\text{F}_2$ and $\text{Na}_3\text{Lu}(\text{CO}_3)_2\text{F}_2$ with efficiency of approximately $4 \times \text{KDP}$ ($160 \times \alpha\text{-SiO}_2$).⁵⁰ Also, a

series of alkaline–alkaline-earth fluoro-carbonates, $ABCO_3F$ ($A = K, Rb, Cs$; $B = Ca, Sr, Ba$), was reported to be SHG active.⁵¹ These two families of materials have a wide transparency range between 200 – 800 nm.⁵⁰⁻⁵¹ In addition, several centrosymmetric (CS) fluoro-carbonates have been discovered, including $NaYbCO_3F_2$, $Na_2Yb(CO_3)_2F$, $Na_2EuCO_3F_3$, $Na_3La_2(CO_3)_4F$,⁵²⁻⁵⁸ $BaMCO_3F_2$ (where $M = Mn, Cu$ and Zn)⁵⁶⁻⁵⁷ and $Ba_2Co(CO_3)_2F_2$.⁵⁸

We have reported the synthesis and characterization of two new NCS fluoro-carbonates that incorporate a lone-pair cation - $KPb_2(CO_3)_2F$ and $K_{2.70}Pb_{5.15}(CO_3)_5F_3$.⁵⁹ These materials exhibit inherently asymmetric building blocks, $Pb(CO_3)_3F$ and $Pb(CO_3)_3F_2$, which may be linked to create optically functional new NCS materials. Additional investigation in the alkali-metal – lead – fluoro-carbonate family resulted in the discovery of two NCS materials - $RbPbCO_3F$ and $CsPbCO_3F$. $CsPbCO_3F$ was recently reported,⁶⁰ and it was suggested that the p - π interaction between Pb^{2+} and CO_3^{2-} is responsible for the large SHG response of $13.4 \times KDP$ ($530 \times \alpha$ - SiO_2). Remarkably, it was reported that Pb^{2+} is stereochemically *inactive*, and model electronic structure calculations on molecular $PbCO_3$ units identified enhanced *covalent* interactions at the origin of the SHG response upon inspection of the real space extent of the molecular orbitals characterizing the highest occupied and lowest unoccupied states.

In this chapter, we report the synthesis, crystal structure, characterization and atomic scale–acentric property relationships of $RbPbCO_3F$ and $CsPbCO_3F$. The second harmonic response and piezoelectric coefficients are determined and correlated to the locally polar PbO_6F_2 units with the oxygen ligands associated with the cooperatively aligned triangular

carbonate units. We disentangle the contribution of the acentric displacements in the achiral and non-polar structures from the proposed electronic polarizability mechanisms using a scheme introduced by Cammarata *et al.*⁶¹ In this regard, recent applications of group representation theory and mode crystallography inspired by Chen's anionic group theory are applied in combination with density functional calculations that treat on equal footing the point and translation periodicity of the system to address the microscopic origin for the NLO behavior. We find that the local Pb coordination environment is acentric and the ionic-covalent balance among bridging ligands is highly anisotropic, suggesting that analysis of charge density contours may be insufficient to deduce Pb²⁺ lone pair in-activity. Rather, the application of a mode-polarization analysis provides an improved structural descriptor of the SHG response, which opens a path to understand the acentric properties of the known three-dimensional fluorocarbonates.

5.3 Results and Discussion

5.3.1 Structures

Details of the synthesis and characterizations are presented in Chapter 3. The semi-quantitative energy-dispersive X-ray spectroscopy (EDS) measurements were taken three times from the selected RbPbCO₃F and CsPbCO₃F crystals that were used for X-ray diffraction analysis. The average Rb:Pb and Cs:Pb ratios of 1.06(9) and 1.09(3), respectively, found by EDS is in agreement with the value of 1.00 determined by least squares refinement of the X-ray data. Relevant crystallographic data, selected bond

distances and angles, atomic coordinates and equivalent isotropic displacement parameters for RbPbCO₃F and CsPbCO₃F are given in Tables 5.1 – 5.4.

RbPbCO₃F exhibits a three-dimensional crystal structure consisting of corner-sharing Pb(CO₃)₃F₂ polyhedra (see Figure 5.1). The Pb²⁺ cations are connected to carbonate groups in the *ab*-plane, and along the *c*-axial direction the connectivity is through bridging fluorides. The Rb⁺ cations are located in the cavities formed between Pb(CO₃)₃F₂ polyhedral building units. In this structure model, the bridging fluorine is observed to be statistically disordered in the *ab*-plane, resulting in a Pb–F–Pb angle of 170.8(9)°. In connectivity terms, the material may be written as [Pb(CO₃)₃/3F₂/2]¹⁻, with charge balance maintained by one Rb⁺ cation. Each Pb²⁺ cation is bonded to six oxygen atoms and two fluorine atoms in a distorted hexagonal bipyramidal coordination environment, with Pb–O distances of 2.6864(8) Å and Pb–F distances of 2.421(7) Å. The carbonate C–O distance is 1.290(6) Å. The Rb⁺ cation is surrounded by six oxygen atoms and three fluorine atoms with Rb–O distances of 3.010(3) Å and Rb–F distances of 3.00(4) Å. Bond valence calculations resulted in values of 1.11, 1.97, and 3.93 for Rb⁺, Pb²⁺, and C⁴⁺, respectively (Table 5.5).⁶²⁻⁶³ The anisotropic displacement parameters of RbPbCO₃F are depicted in Figure 5.2 as ellipsoid diagrams.

Table 5.1 Crystallographic data for RbPbCO₃F and CsPbCO₃F

	RbPbCO ₃ F	CsPbCO ₃ F
M/gmol ⁻¹	371.67	419.11
T/K	213(2)	213(2)
$\lambda/\text{\AA}$	0.71073	0.71073
Crystal system	Hexagonal	Hexagonal
Space group	$P\bar{6}m2$ (No. 187)	$P\bar{6}m2$ (No. 187)
$a/\text{\AA}$	5.3488(12)	5.393(3)
$c/\text{\AA}$	4.8269(12)	5.116(2)
$V/\text{\AA}^3$	119.59(5)	128.85(10)
Z	1	1
d_c/gcm^{-3}	5.161	5.401
μ/mm^{-1}	45.287	39.611
$2\theta_{\text{max}}/^\circ$	54.84	56.34
R_{int}	0.0201	0.0328
GOF	1.267	1.230
$R(F)^a$	0.0112	0.0191
$R_w(F_o^2)^b$	0.0258	0.0517
Flack parameter	0.09(3)	0.32(2)
Largest diff. peak/hole ($e \text{\AA}^{-3}$)	0.673/-0.853	0.966/-0.680
^a $R(F) = \Sigma F_o - F_c /\Sigma F_o $. ^b $R_w(F_o^2) = [\Sigma w(F_o^2 - F_c^2)^2/\Sigma w(F_o^2)^2]^{1/2}$		

Table 5.2 Selected bond distances (Å) and angles (deg) for RbPbCO₃F and CsPbCO₃F

RbPbCO ₃ F		CsPbCO ₃ F	
Pb – O × 6	2.6865(8)	Pb – O × 6	2.7086(17)
Pb – F × 2	2.421(7)	Pb– F	2.23(3)
		Pb– F	2.88(3)
C – O × 3	1.290(6)	C – O × 3	1.300(11)
O – Pb – O	49.1(2)	O – Pb – O	49.1(5)
O – Pb – O	70.9(2)	O – Pb – O	70.9(5)
F – Pb – O	85.8(18)	F – Pb – O	90.0
F – Pb – O	93.8(16)		
Pb – F – Pb	175.4(19)	Pb – F – Pb	180.0

Table 5.3 Atomic coordinates and equivalent isotropic displacement parameters (Å²) for RbPbCO₃F

Atom	x	y	z	U_{eq}^a
Rb	0.6667	0.3333	0.0000	0.011(3)
Pb	1.0000	1.0000	0.5000	0.007(2)
C	0.3333	0.6667	0.5000	0.011(3)
O	0.4726(6)	0.9451(12)	0.5000	0.020(2)
F	0.9580(17)	0.9790(9)	0.0000	0.020(14)

Table 5.4 Atomic coordinates and equivalent isotropic displacement parameters (Å²) for CsPbCO₃F

Atom	x	y	z	U_{eq}^a
Cs	0.3333	0.6667	0.5000	0.014(4)
Pb	0.0000	0.0000	0.0000	0.010(4)
C	0.6667	0.3333	0.0000	0.006(5)
O	0.5275(12)	0.4725(12)	0.0000	0.020(3)
F	0.0000	0.0000	0.4360(4)	0.023(6)

^a U_{eq} is defined as one-third of the trace of the orthogonalized U_{ij} tensor

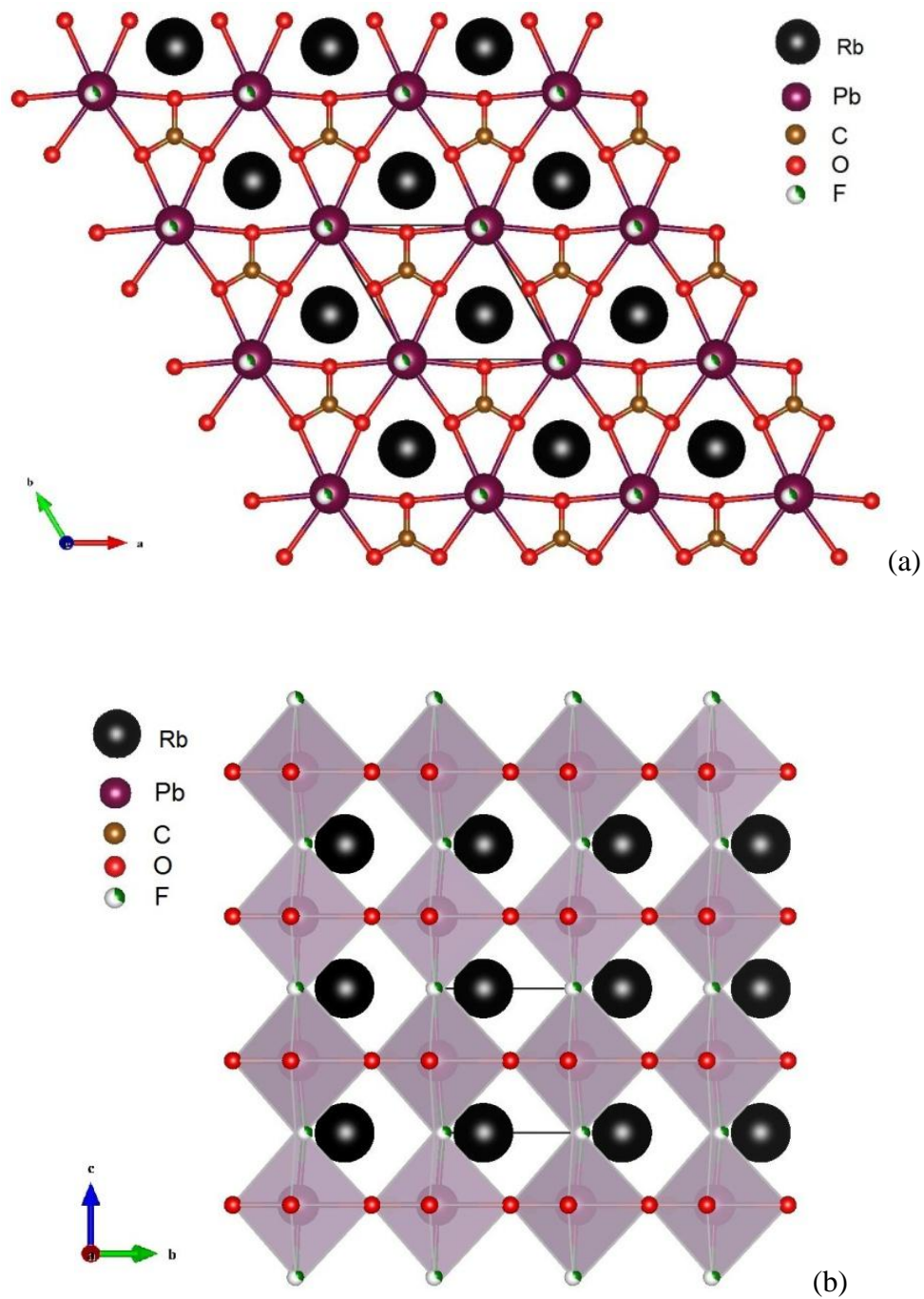


Figure 5.1 Ball-and-stick in the ab -plane (a), and polyhedral in the bc -plane (b) representations of RbPbCO_3F . Only one position of the disordered bridging fluoride in the structure is shown.

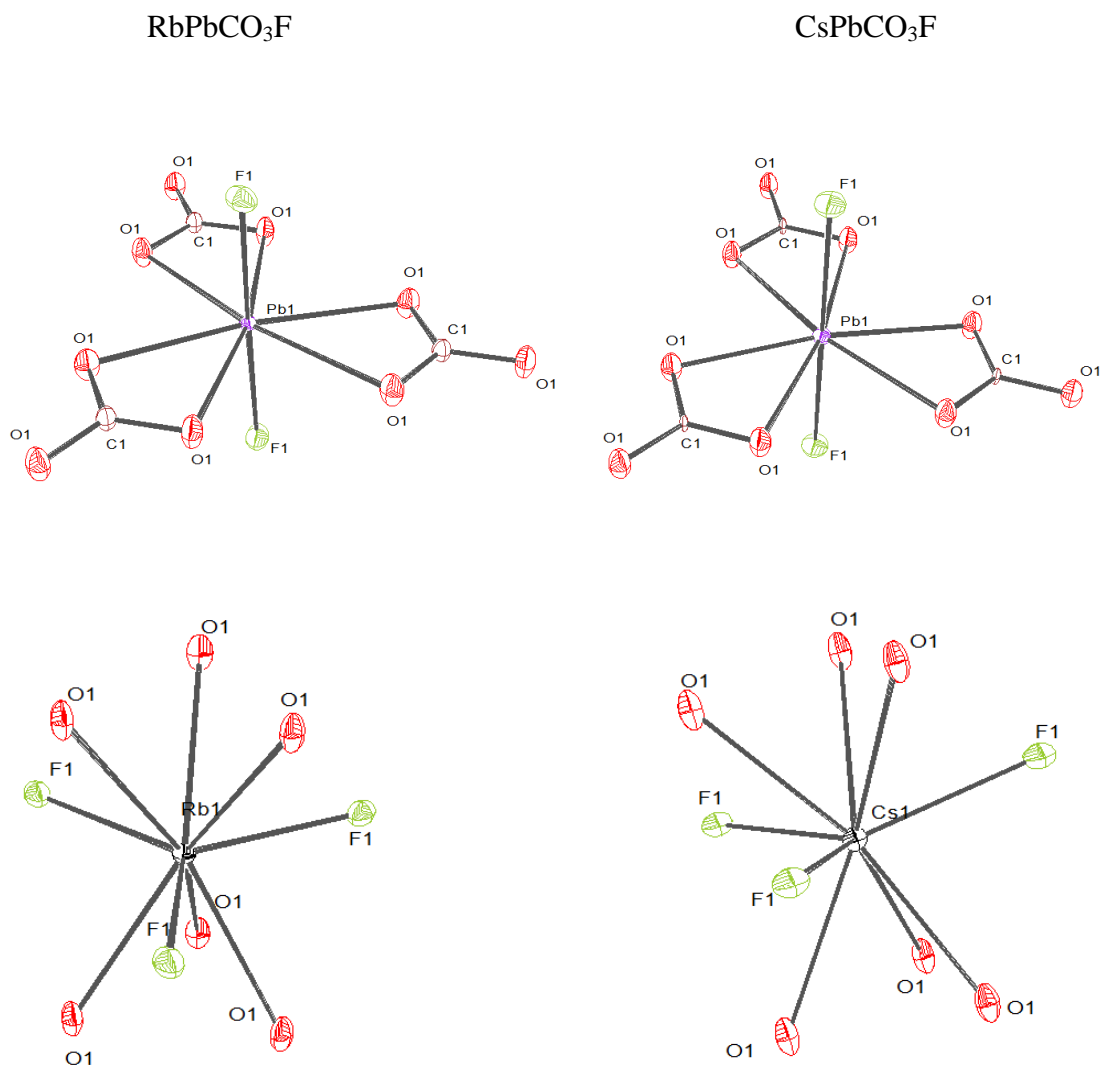


Figure 5.2 ORTEP (50% probability ellipsoids) diagrams of RbPbCO_3F and CsPbCO_3F . Note that the F atoms, which were refined to be disordered, have well-behaved thermal parameters.

For CsPbCO₃F compound, we noted discrepancies between our structure and the recently reported one during our data collection and refinement of CsPbCO₃F. In the reported structure, the bridging fluoride is entirely ordered in a $\bar{6}m2$ crystallographic site, resulting in a symmetric bridge having identical Pb-F distances of 2.5536(7) Å.⁶⁰ Also, the equivalent isotropic displacement U_{eq} for F is significantly greater than those for other atoms.⁶⁰ In addition, the bond valence sum value of Pb²⁺ was reported to be 1.686, which can be considered to be fairly under-bonded.⁶⁰ Our data clearly reveal that the bridging F atom is statistically disordered along the *c*-axis direction. The thermal displacement parameters of our structure refinement are represented in Figure 5.2.

Similar to RbPbCO₃F, CsPbCO₃F also exhibits a three-dimensional structure consisting of corner-sharing Pb(CO₃)₃F₂ polyhedra (see Figure 5.3). The Pb²⁺ cations are connected by carbonate groups in the *ab*-plane, and along the *c*-axis direction the connectivity is through a bridging fluoride. The Cs⁺ cations are located in cavities formed between Pb(CO₃)₃F₂ polyhedral building units. The statistic disorder of the bridging fluoride along the *c*-axis direction results in a shorter and a longer Pb-F distance. The Pb²⁺ cation is observed in a distorted hexagonal bipyramidal environment with Pb-O distances of 2.709(2) Å and Pb-F distances of 2.23(3) and 2.88(3) Å. In connectivity terms, the material may be written as [Pb(CO₃)_{3/3}F_{2/2}]¹⁻, with charge balance maintained by one Cs⁺ cation. The Cs⁺ cation is surrounded by six oxygen atoms and three fluorine atoms with Cs-O distances of 3.136(7) Å and Cs-F distances of 3.131(3) Å. Bond valence calculations resulted in values of 1.20, 1.89, and 3.84 for Cs⁺, Pb²⁺, and C⁴⁺, respectively (Table 5.5).⁶²⁻⁶³

As discussed earlier, in RbPbCO₃F structure, the statistical disorder of the bridging F atom in the *ab*-plane results in a Pb–F–Pb angle of 170.8(9)°. This specifically disordered fluorine was also observed in K_{2.70}Pb_{5.15}(CO₃)₅F₃ with a corresponding Pb–F–Pb angle of 169.5(16)°. ⁵⁹ It should be noted that in these materials, the Pb–F–Pb is symmetrically bridged with two identical Pb–F distances and the disordered F renders a Pb–F–Pb angle offset by about 10° from 180°.

With respect to the CsPbCO₃F structure, the F atom was initially also refined on a $\bar{6}m2$ site (0,0,1/2) midway between Pb atoms, which created a symmetrically bridged linear chain along the *c*-axis. However, it was noted that U_{33} , the component of the anisotropic displacement along the *c* direction, was very large, which was also observed in the previously reported CsPbCO₃F structure. ⁶⁰ The large U_{33} clearly indicated that the F atom was not actually on the $\bar{6}m2$ site, but instead was displaced by a significant distance, 0.32 Å, from this crystallographic site in a disordered arrangement. The *z*-coordinate parameter was allowed to refine independently rendering a converged value of 0.4360(4), and the anisotropic displacement parameters of the F atom is well-behaved (see Figure 5.2). Attributable to the disorder, shorter (2.23(3) Å) and longer (2.88(3) Å) Pb–F bonds are observed. These Pb–F bond lengths are consistent with those reported in literature. ⁶⁴⁻⁶⁵ As would be expected, the Pb–F distances in our structural model are different from the previous report ⁶⁰ where two Pb–F distances 2.5536(7) Å. This distance is simply an average of the two true Pb–F distances and not an actual accurate bond distance. Also, in our model there is an improvement in bond valence sum for Pb²⁺ in our structure compared to the reported value, 1.89 vs 1.686. ⁶⁰

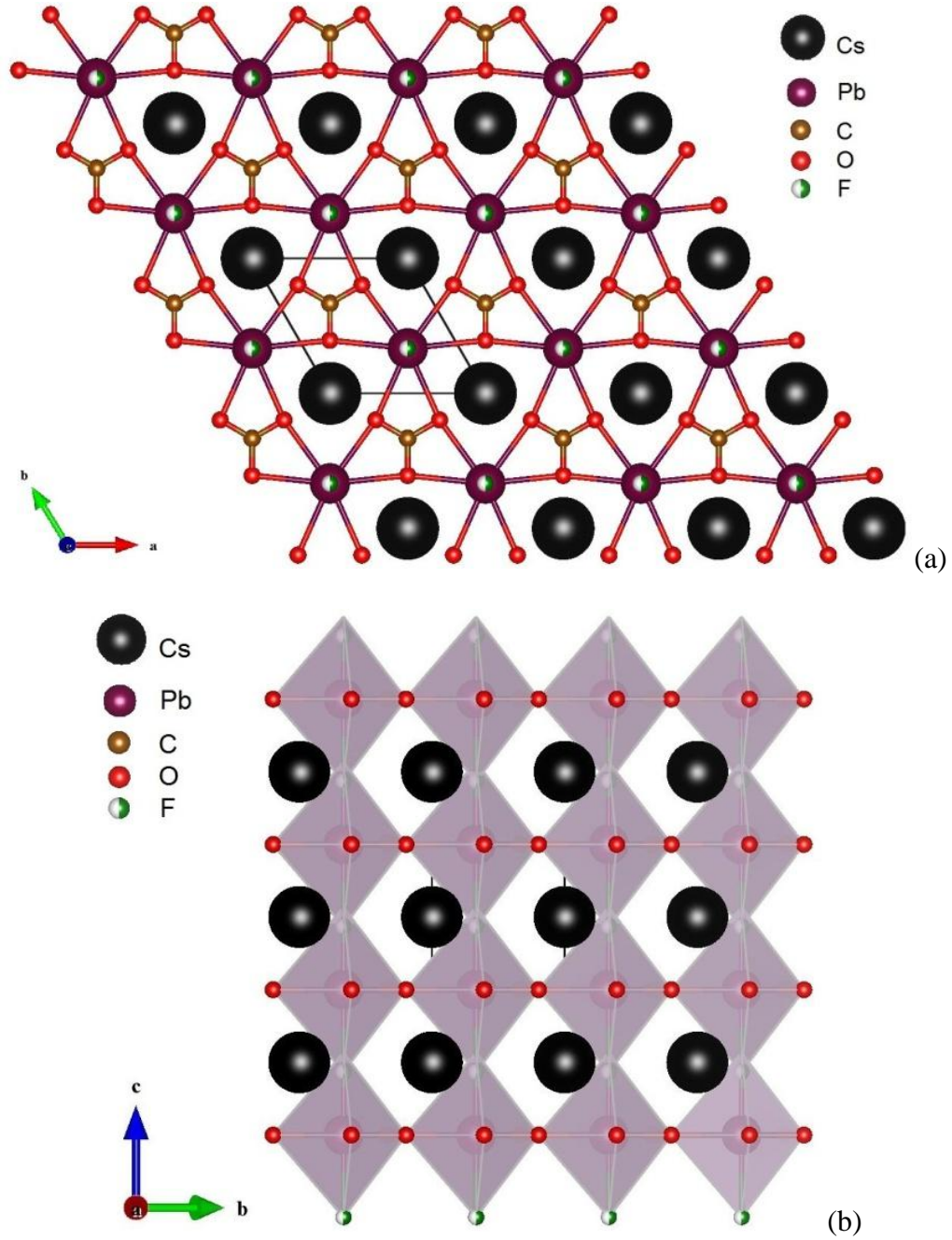


Figure 5.3 Ball-and-stick in the *ab*-plane (a) and polyhedral in the *bc*-plane (b) representations of CsPbCO₃F. Only one position of the disordered bridging fluoride in the structure is shown.

Further examination of the two related materials, RbPbCO₃F and CsPbCO₃F, reveals some similarities and differences in the crystallographic architecture. These materials both crystallize in the hexagonal $P\bar{6}m2$ space group with the a and b unit cell parameters nearly identical (5.3488(12) vs 5.393(3) Å for the Rb and Cs compounds respectively) since the parameters are defined by the Pb(CO₃)₃ bonding patterns. The c -axes, however, are different (4.8269(12) (Rb) vs 5.116(2) Å (Cs)), and these are a function of the Pb–F distances associated with the size of the alkaline cation (see Figures 5.1 and 5.3). RbPbCO₃F and CsPbCO₃F are structurally similar and built up from the Pb(CO₃)₃F₂ building units. With respect to the 'A⁺' cations, the effective ionic radii are 1.63 and 1.78 Å for Rb⁺ and Cs⁺, respectively.⁶⁶ If we replace Rb⁺ with the larger cation Cs⁺ in the structure, we notice that the cavity separation is not very big. In other words, when the larger cation Cs⁺ is introduced into the crystal structure, the structural strain is produced inside the cavities between the Pb(CO₃)₃F₂ frameworks. To minimize this strain, the Pb(CO₃)₃ layers need to slightly separate along the c direction to accommodate the larger cation Cs⁺. This phenomenon is clearly observed in the increase of the c -axis of unit cell parameters (see Table 5.1). The c -axis of CsPbCO₃F is longer than that of RbPbCO₃F, whereas the a - and b -axes remain essentially constant.

For fluoro-carbonate materials, the spatial arrangement of the acentric carbonate groups with respect to the overall structure has been previously described.⁶⁷⁻⁶⁹ It has been observed that in fluoro-carbonates, the CO₃ group may be parallel or inclined with regard to the rest of the structure. The carbonate groups in RbPbCO₃F and CsPbCO₃F are parallel to the entire structures, which is similar to other three-dimensional fluoro-

carbonates such as KSrCO_3F , RbSrCO_3F , KCaCO_3F .⁵¹ Along the *c*-axis, the eclipsed and staggered arrangements of the carbonate groups were observed in our $\text{KPb}_2(\text{CO}_3)_2\text{F}$ and $\text{K}_{2.70}\text{Pb}_{5.15}(\text{CO}_3)_5\text{F}_3$,⁵⁹ whereas the acentric CO_3 groups in Rb and Cs members of this family are found to align in co-planar and co-parallel fashion with respect to the overall structural architecture, which should produce a structural contribution to the observed SHG efficient.

Table 5.5 Bond valence analysis for $\text{RbPbCO}_3\text{F}^a$

Atom	O	F	Σ cations
Rb	0.133 ^[x6]	0.103 ^[x3]	1.11
Pb	0.212 ^[x6]	0.348 ^[x2]	1.97
C	1.31 ^[x3]		3.93
Σanions	2.00	1.01	

^a Bond valence sums calculated with the formula: $S_i = \exp[(R_0 - R_i)/B]$, where S_i =valence of bond “*i*” and $B=0.37$.

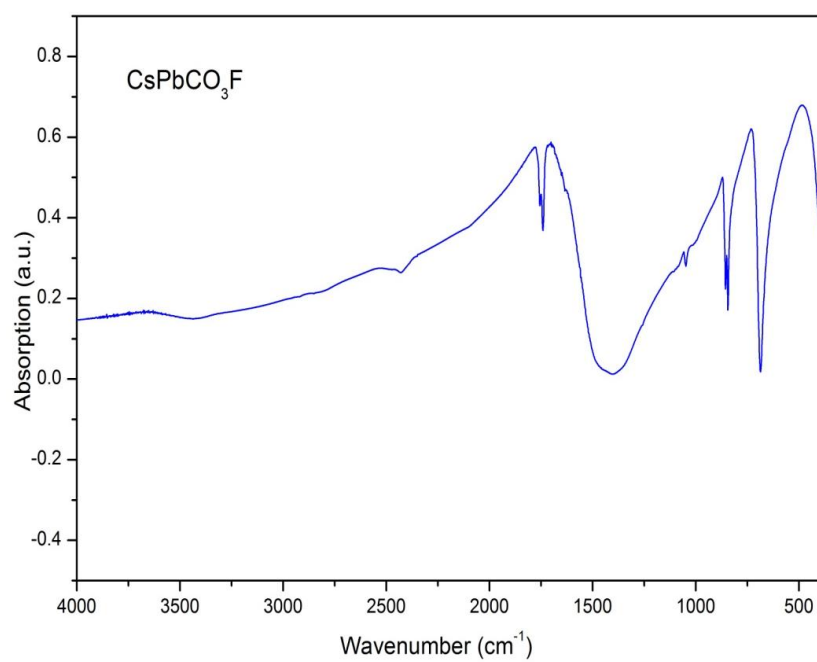
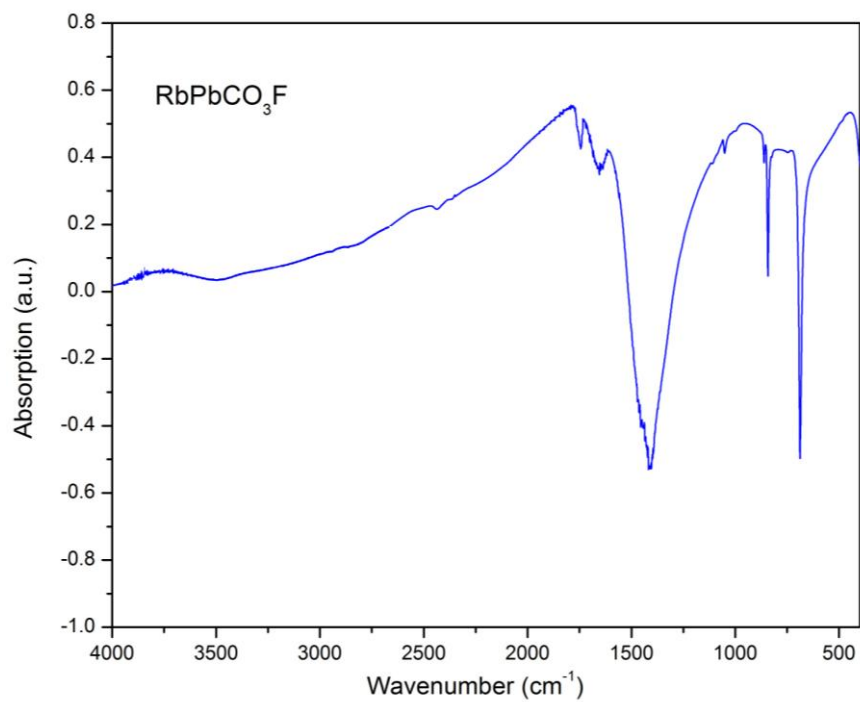
Table 5.5 Bond valence analysis for $\text{CsPbCO}_3\text{F}^a$

Atom	O	F	Σ cations
Cs	0.143 ^[x6]	0.115 ^[x3]	1.20
Pb	0.199 ^[x6]	0.582	1.89
		0.101	
C	1.28 ^[x3]		3.84
Σanions	1.96	1.03	

^a Bond valence sums calculated with the formula: $S_i = \exp[(R_0 - R_i)/B]$, where S_i =valence of bond “*i*” and $B=0.37$.

5.3.2 Infrared (IR) Spectroscopy

The IR spectrum of RbPbCO₃F and CsPbCO₃F revealed C–O vibrations between 1400 – 680 cm⁻¹. The strong broad bands observed at 1410 and 1442 cm⁻¹ can be assigned to the stretching C–O vibrations. The out-of-plane vibration, $\delta(\text{OCO})$, is observed in the range of 840 – 830 cm⁻¹ as a medium band, and the bending vibration, $\delta(\text{OCO})$, should appear at 700 – 670 cm⁻¹ as a medium weak band.⁷⁰⁻⁷³ A strong band, however, was observed in the range of 700 – 670 cm⁻¹ which can be attributed to the overlap between the bending vibration, $\delta(\text{OCO})$, and the stretching vibration, $\nu(\text{Pb–O})$.⁷²⁻
⁷³ The $\nu(\text{Pb–F})$ vibration is observed at ~400 cm⁻¹.⁷³ The infrared spectra are presented in Figure 5.4.



	$\nu(\text{C-O})$	$\delta(\text{OCO})$	$\nu(\text{Pb-F})$
RbPbCO ₃ F	1410, 1038	836, 687	400
CsPbCO ₃ F	1442, 1049	841, 682	404

Figure 5.4 IR spectra of RbPbCO₃F and CsPbCO₃F

5.3.3 UV-Vis Diffuse Reflectance Spectroscopy

The UV-Vis diffuse reflectance spectra revealed that the absorption energies for RbPbCO₃F and CsPbCO₃F are approximately 4.1 and 4.3 eV, respectively. This is consistent with the white color of the materials. Absorption (K/S) data were calculated from the Kubelka-Munk function.⁷⁴⁻⁷⁵

$$F(R) = \frac{(1-R)^2}{2R} = \frac{K}{S}$$

where R represents the reflectance, K the absorption coefficient, and S the scattering factor. In a K/S versus E (eV) plot, extrapolating the linear part of the rising curve to zero resulted in the onset of absorption at 4.1 and 4.3 eV. The UV-Vis diffuse reflectance spectra are presented in Figure 5.5.

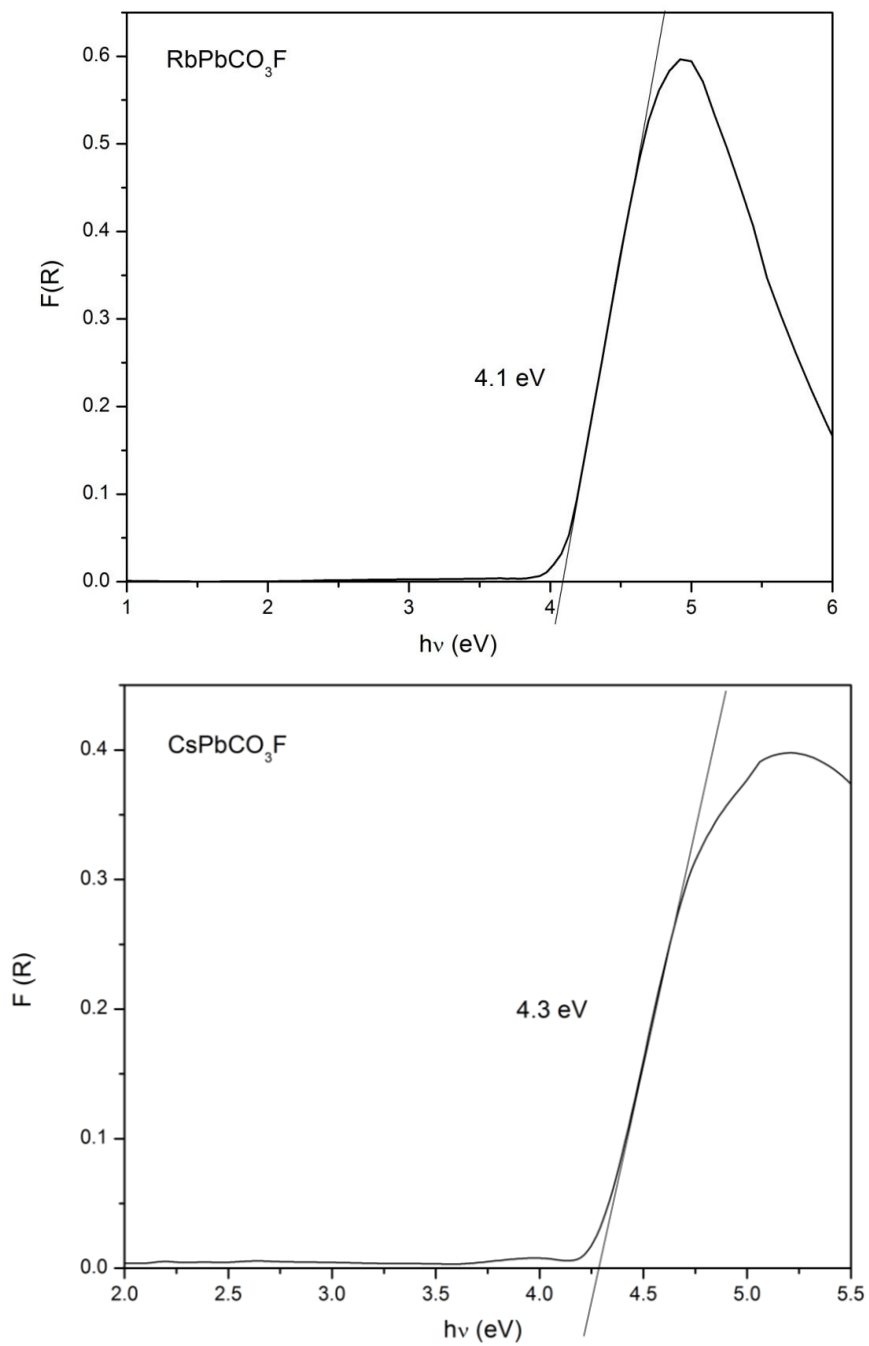


Figure 5.5 UV-Vis diffuse reflectance spectra of RbPbCO_3F and CsPbCO_3F

5.3.4 Thermal Analysis

The thermal behaviors of RbPbCO_3F and CsPbCO_3F were investigated using thermogravimetric analysis (TGA) and differential thermal analysis (DTA) under N_2 atmosphere. The decomposition of materials begins at approximately 300°C , corresponding to the loss of CO_2 . The experimental weight loss is in good agreement with the calculated weight loss. The endothermic peaks in the heating curve are consistent with the decomposition of the material. At approximately 750°C , the drop in mass was observed in the TGA plot that is likely attributable to the loss of fluorides. The exothermic peaks in the cooling cycle indicate re-crystallization of the residues of RbPbCO_3F and CsPbCO_3F occurred at approximately 860 and 760°C . That is confirmed by the appearance of two different modifications of lead (II) oxide, i.e., PbO ($P4/nmm$) and PbO ($Pbcm$), in powder XRD pattern of the residuals. The thermal behaviors of the decomposition products are consistent with those reported previously.⁷⁶ The DTA/TGA diagrams for RbPbCO_3F and CsPbCO_3F are depicted in Figures 5.6.

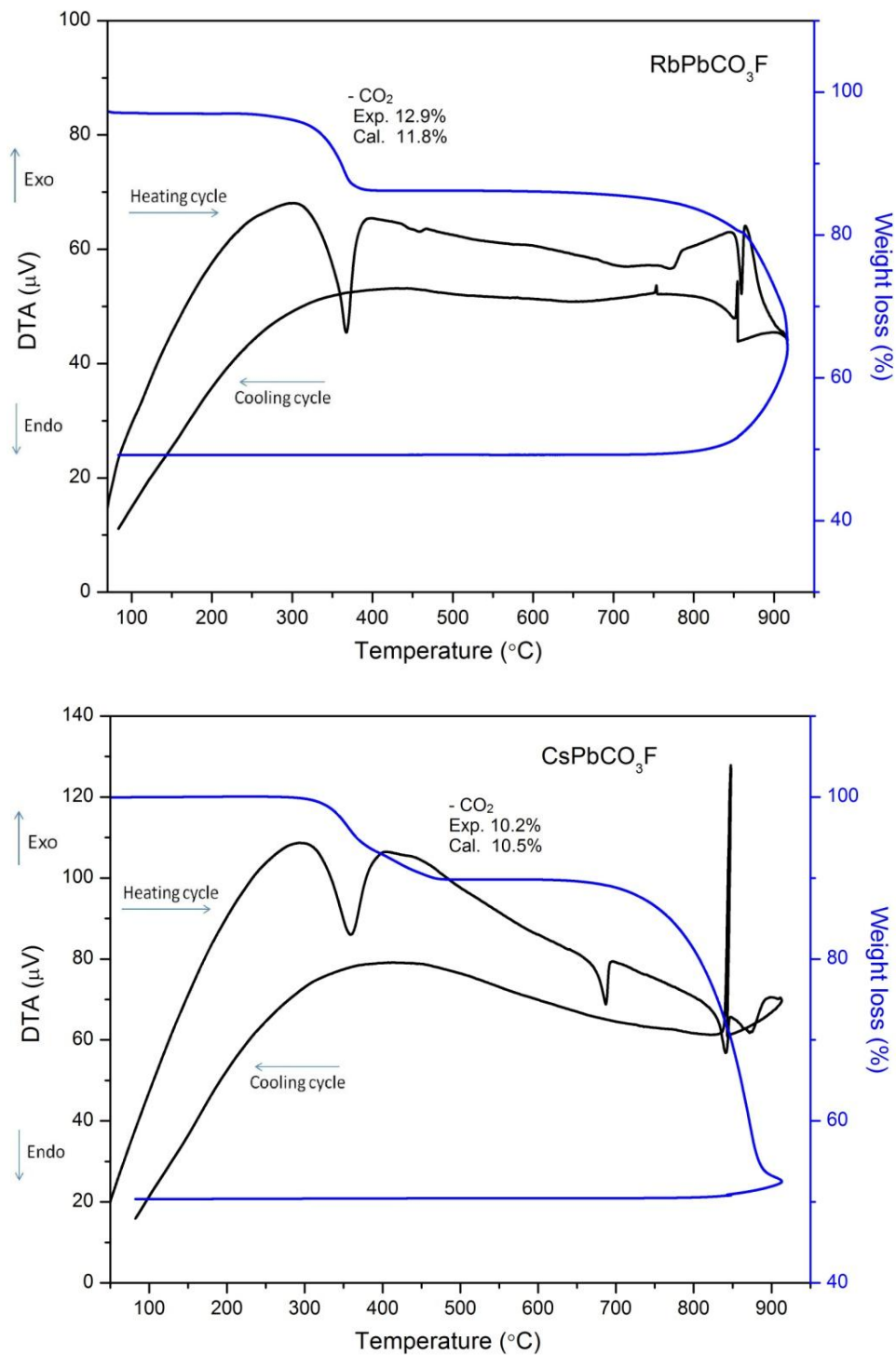


Figure 5.6 Thermogravimetric analysis and differential thermal analysis diagram of RbPbCO_3F and CsPbCO_3F under N_2

5.3.5 Second-Harmonic Generation (SHG) and Piezoelectric Measurements

Since RbPbCO_3F and CsPbCO_3F crystallize in the NCS space group $P\bar{6}m2$, we investigated the SHG and piezoelectric properties. Powder SHG measurements using 1064nm radiation revealed a SHG efficiency of approximately 250 and $300 \times \alpha\text{-SiO}_2$, respectively, in the 45–63 μm particle size range. Additional SHG measurements, particle size vs. SHG efficiency, indicate both materials exhibit type 1 phase-matching behavior. As such RbPbCO_3F and CsPbCO_3F fall into the class A category of SHG materials, as defined by Kurtz and Perry (see Figure 5.7).⁷⁷

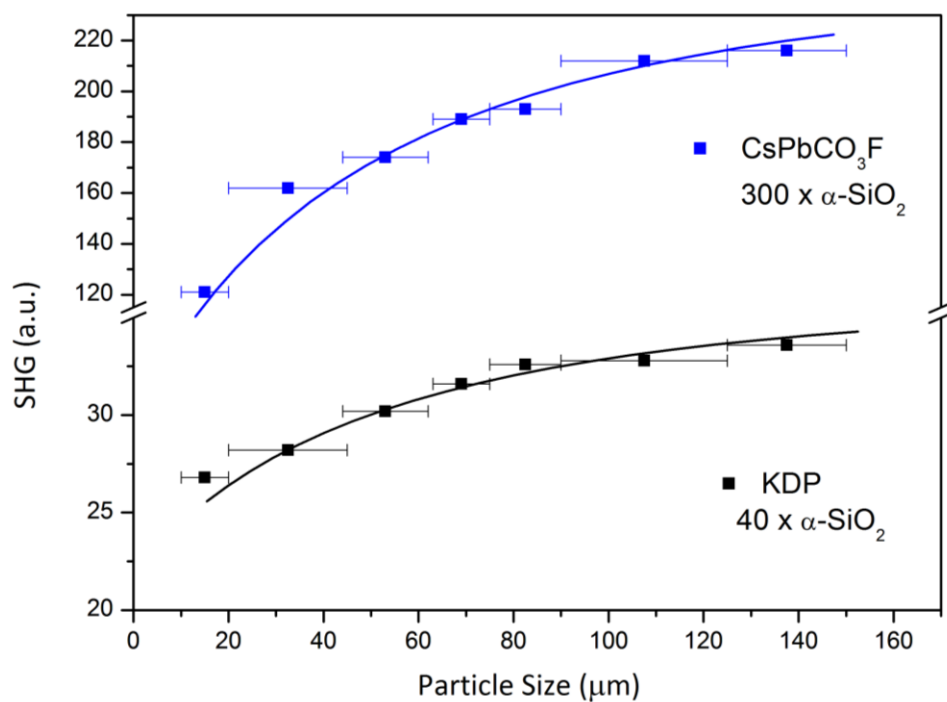
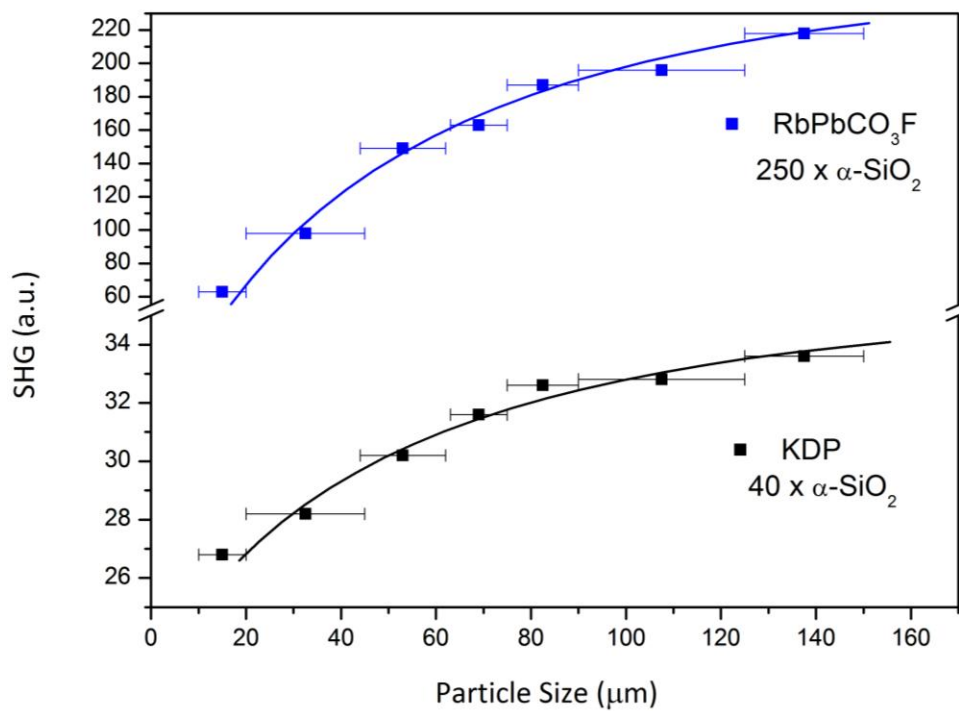


Figure 5.7 Powder second-harmonic generation for RbPbCO₃F and CsPbCO₃F. Curves are drawn to guide the eye and are not a fit to the data.

Converse piezoelectric measurements on RbPbCO_3F and CsPbCO_3F were also performed and a piezoelectric charge constant, d_{33} , of approximately 72 pm/V and 94 pm/V, respectively, were determined (see Figure 5.8).

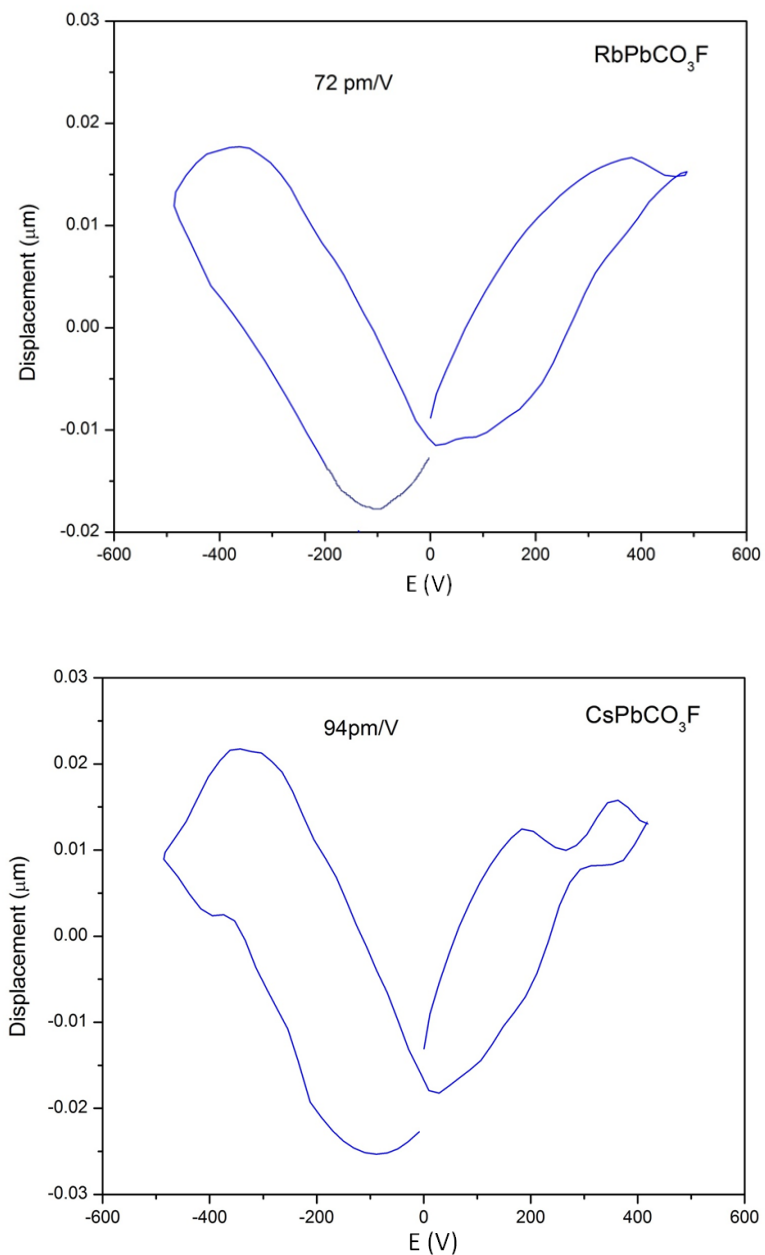


Figure 5.8 Displacement vs. applied voltage for RbPbCO_3F and CsPbCO_3F

5.3.6 Electronic Structure

Figure 5.9 shows the atom-resolved densities of states (DOS) for RbPbCO₃F (upper panel) and CsPbCO₃F (lower panel). First, we obtain a band gap of 3.18 eV and 3.31 eV for RbPbCO₃F and CsPbCO₃F, respectively, (at the DFT-PBEsol level), consistent with the concept that Cs expands the lattice and makes the compound more ionic. The electronic excitation involved in SHG is between states across these gaps. Here we find that the onset of the valence band (VB) edge is sharper in CsPbCO₃F and the bandwidth is much narrower (by 1 eV) compared to the RbPbCO₃F, which is consistent with the observed larger SHG response in the Cs compound over the Rb phase.

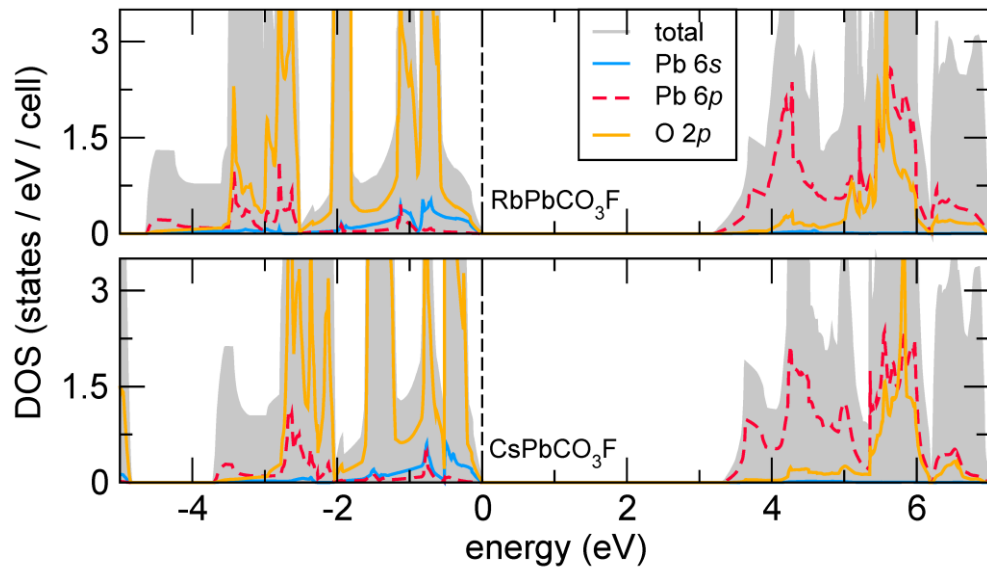


Figure 5.9 The electronic densities of states (DOS) for RbPbCO₃F and CsPbCO₃F decomposed by atomic site and orbital contributions

In both structures the frontier orbitals in the VB are largely derived from the O 2*p* states of the [CO₃]²⁻ group mixed with the nearly spherically symmetric 6*s* electrons of the Pb²⁺ cation; the low-lying states in the conduction band are mainly composed of the

Pb $6p$ states. This electronic configuration is ideal for the electric field of an incident photon to produce an acentric and polarized charge distribution, because of the even-odd parity mixing of the states in the LUMO and HOMO. The filled Rb and Cs states are deep in the valence band (data not shown), centered at -9 eV (Rb) and ranging from -7 to -5 eV (Cs); therefore they should not largely influence the optical transition. The role of these large metal cations is to provide the crystalline lattice topology for the packing of the SHG-active PbCO_3 groups, which we explore in more detail from a structure perspective below.

5.4 Relationship between Electronic Structure, NCS Structures and Acentric Crystal Properties

First, we examine in more detail the electronic structure and charge density distribution by computing the electron localization function (ELF) for both RbPbCO_3F and CsPbCO_3F . Consistent with Ref. 59, we find that there is an asymmetric electron density arranged about the oxygen atoms forming the carbonate group, which is repeated in a clover-like pattern. Interestingly, the electronic density about the Pb^{2+} sites is nearly symmetric and resemble a Reuleaux (rounded equilateral) triangle⁷⁸ when viewed in projection (Figure 5.10a). The Pb cation is located at the center of the triangle which is formed by the space shared by three equivalent circles, each of which have a center tangent to the other and simultaneously collinear with the nearest neighbor carbon atoms. As a result, the charge density on any side of the Pb cation remains equidistance to the opposite “vertex” of maximum density (arrowed) and thus may become highly

polarizable along the Reuleaux triangle vertices, i.e., in the $[\bar{1}10]$, $[210]$, and $[\bar{1}\bar{2}0]$ directions upon excitation by the electric field of an incident photon.

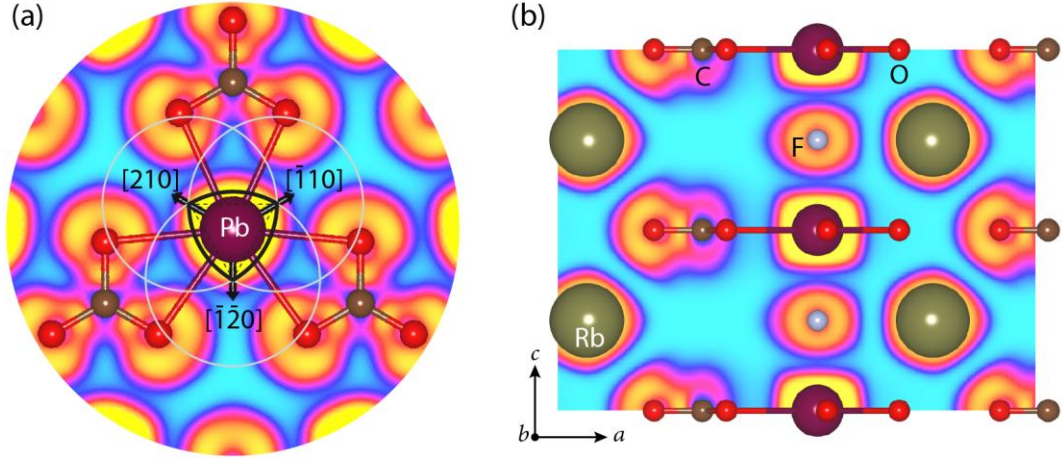


Figure 5.10 Reuleaux triangle projection overlaid on charge density contours of the ELF (ELF=0.85) in the (001) plane about the Pb site in RbPbCO₃F. ELF plot in the $(\bar{1}20)$ plane corresponding to a planar slice along the $[210]$ direction intersecting the “vertex” of the Reuleaux triangle. The red, silver, brown, maroon spheres correspond to oxygen, fluorine, carbon, and lead atoms, respectively.

Indeed, projection of the ELF plot along the normal to these directions reveals that charge density about the Pb²⁺ site is unevenly distributed in the plane (Figure 5.10b). The bloated electron density extends further along the positive a direction than along the negative a direction in the $(\bar{1}20)$ plane. This is evident by comparing the high electron density regions about the Pb site with the Pb-O bond due to neighboring carbonate units. Interestingly, the electron localization about the fluorine anions is also highly anisotropic (Figure 5.10b), which manifest in our Born effective charges (Z^*) for fluorine (Table 5.6). We find dynamical charges of $Z_{11}^* = -0.7$ and $Z_{33}^* = -3.3$, whereas the nominal ionic value is -1 . The anomalous value for Z_{33}^* is indicative an electric polarization to develop

along the six fold axis since Z^* is the linear coefficient coupling an electric field and the force applied on the ion by the field. Similar anomalous values are found for Pb^{2+} (Table 5.6), albeit in the basal plane owing to the strong dynamic charge transfer along the Pb-O bond linked with the carbonate groups consistent with ionic-covalent character of the fluoro-carbonates. Thus while in the ground state these fluoro-carbonates may not present an obvious lobe of electron density corresponding to well-defined static lone-pair, the charge density about the Pb^{2+} is indeed asymmetric and the excited state structure should display large Pb^{2+} lone-pair activity.

Table 5.6 Born effective charges of RbPbCO_3F and CsPbCO_3F in units of electrons

Atom	Ionic	RbPbCO ₃ F		CsPbCO ₃ F	
		Z^*_{11}	Z^*_{33}	Z^*_{11}	Z^*_{33}
Pb	+2	3.6	3.2	3.7	3.00
Cs, Rb	+1	1.2	1.4	1.3	1.5
C	+4	2.7	0.1	2.8	0.04
O(1)	-2	-2.3	-0.5	-2.3	-0.6
O(2)	-2	-2.3	-0.5	-2.3	-0.6
O(3)	-2	-2.3	-0.5	-2.3	-0.6
F	-1	-0.7	-3.3	-0.9	-2.9

We next explore how the atomic structure supports the bonding interactions giving rise to these density distributions and use a structural approach to explain contributions to the acentric properties. We compute the total mode-distortion vector for each compound following the procedure described by Wu *et al.*¹¹ Note that we were unable to identify a pseudosymmetric centrosymmetric structure that obeyed constraints

on integer stoichiometry attributable to Wyckoff site splitting; therefore, we perform the analysis using an idealized $P\bar{6}m2$ structure while including the fractional site occupancies. We find the amplitude of the mode-polarization vectors to be 0.48Å and 0.55Å for RbPbCO₃F and CsPbCO₃F, respectively, with the main atomic displacements connecting the idealized structures via distortions of the anionic network from oxygen and fluorine displacements in the *ab*-plane. Next, we obtain the specific acentric-mode displacements¹¹ (SAMD), which corresponds to the normalized amplitude of the inversion lifting displacements described by the mode-polarization vector per unit cell volume. We find values of $4.03 \times 10^{18} \text{ \AA/cm}^3$ and $4.29 \times 10^{18} \text{ \AA/cm}^3$ for in RbPbCO₃F and CsPbCO₃F, respectively.

Consistent with the acentric mode displacement analysis we find that the converse piezoelectric charge coefficients, d_{33} , for RbPbCO₃F (72 pm/V) is lower than that of CsPbCO₃F (94 pm/V). These values are larger than those observed in α -SiO₂ (2.3 pm/V),⁷⁹ LiNbO₃ (15 pm/V),⁷⁹ K_{2.70}Pb_{5.15}(CO₃)₅F₃ (20 pm/V),⁵⁹ and are similar to those of Ba_{1-x}La_xTi_{1-x}Cr_xO₃ (70 pm/V),⁸⁰ (Bi_{0.5}Na_{0.5})_{0.95}Ba_{0.05}TiO₃ (95 pm/V).⁸¹ The structural origin of the piezoelectric behavior may also be attributable magnitude of the SAMD, because when the voltage is applied the sample undergoes macroscopic strain⁸² that is mediated by strain-polarization coupling owing to the co-parallel arrangement and constructive interaction of the carbonate units associated with the electronic flexibility in the system. The more total polarizability the material arises, the greater piezoelectric response is observed.

On the basis of the understanding formulated for the fluoro-carbonates synthesized in this work and the fact that the SAMD metric provide a meaningful way to measure the deviation from centricity for structures with different cell volumes, we now explore the correlations between the counterions (alkaline) and central metals in the broader family of known three-dimensional alkaline metal fluorcarbonates, including those reported elsewhere (see Table 5.7). Figure 5.11 shows the variance in the metal ionic radii positively correlates with the SAMD in $A^{1+}M^{2+}$ fluoro-carbonates, which cluster into two distinct groups indicated by filled circles (red symbols) and squares (blue symbols). The best linear fit to the data (gray line) gives a cross-correlation coefficient of 0.82, indicating that the ionic radii size mismatch between the alkali and divalent cations provides a reasonable measure of the acentricity of the structure. As the cation variance increases the amplitude of the inversion breaking distortions increase (SAMD becomes larger), which is indicative of an enhanced structural-contribution to the SHG response.⁶¹ Above a value of approximately 0.07 \AA^2 , which separates the fluoro-carbonate compounds into two clusters, a unit cell tripling is observed. The volume change coincides with the crossover from a carbonate topology with fully aligned triangular moieties to one with rotated and anti-aligned triangular units (Figure 5.11, inset). Note that the RbPbCO_3F and CsPbCO_3F compounds synthesized in this work are found below that transition region with the two largest SAMD values in the fluoro-carbonate grouping distinguished by fully aligned $[\text{CO}_3]^{2-}$ triangles.

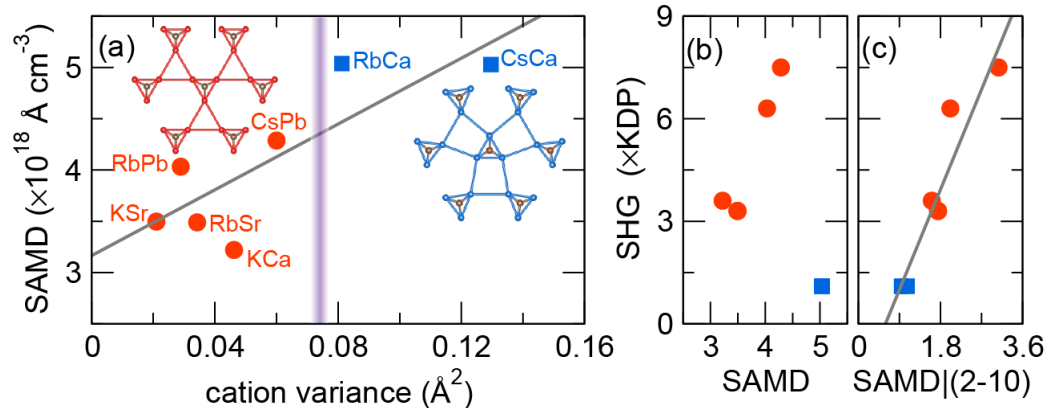


Figure 5.11 (a) Relationship between the alkali metal and divalent cations in three-dimensional fluorocarbonates and the specific acentric-mode displacements (SAMD). All structures exhibit the D_{3h} point symmetry, with the different symbols (colors) corresponding to compounds with $Z=1$ (circles, red) or $Z=3$ (squares, blue) separated by a vertical bar (gradient). The grey line is a linear least squares fit to the data ($R=0.82$). Insets depict the $[\text{CO}_3]^{2-}$ topology, other atoms omitted for clarity. SHG efficiency for the same compounds relative to (b) the total SAMD and (c) the projection of SAMD onto the $(2\bar{1}0)$ plane.

A simplistic view of this correlation would suggest that the NLO response should increase with the value of the specific acentric-mode displacements. Figure 5.11b shows the experimentally measured SHG intensity relative to that of KDP with respect to the calculated SAMD values for each compound. The differentiation between the fluorocarbonates with $Z=1$ and $Z=3$ becomes increasingly apparent. Despite an increase in the SAMD value, the anti-alignment of the carbonate groups for $Z=3$ RbCaCO_3F and CsCaCO_3F reduces the SHG response. *Thus, for achiral and non-polar compounds, large SAMD does not guarantee that a large NLO response will result; the relative orientation of the displacements contributing to the mode-polarization amplitude need to be considered.* This becomes more evident if the acentric displacements used in the SAMD

calculations are projected onto a plane of reduced symmetry, for example, the $(2\bar{1}0)$ plane corresponding to a vertex of the Reuleaux triangle along which the PbO_6F_2 exhibit *local* dipoles, as way to we separate the contributions to SAMD from the acentric distortions from those which occur because of the change in translational symmetry. For structures with $Z=1$ and space group $P\bar{6}m2$ this coincides with a mirror plane that is absent in the $Z=3$ $P\bar{6}2m$ structures. Figure 5.11c shows the projected quantity, $\text{SAMD}|_{(2\bar{1}0)}$, is less than the full value of the SAMD, because it provides a measure of the local acentric displacements relative to these crystal symmetries rather than the cooperative effect. Thus while the RbCaCO_3F and CsCaCO_3F structures appear to be more distorted (Figure 5.11a) relative to those fluoro-carbonates synthesized here, i.e., the large SAMD value derives largely from the rotations of the carbonate groups which lead to the anti-alignment and cell tripling distortion. The additive nature of the acentric moieties leads to a net reduction in SHG; indeed a least squares linear fit of the projected acentricity descriptor (Figure 5.11c), which only considers such displacements relative to directions of symmetries that generate enantiomorphic pairs, is positively correlated with the experimental SHG intensity ($R=0.94$). The analysis of local displacements relative to inversion generating operations is important when explaining the SHG efficiency when the crystal structure is non-polar but non-centrosymmetric and provides an intuitive way to understand the relationships between acentric physical properties and missing symmetry elements.

Table 5.7 Summary of A-M-CO₃-F (A = Na, K, Rb or Cs) compounds

	Radius ratio of A ⁺ /M ⁿ⁺	Structural dimension	Centricity	Space group	ref
Na ₃ La ₂ (CO ₃) ₄ F	0.976	2	CS	<i>P6₃/mmc</i>	55
NaLa ₂ (CO ₃) ₃ F	0.976	3	NCS	<i>P$\bar{6}$m2</i>	83
Na ₃ Ce ₂ (CO ₃) ₄ F	0.992	2	CS	<i>P6₃/mmc</i>	69
NaCe ₂ (CO ₃) ₃ F	0.992	3	NCS	<i>P$\bar{6}$m2</i>	83
KPb ₂ (CO ₃) ₂ F	1.07	2	CS	<i>P6₃/mmc</i>	59
K _{2.70} Pb _{5.15} (CO ₃) ₅ F ₃	1.07	2	NCS	<i>P$\bar{6}$m2</i>	59
NaYCO ₃ F ₂	1.09	3	CS	<i>Pm$\bar{c}n$</i>	84
NaYbCO ₃ F ₂	1.14	3	CS	<i>Pnma</i>	52
KSrCO ₃ F	1.23	3	NCS	<i>P$\bar{6}$m2</i>	51
RbPbCO ₃ F	1.26	3	NCS	<i>P$\bar{6}$m2</i>	this work
RbSrCO ₃ F	1.29	3	NCS	<i>P$\bar{6}$m2</i>	51
KGdCO ₃ F ₂	1.36	3	CS	<i>Fddd</i>	85
K ₄ Gd ₂ (CO ₃) ₃ F ₄	1.36	3	NCS	<i>R32</i>	86
CsPbCO ₃ F	1.38	3	NCS	<i>P$\bar{6}$m2</i>	⁶⁰ and this work
KCaCO ₃ F	1.38	3	NCS	<i>P$\bar{6}$m2</i>	51
RbCaCO ₃ F	1.54	3	NCS	<i>P$\bar{6}$2m</i>	51
CsCaCO ₃ F	1.68	3	NCS	<i>P$\bar{6}$2m</i>	51
KCuCO ₃ F	2.38	3	NCS	<i>Pmc2₁</i>	87

5.5 Conclusions

We synthesized and characterized two acentric alkali-metal lead fluorocarbonates, namely, RbPbCO_3F and CsPbCO_3F . Both materials exhibit achiral and nonpolar noncentrosymmetric 3D structures. Powder SHG measurements revealed efficiencies of approximately 250 and $300 \times \alpha\text{-SiO}_2$ with d_{33} piezoelectric charge constants of approximately 72 and 94 pm/V for RbPbCO_3F and CsPbCO_3F , respectively. SAMD analyses reveal that the nonlinear optical response is derived from the locally polar PbO_6F_2 units and the cooperatively aligned triangular carbonate units. Importantly, we find that large inversion symmetry lifting distortions, large SAMD values, which sum to form the mode-polarization amplitude, do not guarantee a large SHG response; the relative orientation of the displacements contributing to the mode-polarization amplitude need to be taken into account when discussing acentric structure – property relationships especially for achiral and nonpolar acentric structures. By examining the anisotropy in the charge distribution and dynamical charges, we identified key directions of reduced symmetry in the fluorocarbonate crystal structures that provide a positive correlation between the amplitude of the atomic displacements and the SHG. This analysis enabled a quantitative assessment and atomic scale explanation of the origin of the enhanced frequency doubling in CsPbCO_3F compared to RbPbCO_3F . We plan to explore the generality of this conclusion in a variety of acentric materials beyond fluorocarbonates, with structures crystallizing in polar, nonpolar, chiral, and achiral symmetries.

5.6 References

- (1) Lu, H.; Gautier, R.; Donakowski, M. D.; Tran, T. T.; Edwards, B. W.; Nino, J. C.; Halasyamani, P. S.; Liu, Z.; Poeppelmeier, K. R. *J. Am. Chem. Soc.* **2013**, *135*, 11942.
- (2) Zhang, M.; Pan, S.; Yang, Z.; Wang, Y.; Su, X.; Yang, Y.; Huang, Z.; Han, S.; Poeppelmeier, K. R. *J. Mater. Chem. C* **2013**, *1*, 4740.
- (3) Huang, H.; He, R.; Yao, W.; Lin, Z.; Chen, C.; Zhang, Y. *J. Cryst. Growth* **2013**, *380*, 176.
- (4) Matyjasik, S.; Shaldin, Y. V. *Low Temp. Phys.* **2013**, *39*, 967.
- (5) Kesim, M. T.; Zhang, J.; Trolrier-McKinstry, S.; Mantese, J. V.; Whatmore, R. W.; Alpay, S. P. *J. Appl. Phys.* **2013**, *114*, 204101/1.
- (6) Luo, K.; Johnson, R. D.; Tran, T. T.; Halasyamani, P. S.; Radaelli, P. G.; Hayward, M. A. *Chem. Mater.* **2013**, *25*, 1800.
- (7) Padhee, R.; Das, P. R.; Parida, B. N.; Choudhary, R. N. P. *J. Electron. Mater.* **2013**, *42*, 426.
- (8) Pandey, R.; Meena, B. R.; Singh, A. K. *arXiv.org, e-Print Arch., Condens. Matter* **2013**, 1.
- (9) Freitas, V. F.; Protzek, O. A.; Montoro, L. A.; Goncalves, A. M.; Garcia, D.; Eiras, J. A.; Guo, R.; Bhalla, A. S.; Cotica, L. F.; Santos, I. A. *J. Mater. Chem. C* **2014**, *2*, 364.
- (10) Gautier, R.; Norquist, A. J.; Poeppelmeier, K. R. *Cryst. Growth Des.* **2012**, *12*, 6267.

- (11) Wu, H.; Yu, H.; Yang, Z.; Hou, X.; Su, X.; Pan, S.; Poeppelmeier, K. R.; Rondinelli, J. M. *J. Am. Chem. Soc.* **2013**, *135*, 4215.
- (12) Zhang, G.; Li, Y.; Jiang, K.; Zeng, H.; Liu, T.; Chen, X.; Qin, J.; Lin, Z.; Fu, P.; Wu, Y.; Chen, C. *J. Am. Chem. Soc.* **2012**, *134*, 14818.
- (13) Yan, X.; Luo, S.; Lin, Z.; Yue, Y.; Wang, X.; Liu, L.; Chen, C. *J. Mater. Chem. C* **2013**, *1*, 3616.
- (14) Wu, H.; Pan, S.; Poeppelmeier, K. R.; Li, H.; Jia, D.; Chen, Z.; Fan, X.; Yang, Y.; Rondinelli, J. M.; Luo, H. *J. Am. Chem. Soc.* **2011**, *133*, 7786.
- (15) Young, J.; Rondinelli, J. M. *Chem. Mater.* **2013**, *25*, 4545.
- (16) Gou, G.; Rondinelli, J. M. *arXiv.org, e-Print Arch., Condens. Matter* **2013**, *1*.
- (17) Mulder, A. T.; Benedek, N. A.; Rondinelli, J. M.; Fennie, C. J. *Adv. Funct. Mater.* **2013**, *23*, 4810.
- (18) Fry, A. M.; Seibel, H. A.; Lokuhewa, I. N.; Woodward, P. M. *J. Am. Chem. Soc.* **2012**, *134*, 2621.
- (19) Fry, A. M.; Woodward, P. M. *Cryst. Growth Des.* **2013**, *13*, 5404.
- (20) Turp, S. A.; Hargreaves, J.; Baek, J.; Halasyamani, P. S.; Hayward, M. A. *Chem. Mater.* **2010**, *22*, 5580.
- (21) Benedek, N. A.; Fennie, C. J. *J. Phys. Chem. C* **2013**, *117*, 13339.
- (22) Benedek, N. A.; Mulder, A. T.; Fennie, C. J. *J. Solid State Chem.* **2012**, *195*, 11.
- (23) Ke, X.; Birol, T.; Misra, R.; Lee, J. H.; Kirby, B. J.; Schlom, D. G.; Fennie, C. J.; Freeland, J. W. *Phys. Rev. B: Condens. Matter Mater. Phys.* **2013**, *88*, 094434/1.

- (24) Olshansky, J. H.; Tran, T. T.; Hernandez, K. J.; Zeller, M.; Halasyamani, P. S.; Schrier, J.; Norquist, A. J. *Inorg. Chem.* **2012**, *51*, 11040.
- (25) Koffer, J. H.; Olshansky, J. H.; Smith, M. D.; Hernandez, K. J.; Zeller, M.; Ferrence, G. M.; Schrier, J.; Norquist, A. J. *Cryst. Growth Des.* **2013**, *13*, 4504.
- (26) Yang, B.-P.; Hu, C.-L.; Xu, X.; Huang, C.; Mao, J.-G. *Inorg Chem* **2013**, *52*, 5378.
- (27) Huang, C.; Hu, C.-L.; Xu, X.; Yang, B.-P.; Mao, J.-G. *Dalton Trans.* **2013**, *42*, 7051.
- (28) Song, J.-L.; Hu, C.-L.; Xu, X.; Kong, F.; Mao, J.-G. *Inorg Chem* **2013**, *52*, 8979.
- (29) Huang, C.; Hu, C.-L.; Xu, X.; Yang, B.-P.; Mao, J.-G. *Inorg. Chem.* **2013**, *52*, 11551.
- (30) Meier, D.; Lilienblum, M.; Becker, P.; Bohaty, L.; Spaldin, N. A.; Ramesh, R.; Fiebig, M. *Phase Transitions* **2013**, *86*, 33.
- (31) Artyukhin, S.; Delaney, K. T.; Spaldin, N. A.; Mostovoy, M. *Nat. Mater.* **2013**, *13*, 8.
- (32) Garcia-Castro, A. C.; Spaldin, N. A.; Romero, A. H.; Bousquet, E. *Condens. Matter* **2013**, *1*.
- (33) Inaguma, Y.; Aimi, A.; Shirako, Y.; Sakurai, D.; Mori, D.; Kojitani, H.; Akaogi, M.; Nakayama, M. *J. Am. Chem. Soc.* **2014**, *136*, 2748.
- (34) Taniguchi, H.; Kuwabara, A.; Kim, J.; Kim, Y.; Moriwake, H.; Kim, S.; Hoshiyama, T.; Koyama, T.; Mori, S.; Takata, M.; Hosono, H.; Inaguma, Y.; Itoh, M. *Angew. Chem., Int. Ed.* **2013**, *52*, 8088.

- (35) Inaguma, Y.; Sakurai, D.; Aimi, A.; Yoshida, M.; Katsumata, T.; Mori, D.; Yeon, J.; Halasyamani, P. S. *J. Solid State Chem.* **2012**, *195*, 115.
- (36) Nguyen, S. D.; Yeon, J.; Kim, S.-H.; Halasyamani, P. S. *J. Am. Chem. Soc.* **2011**, *133*, 12422.
- (37) Nguyen, S. D.; Kim, S.-H.; Halasyamani, P. S. *Inorg. Chem.* **2011**, *50*, 5215.
- (38) Yeon, J.; Kim, S.-H.; Nguyen, S. D.; Lee, H.; Halasyamani, P. S. *Inorg. Chem.* **2012**, *51*, 609.
- (39) Yeon, J.; Kim, S.-H.; Nguyen, S. D.; Lee, H.; Halasyamani, P. S. *Inorg. Chem.* **2012**, *51*, 2662.
- (40) Nguyen, S. D.; Halasyamani, P. S. *Inorg Chem* **2013**, *52*, 2637.
- (41) Kim, S.-H.; Yeon, J.; Halasyamani, P. S. *Chem. Mater.* **2009**, *21*, 5335.
- (42) Halasyamani, P. S. *Chem. Mater.* **2004**, *16*, 3586.
- (43) Pachoud, E.; Zhang, W.; Tapp, J.; Liang, K.-C.; Lorenz, B.; Chu, P. C. W.; Halasyamani, P. S. *Cryst. Growth Des.* **2013**, *13*, 5473.
- (44) Opik, U.; Pryce, M. H. L. *Proc. R. Soc. London, Ser. A* **1957**, *238*, 425.
- (45) Pearson, R. G. *J. Mol. Struct.: THEOCHEM* **1983**, *12*, 25.
- (46) Wheeler, R. A.; Whangbo, M. H.; Hughbanks, T.; Hoffmann, R.; Burdett, J. K.; Albright, T. A. *J. Am. Chem. Soc.* **1986**, *108*, 2222.
- (47) Goodenough, J. B. *Annu. Rev. Mater. Sci.* **1998**, *28*, 1.
- (48) Ye, N.; Chen, Q.; Wu, B.; Chen, C. *J. Appl. Phys.* **1998**, *84*, 555.
- (49) Grice, J. D.; Maisonneuve, V.; Leblanc, M. *Chem. Rev.* **2007**, *107*, 114.
- (50) Luo, M.; Ye, N.; Zou, G.; Lin, C.; Cheng, W. *Chem. Mater.* **2013**, *25*, 3147.

- (51) Zou, G.; Ye, N.; Huang, L.; Lin, X. *J. Am. Chem. Soc.* **2011**, *133*, 20001.
- (52) Ben, A. A.; Leblanc, M.; Maisonneuve, V. *Acta Crystallogr., Sect. E: Struct. Rep. Online* **2006**, *62*, i133.
- (53) Ben, A. A.; Maisonneuve, V.; Leblanc, M. *Solid State Sci.* **2002**, *4*, 1367.
- (54) Mercier, N.; Leblanc, M. *Acta Crystallogr., Sect. C: Cryst. Struct. Commun.* **1994**, *C50*, 1864.
- (55) Mercier, N.; Taulelle, F.; Leblanc, M. *Eur. J. Solid State Inorg. Chem.* **1993**, *30*, 609.
- (56) Mercier, N.; Leblanc, M. *Eur. J. Solid State Inorg. Chem.* **1993**, *30*, 217.
- (57) Ben, A. A.; Maisonneuve, V.; Smiri, L. S.; Leblanc, M. *Solid State Sci.* **2002**, *4*, 891.
- (58) Ben, A. A.; Maisonneuve, V.; Kodjikian, S.; Smiri, L. S.; Leblanc, M. *Solid State Sci.* **2002**, *4*, 503.
- (59) Tran, T. T.; Halasyamani, P. S. *Inorg. Chem.* **2013**, *52*, 2466.
- (60) Zou, G.; Huang, L.; Ye, N.; Lin, C.; Cheng, W.; Huang, H. *J. Am. Chem. Soc.* **2013**, *135*, 18560.
- (61) Cammarata, A.; Rondinelli, J. M. *ACS Photonics* **2014**, *1*, 96.
- (62) Brown, I. D.; Altermatt, D. *Acta Crystallogr., Sect. B: Struct. Sci.* **1985**, *B41*, 244.
- (63) Brown, I. D. *The Chemical Bond in Inorganic Chemistry*; Oxford University Press: New York, 2002; Vol. 12.
- (64) Kampf, A. R.; Yang, H.; Downs, R. T.; Pinch, W. W. *Am. Mineral.* **2011**, *96*, 402.

- (65) Marukhnov, A. V.; Pushkin, D. V.; Serezhkin, V. N. *Russ. J. Coord. Chem.* **2008**, *34*, 570.
- (66) Shannon, R. D. *Acta Crystallogr., Sect. A* **1976**, *A32*, 751.
- (67) Grice, J. D.; Van, V. J.; Gault, R. A. *Can. Mineral.* **1994**, *32*, 405.
- (68) Grice, J. D.; Gault, A.; Van, V. J. *Can. Mineral.* **1997**, *35*, 181.
- (69) Grice, J. D.; Chao, G. Y. *Am. Mineral.* **1997**, *82*, 1255.
- (70) Donoghue, M.; Hepburn, P. H.; Ross, S. D. *Spectrochim. Acta. A* **1971**, *27*, 1065.
- (71) Andersen, F. A.; Brecevic, L. *Acta Chem. Scand.* **1991**, *45*, 1018.
- (72) Refat, M. S.; Elsabawy, K. M. *Bull. Mater. Sci.* **2011**, *34*, 873.
- (73) Nakamoto, K.; Wiley online, I. *Infrared and Raman Spectra of Inorganic and Coordination Compounds*; Wiley ; John Wiley Hoboken, N.J. : Chichester, 2007.
- (74) M.Kubelka, P.; Munk, F. Z. *Tech. Phys.* **1931**, *12*, 593.
- (75) Tauc, J. *Mater. Res. Bull.* **1970**, *5*, 721.
- (76) Oka, K.; Unoki, H.; Sakudo, T. *J. Cryst. Growth* **1979**, *47*, 568.
- (77) Kurtz, S. K.; Perry, T. T. *J. Appl. Phys.* **1968**, *39*, 3798.
- (78) Griffiths, D.; Culpin, D. *Mathl. Gaz.* **1975**, *59*, 165.
- (79) Xu, Y. *Ferroelectric Materials and Their Applications*; Elsevier Science Publishers: Amsterdam, 1991.
- (80) Fukunaga, M.; Uesu, Y. *Jpn. J. Appl. Phys., Part 1* **2003**, *42*, 6115.
- (81) Roy, A. K.; Prasad, K.; Prasad, A. *Process. Appl. Ceram.* **2013**, *7*, 81.
- (82) Ok, K. M.; Chi, E. O.; Halasyamani, P. S. *Chem. Soc. Rev.* **2006**, *35*, 710.

- (83) Piilonen, P. C.; McDonald, A. M.; Grice, J. D.; Cooper, M. A.; Kolitsch, U.; Rowe, R.; Gault, R. A.; Poirier, G. *Mineral. Mag.* **2010**, *74*, 257.
- (84) Grice, J. D.; Chao, G. Y. *Can. Mineral.* **1997**, *35*, 743.
- (85) Mercier, N.; Leblanc, M.; Antic-Fidancev, E.; Lemaitre-Blaise, M.; Porcher, P. *J. Alloys Compd.* **1995**, *225*, 198.
- (86) Mercier, N.; Leblanc, M.; Durand, J. *Eur. J. Solid State Inorg. Chem.* **1997**, *34*, 241.
- (87) Mercier, N.; Leblanc, M. *Eur. J. Solid State Inorg. Chem.* **1994**, *31*, 423.

Chapter 6 Deep Ultra-Violet Nonlinear Optical Alkali-Metal Magnesium Fluorocarbonates KMgCO_3F and RbMgCO_3F

This chapter is partially based on the results that has been submitted “Tran, T. T.; He, J.; Rondinelli, J. M.; Halasyamani, P. S., RbMgCO_3F : A New Deep-Ultraviolet Nonlinear Optical Material, *Angew. Chem.* **2015**, submitted.”

6.1 Abstract

Two new deep-ultraviolet nonlinear optical (NLO) materials, KMgCO_3F and RbMgCO_3F , have been synthesized and characterized. The materials were synthesized through solvothermal and conventional solid-state techniques. KMgCO_3F and RbMgCO_3F were structurally characterized by single crystal X-ray diffraction and exhibit three-dimensional (3D) crystal structures of corner-shared $\text{Mg}(\text{CO}_3)_2\text{F}_2$ polyhedra. Unlike other acentric fluorocarbonates, the inclusion of Mg^{2+} in RbMgCO_3F creates pentagonal channels where the Rb^+ resides. KMgCO_3F exhibits structurally similar packing to RbMgCO_3F , however, one CO_3 unit was observed to be statistically disordered. Both materials crystallize in the achiral and non-polar space group $P\bar{6}2m$ (crystal class $\bar{6}2m$). KMgCO_3F and RbMgCO_3F are SHG active at both 1064 nm and 532 nm with efficiencies of 120 and $160 \times \alpha\text{-SiO}_2$ and 0.33 and $0.60 \times \beta\text{-BaB}_2\text{O}_4$, respectively. The materials exhibit short UV cut-offs, below 200 nm and 190 nm for KMgCO_3F and RbMgCO_3F , respectively. Charge constants, d_{33} , of approximately 38 and 49 pm/V were obtained for KMgCO_3F and RbMgCO_3F , respectively, through converse piezoelectric measurements. Our electronic structure calculations reveal that the density of the

carbonate linkage, monodentate or bidentate, to the divalent cation is a useful parameter for tuning the transparency window and achieving the sizeable SHG response.

6.2 Introduction

Materials capable of generating coherent deep-ultraviolet (DUV) light, $\lambda < 200\text{nm}$, $E_g > 6.2\text{eV}$, are of intense academic and technological interest.¹⁻¹⁰ Generating coherent deep-UV light may be done through cascaded frequency conversion of nonlinear optical (NLO) materials, i.e., 6th harmonic generation of 1064nm (Nd:YAG) radiation to 177.3nm. From a crystal design and synthetic chemistry perspective, it is an ongoing challenge to discover a new material that is crystallographically non-centrosymmetric (NCS), exhibits a wide band gap (large transparency window), has a large second-harmonic generating (SHG) coefficient with moderate birefringence, is chemically stable with a large laser damage threshold, and is easy to grow as large (cm^3) single crystals. Technologically, these materials are used in photolithography, atto-second pulse generation, and advanced instrument development.¹¹⁻¹³ Currently, only $\text{KBe}_2\text{BO}_3\text{F}_2$ (KBBF) is capable of generating coherent light below 200nm.¹⁴ With KBBF, single crystals tend to layer along their optical axis thus hindering their practical applications.¹⁵⁻¹⁷ Also, the need for highly toxic BeO in their synthesis and crystal growth complicates the detailed investigation of their properties. Thus, it is of great interest to discover DUV NLO materials that do not contain beryllium.

Other than KBBF, NCS borates are the most common materials for deep-UV NLO applications. LiB_3O_5 (LBO)¹⁸ and CsB_3O_5 (CBO)¹⁸⁻¹⁹ have absorption edges of 155nm

and 167nm respectively. The poor birefringence in both materials, 0.045 (LBO)²⁰ and 0.063 (CBO),¹⁹ prevent them from being used for deep-UV NLO applications. β -BaB₂O₄ (β -BBO) has an appropriate birefringence, 0.1127,²¹ however its absorption edge of 185nm²⁰ preclude the material from being used for 6th harmonic Nd:YAG generation. A number of other methods have been discussed for designing new NLO materials. These include using cations susceptible to second-order Jahn-Teller (SOJT) distortions,²²⁻²⁵ cations with a stereo-active lone-pair,²⁶⁻³⁴ and asymmetric chalcogenide polyhedra.³⁵⁻³⁷ An issue with all of these design strategies is that the absorption edge is red-shifted. Thus the materials are not suitable for deep-UV NLO applications.

Mixed-metal fluorocarbonates, which are accessible through hydrothermal synthesis, are a promising³⁸ materials family³⁹ for DUV NLO applications. Two unique attributes they exhibit include (i) fully bonded (CO₃)²⁻ units, i.e. there is (are) no dangling oxygen atoms(s). It has been shown in borates that the terminal oxygen atom red-shifts the absorption edge, making it difficult to reach the DUV.⁴⁰⁻⁴² (ii) The inclusion of fluoride also blue-shifts the absorption edge.^{6,17} Thus the materials are much more amenable to transmission in the DUV. Recently, two families of NCS fluorocarbonates have been reported - ABCO₃F (A⁺ = K, Rb, Cs; B²⁺ = Ca, Sr, Ba, and Pb)⁴³ and Na₈Lu₂(CO₃)₆F₂ and Na₈Lu(CO₃)₂F₂.⁴⁴ Although quantitative measurements of the optical gaps have yet to be determined, all materials are reported to have an absorption edge below 200nm. Remarkably, the B=Mg member of this family has gone unreported, likely attributable to the low decomposition temperature of MgCO₃ compared with the other alkaline-earth carbonates.

In this chapter, we report the solid-state and hydrothermal synthesis of the achiral non-polar non-centrosymmetric (NCS) KMgCO_3F and RbMgCO_3F . An unique pentagonal planar arrangement of $\text{Mg}_3(\text{CO}_3)_3$ owing to the A and B cation variance was observed in RbMgCO_3F . KMgCO_3F possesses structurally akin packing to the Rb compound, however, a CO_3 group was found to be disordered. It exhibits powder SHG responses at both 1064 nm and 532 nm incident radiation with short absorption edges, below 200 nm and 190 nm for KMgCO_3F and RbMgCO_3F , respectively. Electronic structures calculations on RbMgCO_3F reveal that although the compound exhibits enhanced acentric displacements, which usually anti-correlate with the SHG response in these fluorocarbonates, this compound delivers an enhanced response owing to the non-uniform mono- and bidentate ligand bonding of Mg^{2+} . The results indicate KMgCO_3F and RbMgCO_3F could be excellent candidates for optical technologies operating in the DUV utilizing nonlinear light-matter interactions.

6.3 Results and Discussion

6.3.1 Structures

Details of the synthesis and characterizations are presented in Chapter 3. The semi-quantitative EDS measurements were taken three times from the selected KMgCO_3F and RbMgCO_3F crystals that were used for X-ray diffraction analysis. The average K:Mg and Rb:Mg ratios of 0.96(9) and 1.06(7), respectively, found by EDS is in excellent agreement with the value of 1.00 determined by least squares refinement of the X-ray data. Relevant crystallographic data, selected bond distances and angles, atomic

coordinates and equivalent isotropic displacement parameters for KMgCO_3F and RbMgCO_3F are given in Tables 6.1 – 6.4.

Table 6.1 Crystallographic data for KMgCO_3F and RbMgCO_3F

	KMgCO_3F	RbMgCO_3F
M/gmol ⁻¹	142.42	188.79
T/K	293(2)	293(2)
$\lambda/\text{\AA}$	0.71073	0.71073
Crystal system	Hexagonal	Hexagonal
Space group	$P\bar{6}2m$ (No. 189)	$P\bar{6}2m$ (No. 189)
$a/\text{\AA}$	8.8437(2)	9.0160(3)
$c/\text{\AA}$	3.9254(1)	3.9403(2)
$V/\text{\AA}^3$	265.88(2)	277.39(2)
Z	3	3
d_c/gcm^{-3}	2.668	3.390
μ/mm^{-1}	1.550	13.438
$2\theta_{\text{max}}/^\circ$	55.84	75.52
R_{int}	0.0182	0.0152
GOF	1.157	1.027
$R(\text{F})^a$	0.0492	0.0087
$R_w(\text{F}_o^2)^b$	0.1165	0.0199
Flack parameter	0.119(5)	0.022(5)
Largest diff. peak/hole (e \AA^{-3})	0.680/-0.652	0.314/-0.327
^a $R(\text{F}) = \Sigma \text{F}_o - \text{F}_c /\Sigma \text{F}_o $. ^b $R_w(\text{F}_o^2) = [\Sigma w(\text{F}_o^2 - \text{F}_c^2)^2/\Sigma w(\text{F}_o^2)^2]^{1/2}$		

Table 6.2 Selected bond distances (Å) and angles (deg) for KMgCO₃F and RbMgCO₃F

KMgCO ₃ F		RbMgCO ₃ F	
Mg – O(1)	1.9926(4)	Mg – O(1) × 2	1.9937(9)
Mg – O(1)'	2.0891(3)		
Mg – O(2) × 2	2.2284(5)	Mg – O(2) × 2	2.1960(1)
Mg – F × 2	1.9637(5)	Mg – F × 2	1.9703(2)
C(1) – O(1) × 3	1.2540(3)	C(1) – O(1) × 3	1.2724(11)
C(1) – O(1)' × 3	1.1840(2)		
C(2) – O(2) × 3	1.3288(4)	C(2) – O(2) × 3	1.2842(7)
O(1) – Mg – O(1)	86.44(2)	O(1) – Mg – O(1)	104.03(8)
O(1)' – Mg – O(1)'	130.98(2)		
O(1) – Mg – O(2)	105.63(2)	O(1) – Mg – O(2)	97.56(5)
O(1)' – Mg – O(2)	83.28(2)		
O(2) – Mg – O(2)	62.18(2)	O(2) – Mg – O(2)	60.85(6)
F – Mg – O(1)	88.92(2)	F – Mg – O(1)	90.39(2)
F – Mg – O(1)'	88.01(2)		
F – Mg – O(2)	88.46(2)	F – Mg – O(2)	89.45(3)
F – Mg – F	176.41(2)	F – Mg – F	178.72(8)

Table 6.3 Atomic coordinates and equivalent isotropic displacement parameters (\AA^2) for KMgCO_3F . All atoms were refined anisotropically except disordered O1 and O1'.

Atom	x	y	z	U_{eq}^a
K	0.0000	0.3711(4)	0.0000	0.0265(10)
Mg	0.0000	0.7091(5)	0.5000	0.0176(13)
C1	0.3333	0.6667	0.5260(2)	0.0110(5)
C2	0.0000	0.0000	0.5000	0.0120(5)
O1(0.60(3))	0.1782(17)	0.6342(17)	0.4793(13)	0.0230(5)
O1'(0.40(3))	0.2480(3)	0.7360(3)	0.4793(13)	0.0200(5)
O2	0.0000	0.1503(12)	0.5000	0.0180(2)
F	0.2840(2)	0.2840(2)	0.0000	0.0280(2)

^a U_{eq} is defined as one-third of the trace of the orthogonalized U_{ij} tensor

Table 6.4 Atomic coordinates and equivalent isotropic displacement parameters (\AA^2) for RbMgCO_3F

Atom	x	y	z	U_{eq}^a
Rb	0.0000	0.3825(2)	0.0000	0.0147(4)
Mg	0.0000	0.7188(6)	0.5000	0.0087(9)
C1	0.3333	0.6667	0.5000	0.0094(2)
C2	0.0000	0.0000	0.5000	0.0091(3)
O1	0.2012(2)	0.6833(2)	0.5000	0.0246(2)
O2	0.0000	0.1424(2)	0.5000	0.0117(2)
F	0.2788(2)	0.2788(2)	0.0000	0.0167(2)

^a U_{eq} is defined as one-third of the trace of the orthogonalized U_{ij} tensor

KMgCO₃F and RbMgCO₃F crystallize in achiral non-polar space group $P\bar{6}2m$ and exhibit a three-dimensional crystal structure consisting of corner-sharing Mg(CO₃)₃F₂ polyhedra (see Figure 6.1–6.2).

In KMgCO₃F structure, the Mg²⁺ cations are connected to three carbonate groups, i.e., two [C(1)O(1)₃]²⁻ units and one [C(2)O(2)₃]²⁻ in the *ab*-plane, and a bridging fluoride along the *c*-direction (see Figure 6.1). The K⁺ cations are located in the cavities formed between the Mg(CO₃)₃F₂ groups. Two [C(1)O(1)₃]²⁻ groups are observed to be statistically disordered in two different orientations with population of 0.60(3):0.40(3). In connectivity terms, the materials may be described as [Mg(CO₃)_{3/3}F_{2/2}]⁻ anions, with charge balance maintained by one K⁺ cation. Each Mg²⁺ cation in MgO₄F₂ is bonded to four oxygen atoms and two fluorine atoms in a distorted octahedral coordination environment, with Mg–O distances of 1.9926(4)–2.2284(5) Å and a Mg–F distance of 1.9637(5) Å. The carbonate C–O bond distances range from 1.1840(2) to 1.2540(3) Å. The K⁺ cation is surrounded by six oxygen atoms and three fluorine atoms, with K–O distances of 2.750(4)–2.769(8) Å and K–F distances of 2.973(4)–3.050(10) Å. Bond valence calculations resulted in values of 1.11, 1.92 and 3.60–4.08 for K⁺, Mg²⁺ and C⁴⁺, respectively (Table 6.5).

With respect to RbMgCO₃F structure, the Mg²⁺ cations are connected to three carbonate groups in the *ab*-plane, and a bridging fluoride along the *c*-direction (see Figure 6.2). The Rb⁺ cations are located in the cavities formed between the Mg(CO₃)₃F₂ groups. In connectivity terms, the materials may be described as [Mg(CO₃)_{3/3}F_{2/2}]⁻ anions, with charge balance maintained by one Rb⁺ cation. Each Mg²⁺ cation in MgO₄F₂ is

bonded to four oxygen atoms and two fluorine atoms in a distorted octahedral coordination environment, with Mg–O distances of 1.9937(17)–2.1960(13) Å and a Mg–F distance of 1.9703(2) Å. The carbonate C–O bond distances range from 1.2724(9) to 1.2842(6) Å. The Rb⁺ cation is surrounded by six oxygen atoms and three fluorine atoms, with Rb–O distances of 2.9262(8)–3.0991(8) Å and Rb–F distances of 3.0533(6)–3.0893(9) Å. Bond valence calculations resulted in values of 1.00, 2.09 and 3.99–4.12 for Rb⁺, Mg²⁺ and C⁴⁺, respectively (Table 6.5). The thermal anisotropic displacements of KMgCO₃F and RbMgCO₃F are depicted in Figure 6.3.

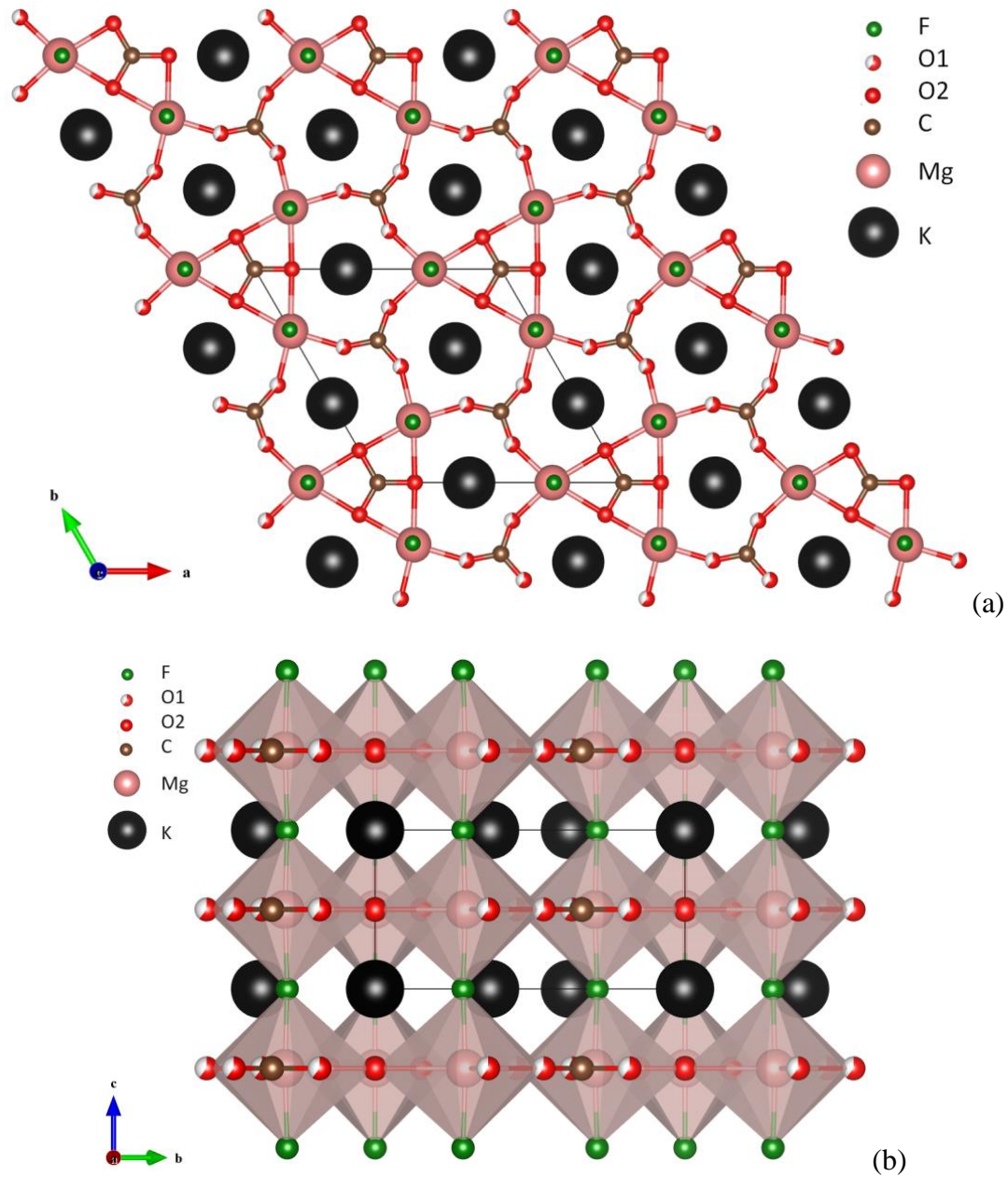


Figure 6.1 Ball-and-stick in the ab -plane (a), and polyhedral in the bc -plane (b) representations of KMgCO_3F . Only one position of the disordered $[\text{CO}_3]^{2-}$ in the structure is shown.

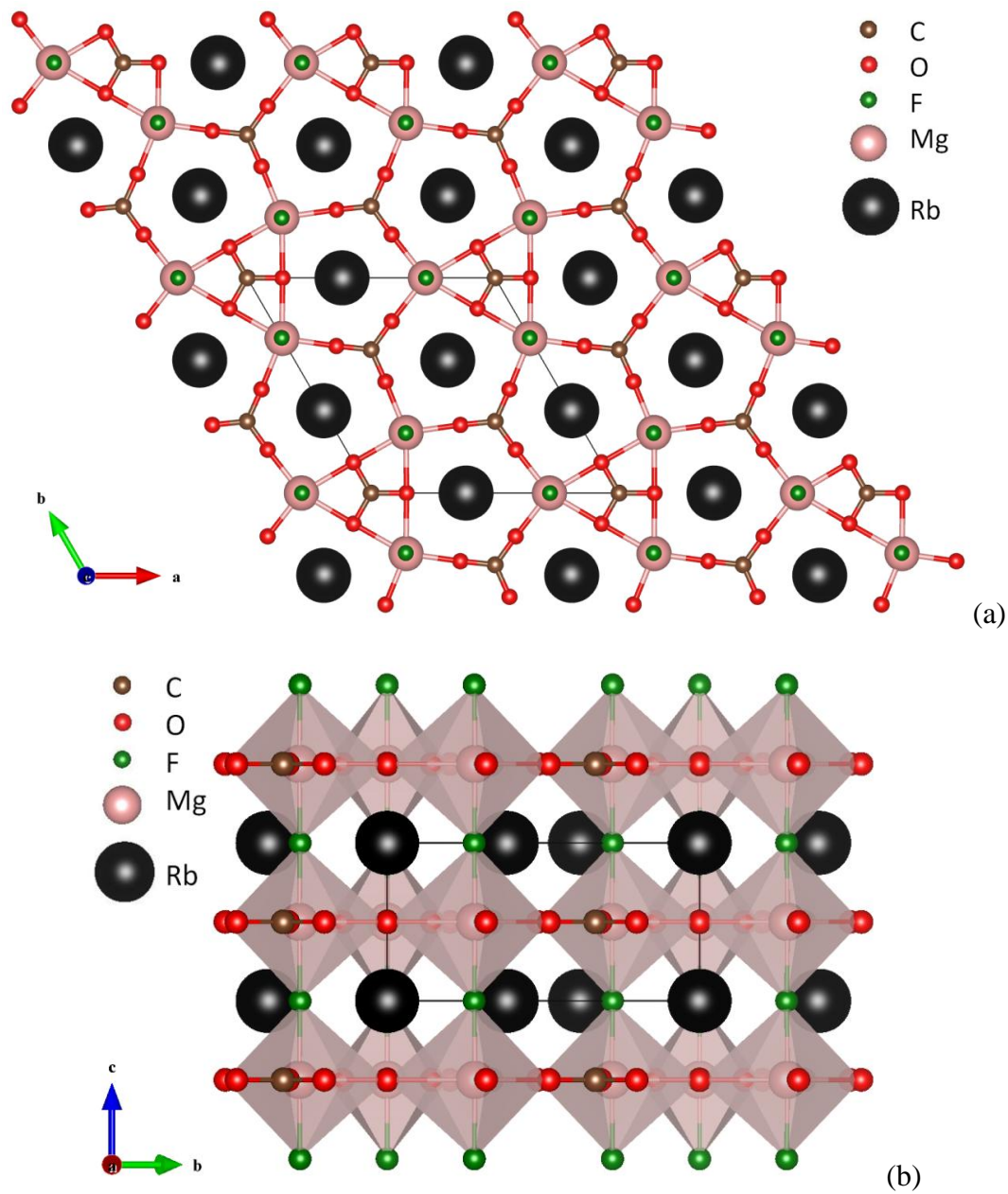


Figure 6.2 Ball-and-stick in the ab -plane (a), and polyhedral in the bc -plane (b) representations of RbMgCO_3F . In (a) note that the Rb cations reside in pentagonal tunnels created by the Mg polyhedra. In (b) note that the Mg polyhedra are connected by bridging fluorine atoms.

Further examination of the two related materials, KMgCO_3F and RbMgCO_3F , reveals some similarities and differences in the crystallographic architecture. These materials both crystallize in the hexagonal $P\bar{6}2m$ space group with the c -axes nearly identical (3.9254(1) vs 3.9403(2) Å for the K and Rb compounds respectively) since the parameters are defined by the Mg–F bond distances. The a and b unit cell parameters, however, are different (8.8437(2) (K) vs 9.0160(3) Å (Rb)), and these are a function of the $\text{Mg}(\text{CO}_3)_3$ bonding patterns associated with the size of the alkaline cation (see Figures 6.1 and 6.2). KMgCO_3F and RbMgCO_3F are structurally similar and built up from the $\text{Mg}(\text{CO}_3)_3\text{F}_2$ building units. With respect to the 'A⁺' cations, the effective ionic radii are 1.55 and 1.63 Å for K^+ and Rb^+ , respectively.⁴⁵ If we replace K^+ with the larger cation Rb^+ in the structure, we notice that the cavity separation is not very big. In other words, when the larger cation Rb^+ is introduced into the crystal structure, the structural strain is produced inside the cavities between the $\text{Mg}(\text{CO}_3)_3\text{F}_2$ frameworks. To minimize this strain, the $\text{Mg}(\text{CO}_3)_3$ layers need to slightly separate in the ab -plane to accommodate the larger cation Rb^+ . This phenomenon is clearly observed in the increase of the a - and b -axes of unit cell parameters (see Table 6.1). The the a - and b -axes of RbMgCO_3F are longer than that of KMgCO_3F , whereas the c -axis remains essentially constant. In addition, the packing of both materials are similar, it is, however, observed that KMgCO_3F structure possesses a disorder of one $[\text{CO}_3]$ unit whereas RbMgCO_3F structure is entirely ordered.

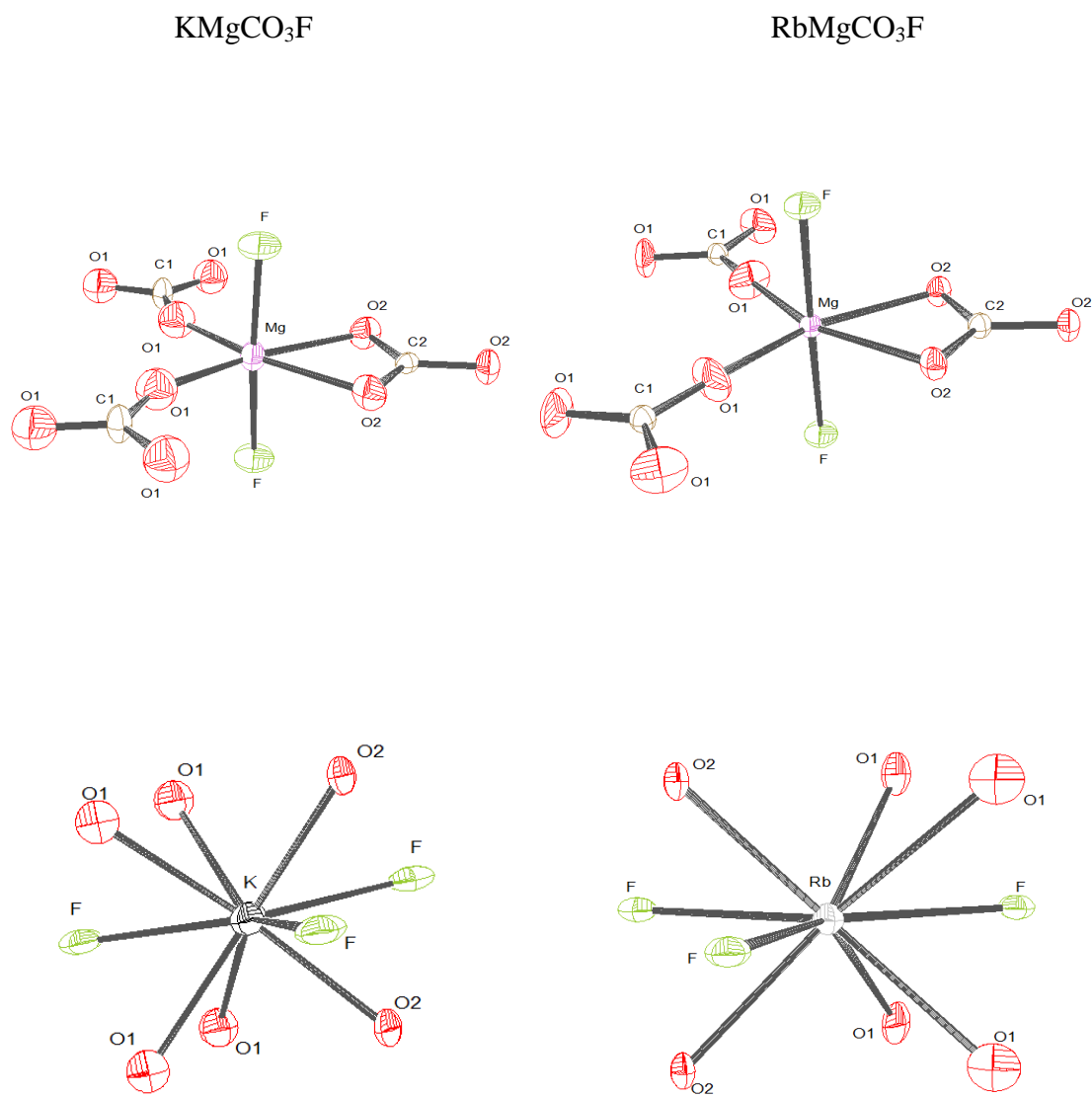


Figure 6.3 ORTEP (50% ellipsoid probability) diagrams for KMgCO_3F and RbMgCO_3F . Note that only one position of the disordered $[\text{C}(1)\text{O}(1)_3]$ in KMgCO_3F is shown.

The coordination environment of the Mg^{2+} cation in KMgCO_3F and RbMgCO_3F is entirely different from the known alkaline-earth cations in the ABCO_3F fluorocarbonate family (Figure 6.4). Mg^{2+} is found in a distorted octahedral coordination environment, MgO_4F_2 , whereas other alkaline-earth cations are higher-fold coordinated, i.e., CaO_5F_2 (7-fold) in $\text{Rb}(\text{Cs})\text{CaCO}_3\text{F}$ and CaO_6F_2 (8-fold) in KCaCO_3F , SrO_6F_2 (8-fold) in $\text{K}(\text{Rb})\text{SrCO}_3\text{F}$, BaO_6F_3 (9-fold) and BaO_6F_4 (10-fold) $\text{Cs}_3\text{Ba}_4(\text{CO}_3)_3\text{F}_5$.⁴³ This evolution is attributed to the difference in the effective ionic radii, i.e., the radius of Mg^{2+} (0.72 Å, 6 coordination number (C.N.)) is significantly smaller than those of other alkaline-earth cations, Ca^{2+} (1.06 Å, 7 C.N. and 1.12 Å, 8 C.N.), Sr^{2+} (1.26 Å, 8 C.N.) and Ba^{2+} (1.47 Å, 9 C.N. and 1.52 Å, 10 C.N.).⁴⁵

The coordination environment also produces a unique bonding pattern of $[\text{Mg}(\text{CO}_3)]_\infty$ layers. The layers are arranged in a pentagonal fashion in the (001) plane of RbMgCO_3F that is not observed in the other members of the ABCO_3F family. The Mg^{2+} cation is bonded to four oxygen atoms: two ligands, O(2), from one carbonate CO_3^{2-} group (bidentate) and the other two from two oxygen atoms, O(1), from separate (monodentate) CO_3^{2-} groups (see Figure 6.4). This does not occur for the Ca^{2+} and Sr^{2+} cations in ABCO_3F (A = K, Rb, Cs, B = Ca, Sr). In $[\text{B}(\text{CO}_3)]_\infty$ layers of ABCO_3F , the Ca^{2+} cation can be connected to either (i) five oxygen atoms: four from two bidentate CO_3^{2-} groups and one from single CO_3^{2-} group (RbCaCO_3F and CsCaCO_3F) or (ii) six oxygen atoms from three bidentate CO_3^{2-} units (KCaCO_3F).⁴³ For the Sr^{2+} cation, in KSrCO_3F and RbSrCO_3F , the bonding pattern of $[\text{Sr}(\text{CO}_3)]_\infty$ is similar to $[\text{Ca}(\text{CO}_3)]_\infty$ (see Figure 6.4).⁴³ This change in denticity can be distinguished using a formalism introduced

in Ref. 45, which relies on the variance between the ionic radii of the A and B cations. Here we compute a cation radii variance of 0.21 \AA^2 for RbMgCO_3F , which places it well-beyond the range previously established to be compatible with aligned carbonate groups and three bidentate linkages ($\sim 0.07 \text{ \AA}^2$, see Figure 6.4, right).⁴⁶ Note that the former stability range was established for fluorocarbonates with a single formula unit per unit cell, $Z=1$, whereas RbMgCO_3F is more similar to RbCaCO_3F and CsCaCO_3F with $Z=3$ and two bidentate linkages (variance $> \sim 0.07$, see Figure 6.4, center). Here we report the first member within what is likely a family of compounds with $Z=3$ and a single bidentate linkage of the B^{2+} cation in achiral non-polar NCS fluorocarbonates (Figure 6.4, left).

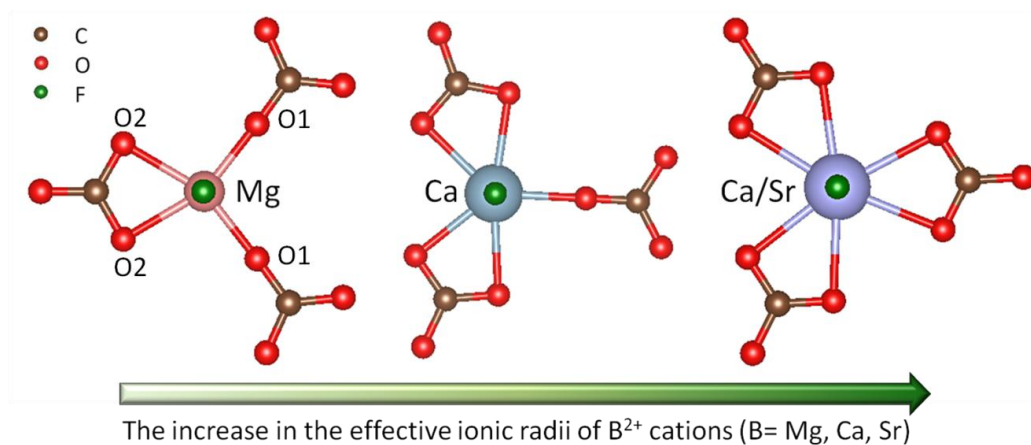


Figure 6.4 Different coordination denticities for B^{2+} cations ($\text{B} = \text{Mg}, \text{Ca}, \text{Sr}$) in ABCO_3F materials ($\text{A} = \text{K}, \text{Rb}, \text{Cs}$). Note that unique to Mg^{2+} cation, two monodentate and one bidentate linkages are observed.

Table 6.5 Bond valence analysis for KMgCO_3F^a

Atom	O1(60%)	O1'(40%)	O2	F	Σ cations
K	0.137 ^[x4]	0.153 ^[x4]	0.169 ^[x2]	0.071 ^[x2] 0.057	1.11
Mg	0.445 ^[x2]	0.343 ^[x2]	0.202 ^[x2]	0.353 ^[x2]	1.92
C1	1.44 ^[x3]	1.24 ^[x3]			4.08
C2			1.18 ^[x3]		3.60
Σ anions		1.90	1.56	0.904	

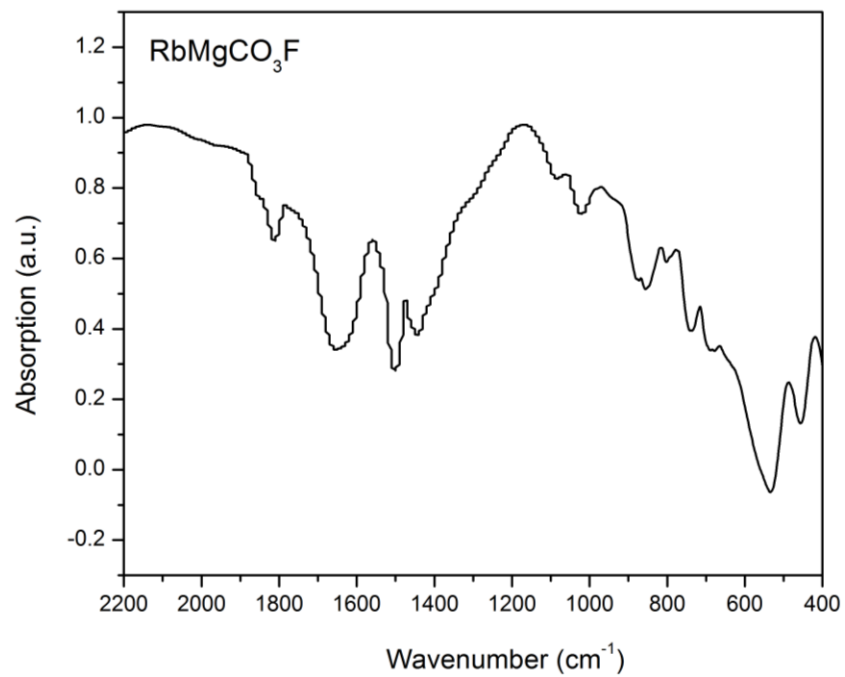
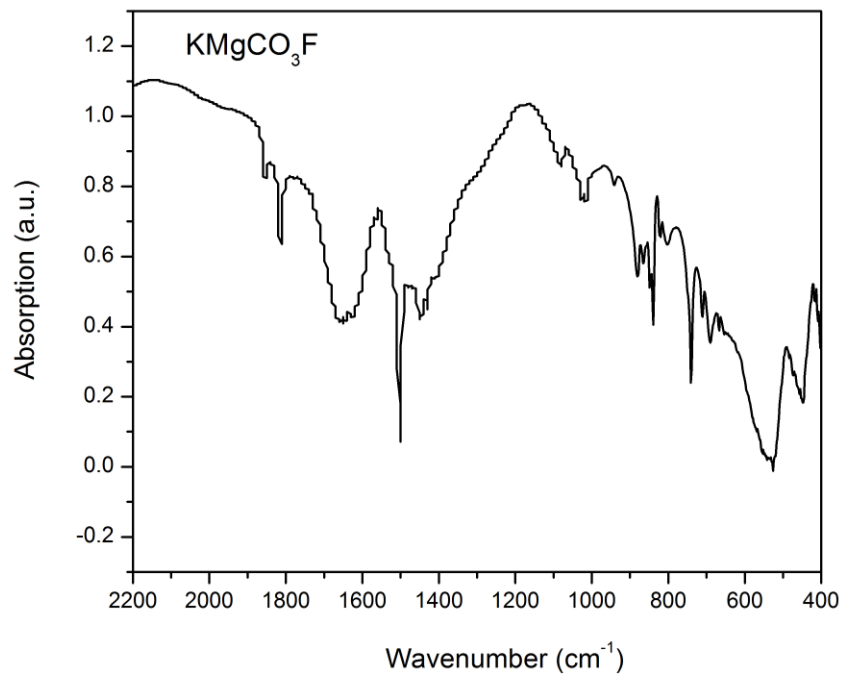
Table 6.5 Bond valence analysis for $\text{RbMgCO}_3\text{F}^a$

Atom	O1	O2	F	Σ cations
Rb	0.104 ^[x4]	0.167 ^[x2]	0.081 ^[x2] 0.089	1.00
Mg	0.444 ^[x2]	0.257 ^[x2]	0.346 ^[x2]	2.09
C1	1.37 ^[x3]			4.11
C2		1.33 ^[x3]		3.99
Σ anions	1.92	1.76	0.944	

^a Bond valence sums calculated with the formula: $S_i = \exp[(R_o - R_i)/B]$, where S_i =valence of bond "i" and $B=0.37$.

6.3.2 Infrared (IR) Spectroscopy

The infrared (IR) spectra of KMgCO_3F and RbMgCO_3F revealed C–O vibrations between $1800\text{--}680\text{cm}^{-1}$. The strong broad bands observed at $1800\text{--}1450\text{ cm}^{-1}$ can be assigned to the stretching C–O vibrations. The out-of-plane vibration, $\delta(\text{OCO})$, is observed in the range of $900\text{--}800\text{ cm}^{-1}$, and the bending vibration, $\delta(\text{OCO})$, appears at $700\text{--}680\text{ cm}^{-1}$.⁴⁷ The $\nu(\text{Mg--O})$ vibration is observed in the range of $830\text{--}790\text{ cm}^{-1}$, which can be partially overlapped with $\delta(\text{OCO})$.⁴⁷ The bands observed at $540\text{--}450\text{ cm}^{-1}$ correspond to the $\nu(\text{Mg--F})$ stretching vibration.⁴⁸ The infrared spectra are presented in Figure 6.5.



cm^{-1}	$\nu(\text{C-O})$	$\delta(\text{OCO})$	$\nu(\text{Mg-O})$	$\nu(\text{Mg-F})$
KMgCO_3F	1695, 1502	904, 685	838, 790	536, 452
RbMgCO_3F	1650, 1495	890, 680	830, 790	540, 450

Figure 6.5 IR spectra of KMgCO_3F and RbMgCO_3F

6.3.3 UV-Vis Transmission Spectroscopy

The UV-Vis transmission spectra indicate that KMgCO_3F and RbMgCO_3F exhibit wide transparency windows, with absorption edges below 200 nm and 190 nm, respectively.

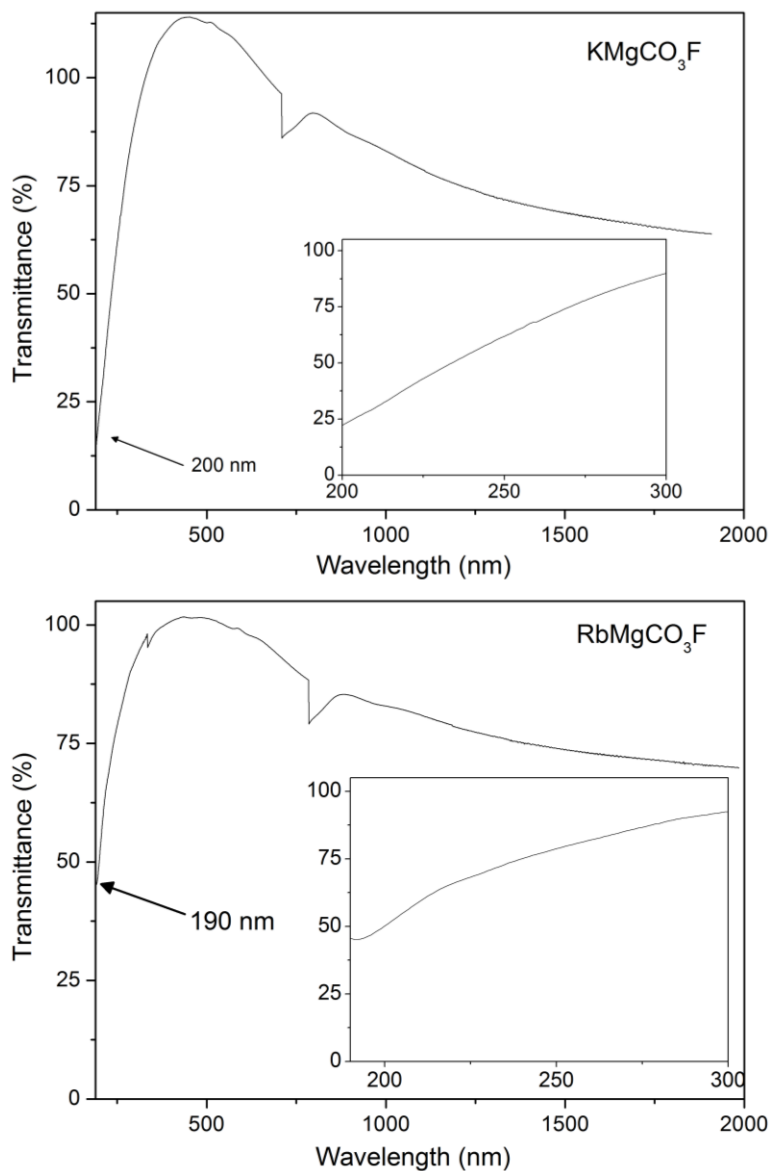


Figure 6.6 UV-Vis transmission spectra of KMgCO_3F and RbMgCO_3F . The ‘spike’ at ~800 nm is artifact attributable to the detector change.

Even at 200 nm and 190 nm, the transmission for KMgCO_3F and RbMgCO_3F is nearly 25% and 50%, respectively. This would indicate that these materials are promising deep-UV NLO materials. The UV-Vis transmission spectra are presented in Figure 6.6.

6.3.4 Thermal Analysis

The thermal behaviors of KMgCO_3F and RbMgCO_3F were investigated using thermogravimetric analysis (TGA) and differential thermal analysis (DTA) under N_2 atmosphere. The decomposition of KMgCO_3F and RbMgCO_3F begins at approximately 390 and 400°C, respectively, corresponding to the loss of CO_2 . The experimental weight loss is in good agreement with the calculated weight loss. The endothermic peaks in the heating curve are consistent with the decomposition of the material. At approximately 600°C, the drop in mass was observed in the TGA plot that is likely attributable to the loss of fluorides. The exothermic peaks in the cooling cycle indicate re-crystallization of the residues occurred at approximately 830, 775°C for KMgCO_3F and 760, 615°C for RbMgCO_3F . That is confirmed by the appearance of MgO and unidentified phases in powder XRD pattern of the residuals. The DTA/TGA diagrams for KMgCO_3F and RbMgCO_3F are depicted in Figure 6.7 .

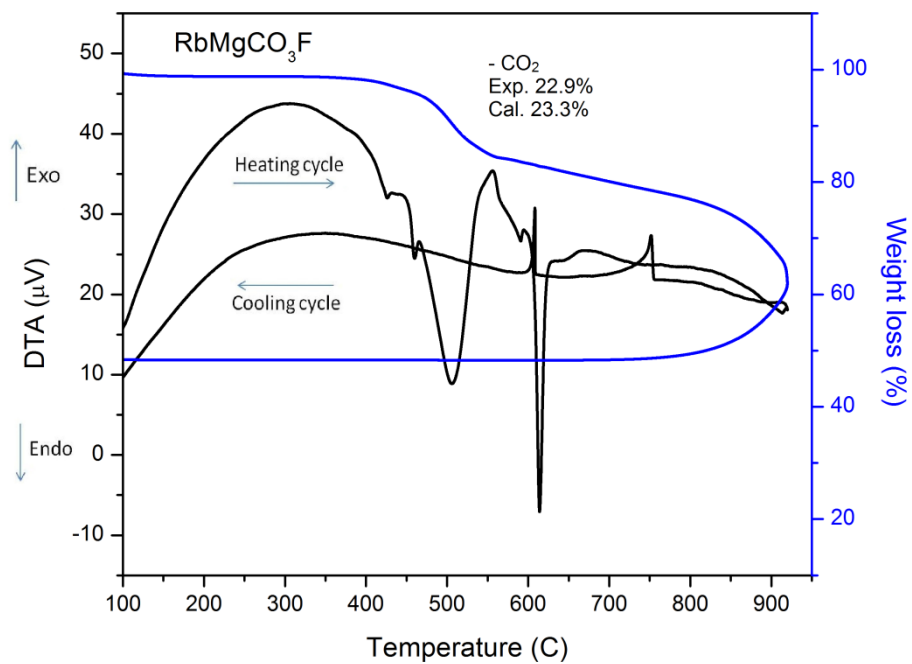
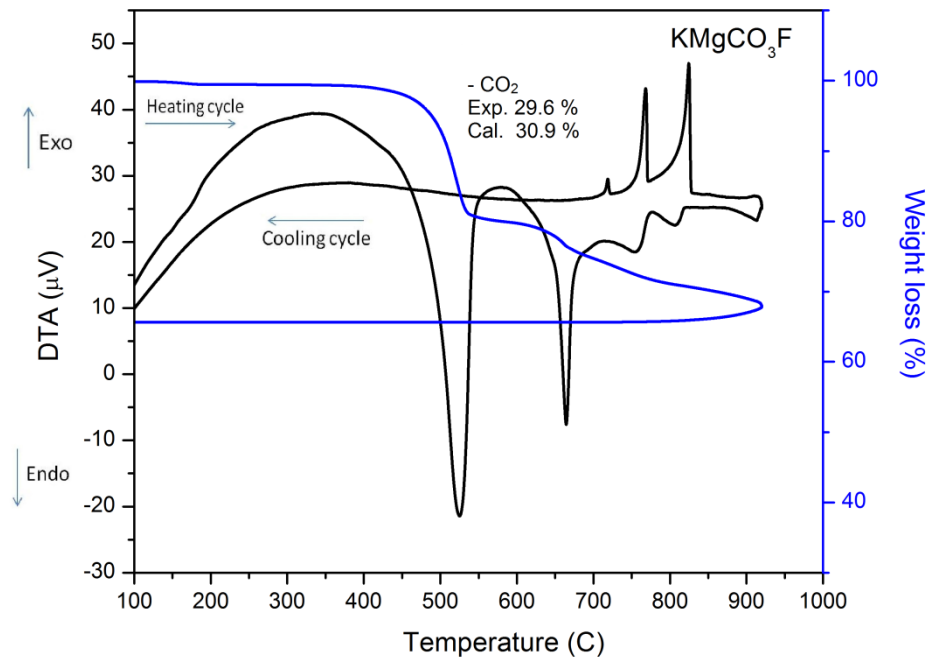


Figure 6.7 Thermogravimetric analysis and differential thermal analysis diagram of KMgCO_3F and RbMgCO_3F under N_2

6.3.5 Second-Harmonic Generation (SHG) and Piezoelectric Measurements

Motivated by the unusual connectivity of KMgCO_3F and RbMgCO_3F and the NCS space group $P\bar{6}2m$, we investigated the SHG and piezoelectric properties.

Powder SHG measurements for KMgCO_3F and RbMgCO_3F using 1064nm and 532nm radiation revealed a SHG efficiency of approximately 120, $160 \times \alpha\text{-SiO}_2$ and 0.33, $0.60 \times \beta\text{-BBO}$, respectively, in the 45–63 μm particle size range. Additional SHG measurements, particle size vs. SHG efficiency, indicate the material exhibits type 1 phase-matching behavior (see Figure 6.8 – 6.9). As such KMgCO_3F and RbMgCO_3F fall into the class A category of SHG materials, as defined by Kurtz and Perry.⁴⁹

Converse piezoelectric measurements on KMgCO_3F and RbMgCO_3F were also performed and piezoelectric charge constants, d_{33} , of approximately 38 and 49 pm/V were determined, respectively (see Figure 6.10).

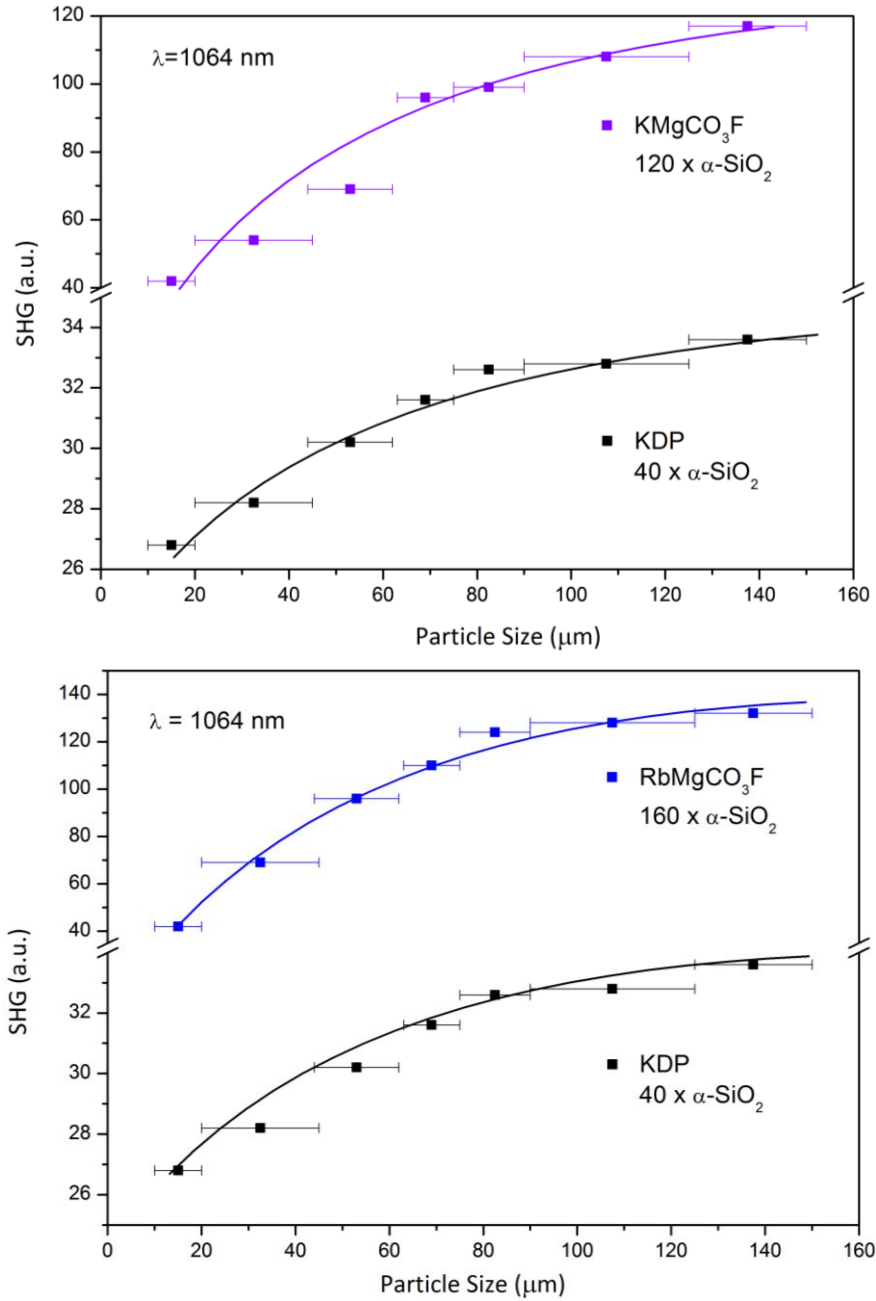


Figure 6.8 Powder second-harmonic generation for KMgCO_3F and RbMgCO_3F at 1064 nm incident radiation. Curves are drawn to guide the eye and are not a fit to the data.

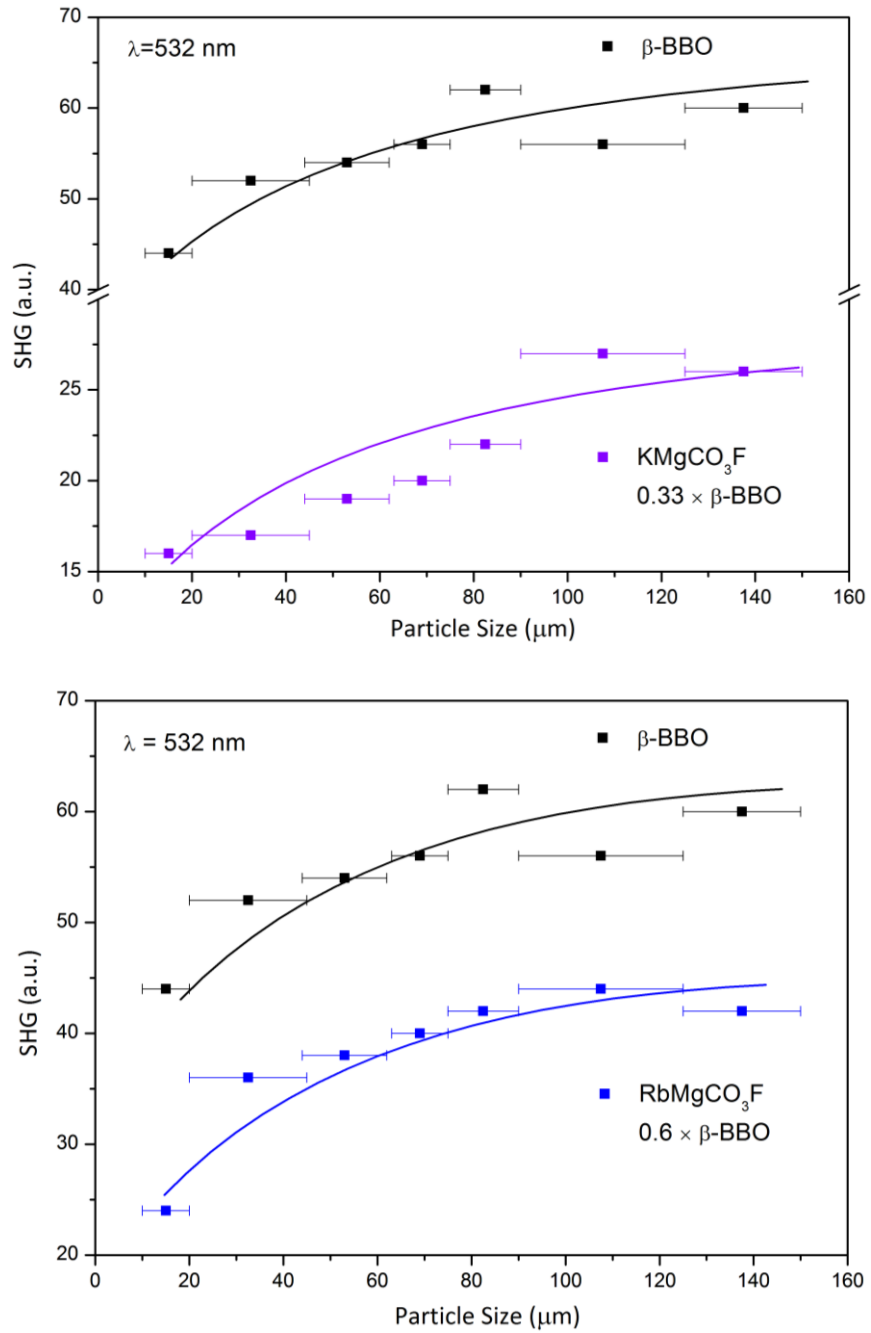


Figure 6.9 Powder second-harmonic generation for KMgCO_3F and RbMgCO_3F at 532 nm incident radiation. Curves are drawn to guide the eye and are not a fit to the data.

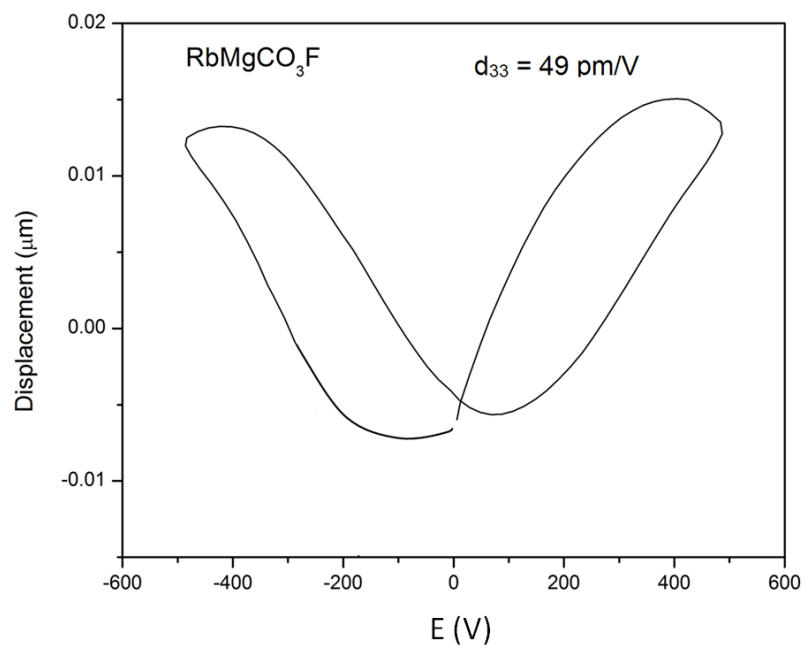
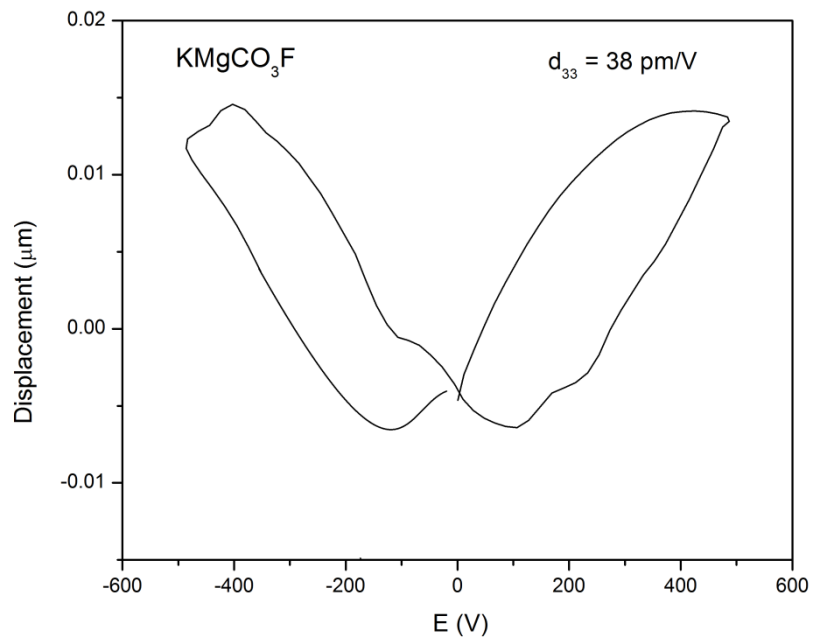


Figure 6.10 Displacement vs. applied voltage for KMgCO_3F and RbMgCO_3F

6.3.7 Electronic Structure

Figure 6.11 shows the atom-resolved density of states (DOS) for RbMgCO₃F. The calculated band gap using PBEsol is 4.75 eV, which is ~2 eV smaller than experimental value due to the systematic band gap underestimation of the semi-local functional. The calculated band gap of RbMgCO₃F is much larger than that of RbPbCO₃F calculated at the same theoretical level, consistent with our experiments. The smaller band gap for RbPbCO₃F is mainly a consequence of the lone pair on Pb²⁺. The electronic structure of RbMgCO₃F is also sharply different compared with RbPbCO₃F in that the valence band maximum (VBM) and conduction band minimum (CBM) are dominated by O 2p and Rb 5s states, respectively, because Mg²⁺ is fully ionized and contributes states far from the Fermi energy. Upon atomic decomposition of the DOS, we find that the states at the VB edge derive from the oxygen ligands O(1) bonded in a monodentate fashion with Mg whereas the O(2) atoms with bidentate bonding are found lower in energy (approximately -2 to -1 eV). The fluorine 2p states, as expected, are found below those of both oxygen atoms within the energy range of -4 to -2.5 eV (not shown).

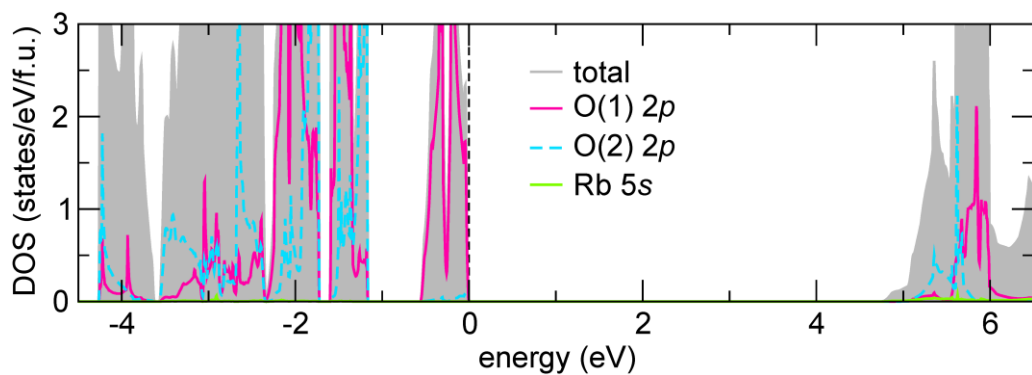


Figure 6.11 DOS for RbMgCO₃F decomposed by atomic site and orbital contributions. O(1) and O(2) correspond to Mg ligands which bond to monodentate and bidentate [CO₃]²⁻ groups, respectively

6.4 Relationship between Electronic Structure, NCS Structures and Acentric Crystal Properties

To understand in detail how the atomic structure provides for this electronic structure configuration and a SHG efficiency at 1064nm, intermediate between RbPbCO₃F (6.25 × KDP) and RbSrCO₃F (3.33 × KDP), we compute the specific acentric mode displacements (SAMD).⁶ The calculated SAMD according to the previous definition⁴⁶ applied to fluorocarbonates is $5.77 \times 10^{18} \text{ \AA/cm}^3$, which is larger than that of all RbB²⁺CO₃F (see Figure 6.12). The mode consists mainly of oxygen and fluorine displacements within the ab-plane. As pointed out in our previous work, however, large SAMD does not necessitate a large NLO response since three dipolar moments in $P\bar{6}2m$ align along the principal directions of a Reuleaux triangle located on the B²⁺ cation site and macroscopically cancel.⁴⁶ The moderate SHG intensity in RbMgCO₃F is attributable to the increased SAMD in the achiral NCS material, which although indicating a greater number of inversion symmetry lifting distortions in the structure, act to constructively cancel an induced-polarization arising from the oscillating electric field of an incident photon. The extent to which this occurs in RbMgCO₃F is examined in the inset of Figure 6.12, which depicts the electron localization function (ELF) in the (001) plane. As common to the NCS fluorocarbonates, we find clover-like electron density motifs for the carbonate units, however, those oxygen ligands forming a monodentate link to Mg²⁺ are more dimpled than those with the bidentate connectivity. As described in one of our earlier studies,⁴⁶ The B²⁺ cation is usually located at the center of a *regular* Reuleaux triangle formed by the non-bonding oxygen charge density. Interestingly, we find this

triangle should be puckered in RbMgCO_3F , along the $[120]$ direction (see blue bolded arrow in Figure 6.12) as a direct consequence of the single bidentate bonding geometry.

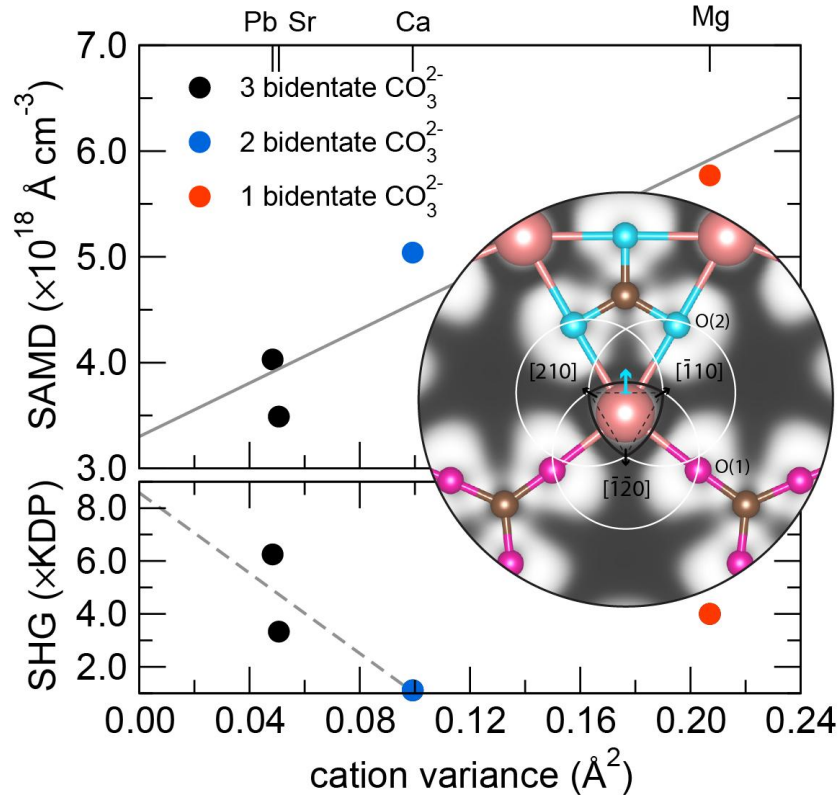


Figure 6.12 Effect of Rb and B cation variance on the carbonate linkage in RbBCO_3F fluorocarbonates. The density of acentric displacements as parameterized in the SAMD value (see text) increases with the change in bonding of the B^{2+} cation with the carbonate group (top). The SHG response is anti-correlated with the cation variance for two and three bidentate carbonate groups (bottom), whereas the behaviour of RbMgCO_3F is found to be an outlier owing to reduced polarizable charge density in response to an electric-field. The inset depicts charge-density contours of the ELF (ELF=0.85) in the (001) plane about the Mg site with the static asymmetry greater than that found for the other compounds. The Reuleaux triangle construction is highlighted and because of the bonding environment should be puckered (no longer regular) along the vertical direction indicated by the (blue) arrow.

As a result, there is a greater static asymmetric distribution of charge. Nonetheless, the reduced electronic polarizability of Mg^{2+} , i.e., its position in the periodic table is above all of the other B^{2+} cations found in $\text{RbB}^{2+}\text{CO}_3\text{F}$ provides a *reduction* to the electronic component of the SHG from the induced charge density oscillations under optical excitation.⁵⁰ RbMgCO_3F then exhibits a response less than RbPbCO_3F , but greater than the Sr and Ca analogues owing to the local asymmetry in the Mg–O bond lengths from the denticity, i.e., C–O(1) bond length is 0.012 Å shorter than C–O(2).

6.5 Conclusions

We synthesized and characterized two new acentric alkali–alkaline-earth fluorocarbonates, namely, KMgCO_3F and RbMgCO_3F . Both materials exhibit achiral and nonpolar noncentrosymmetric 3D structures. These compounds possess unique bonding pattern of Mg polyhedra, i.e., the Mg^{2+} cation bonds to two monodentate $[\text{CO}_3]^{2-}$ units and one bidentate $[\text{CO}_3]^{2-}$ group. This powder SHG measurements revealed efficiencies of approximately 120 and $160 \times \alpha\text{-SiO}_2$ (at 1064 nm) and 0.33 and $0.60 \times \beta\text{-BBO}$ (at 532 nm) with d_{33} piezoelectric charge constants of approximately 38 and 49 pm/V for KMgCO_3F and RbMgCO_3F , respectively. Electron structure calculations indicate that the local asymmetry in Mg–O bonding pattern from the different denticity contributes to tuning the transparency window and enhancing the SHG responses.

6.6 References

- (1) Xu, K.; Loiseau, P.; Aka, G. *J. Cryst. Growth* **2009**, *311*, 2508.
- (2) Yang, Y.; Pan, S.; Hou, X.; Wang, C.; Poeppelmeier, K. R.; Chen, Z.; Wu, H.; Zhou, Z. *J. Mater. Chem.* **2011**, *21*, 2890.
- (3) Wu, H.; Pan, S.; Poeppelmeier, K. R.; Li, H.; Jia, D.; Chen, Z.; Fan, X.; Yang, Y.; Rondinelli, J. M.; Luo, H. *J. Am. Chem. Soc.* **2011**, *133*, 7786.
- (4) Zhang, M.; Pan, S.; Yang, Z.; Wang, Y.; Su, X.; Yang, Y.; Huang, Z.; Han, S.; Poeppelmeier, K. R. *J. Mater. Chem. C* **2013**, *1*, 4740.
- (5) Wu, H.; Yu, H.; Pan, S.; Huang, Z.; Yang, X.; Su, K.; Poeppelmeier, K. R. *Angew. Chem. Int. Ed. Engl.* **2013**, *52*, 3406.
- (6) Wu, H.; Yu, H.; Yang, Z.; Hou, X.; Su, X.; Pan, S.; Poeppelmeier, K. R.; Rondinelli, J. M. *J. Am. Chem. Soc.* **2013**, *135*, 4215.
- (7) Wu, H.; Wu, W.; Pan, S.; Yang, Z.; Hou, X.; Su, X.; Jing, Q.; Poeppelmeier, K. R.; Rondinelli, J. M. *J. Am. Chem. Soc.* **2014**, *136*, 1264.
- (8) Yan, X.; Luo, S.; Yao, J.; He, R.; Yue, Y.; Chen, C.; Lin, Z. *Inorg. Chem.* **2014**, *53*, 1952.
- (9) Zhao, S.; Gong, P.; Bai, L.; Xu, X.; Zhang, S.; Sun, Z.; Lin, Z.; Hong, M.; Chen, C.; Luo, J. *Nat. Commun.* **2014**, *5*, 1.
- (10) Yu, H.; Wu, H.; Pan, S.; Yang, Z.; Hou, X.; Su, X.; Jing, Q.; Poeppelmeier, K. R.; Rondinelli, J. M. *J. Am. Chem. Soc.* **2014**, *136*, 1264.
- (11) Savage, N. *Nature Phonics* **2007**, *1*, 83.

- (12) Cyranoski, D. *Nature* **2009**, *457*, 953.
- (13) Yao, W.; He, R.; Wang, X.; Lin, Z.; Chen, C. *Adv. Opt. Mater.* **2014**, *2*, 411.
- (14) Chen, C. T.; Wang, G. I.; Wang, X. Y.; Xu, Z. Y. *Appl. Phys. B* **2009**, *97*, 9.
- (15) Ye, N.; Tang, D. Y. *J. Cryst. Growth* **2006**, *293*, 233.
- (16) McMillen, C. D.; Kolis, J. W. *J. Cryst. Growth* **2008**, *310*, 2033.
- (17) Chen, C. T.; Wang, G. L.; Wang, X. Y.; Xu, Z. Y. *Appl. Phys. B* **2009**, *97*, 9.
- (18) Chen, C. T.; Wu, Y. C.; Jiang, A. D.; Wu, B. C.; You, G. M.; Li, R. K.; Lin, S. J. *J. Opt. Soc. Am. B* **1989**, *6*, 616.
- (19) Wu, Y. C.; Sasaki, T.; Nakai, N.; Yokotani, A.; Tang, H. G.; Chen, C. T. *Appl. Phys. Lett.* **1993**, *62*, 2614.
- (20) Chen, C.; Sasaki, T.; Li, R. K.; Wu, Y.; Lin, Z.; Mori, Y.; Hu, Z.; Wang, J.; Uda, S.; Yoshimura, M.; Kaneda, Y. **2012**.
- (21) Eimerl, D.; Davis, L.; Velsko, S.; Graham, E. K. *J. Appl. Phys.* **1987**, *62*, 1968.
- (22) Halasyamani, P. S.; Poepelmeier, K. R. *Chem. Mater.* **1998**, *10*, 2753.
- (23) Ra, H.-S.; Ok, K. M.; Halasyamani, P. S. *J. Am. Chem. Soc.* **2003**, *125*, 7764.
- (24) Sun, C.-F.; Hu, C.-L.; Xu, X.; Ling, J.-B.; Hu, T.; Kong, F.; Long, X.-F.; Mao, J.-G. *J. Am. Chem. Soc.* **2009**, *131*, 9486.
- (25) Donakowski, M. D.; Gautier, R.; Yeon, J.; Moore, D. T.; Nino, J. C.; Halasyamani, P. S.; Poepelmeier, K. R. *J. Am. Chem. Soc.* **2012**, *134*, 7679.
- (26) Yang, B. P.; Hu, C.-L.; Xu, X.; Sun, C.-F.; Zhang, J.-H.; Mao, J.-G. *Chem. Mater.* **2010**, *22*, 1545.

- (27) Nguyen, S. D.; Yeon, J.; Kim, S.-H.; Halasyamani, P. S. *J. Am. Chem. Soc.* **2011**, *133*, 12422.
- (28) Cao, X.-L.; Hu, C.-L.; Xu, X.; Kong, F.; Mao, J.-G. *Chem. Commun.* **2013**, *49*, 9965.
- (29) Huang, C.; Hu, C.-L.; Xu, X.; Yang, B.-P.; Mao, J.-G. *Dalton Trans.* **2013**, *42*, 7051.
- (30) Yang, B.-P.; Hu, C.-L.; Xu, X.; Huang, C.; Mao, J.-G. *Inorg. Chem.* **2013**, *52*, 5378.
- (31) Xu, X.; Yang, B.-P.; Huang, C.; Mao, J.-G. *Inorg. Chem.* **2014**, *53*, 1756.
- (32) Jo, H.; Kim, Y. H.; Lee, D. W.; Ok, K. M. *Dalton Trans.* **2014**, *43*, 11752.
- (33) Kim, Y. H.; Lee, D. W.; Ok, K. M. *Inorg. Chem.* **2014**, *53*, 5240.
- (34) Kim, Y. H.; Lee, D. W.; Ok, K. M. *Inorg. Chem.* **2014**, *53*, 1250.
- (35) Chung, I.; Kanatzidis, M. G. *Chem. Mater.* **2014**, *26*, 849.
- (36) Brant, J. A.; Clark, D. J.; Kim, Y. S.; Jang, J. I.; Zhang, J.-H.; Aitken, J. A. *Chem. Mater.* **2014**, *26*, 3045.
- (37) Rosmus, K. A.; Brant, J. A.; Wisneski, S. D.; Clark, D. J.; Kim, Y. S.; Jang, J. I.; Brunetta, C. D.; Zhang, J.-H.; Srnec, M. N.; Aitken, J. A. *Inorg. Chem.* **2014**, *53*, 7809.
- (38) Kang, L.; Luo, S.; Huang, H.; Ye, N.; Lin, Z.; Qin, J.; Chen, C. *J. Phys. Chem. C* **2013**, *117*, 25684.
- (39) Grice, J. D.; Maisonneuve, V.; Leblanc, M. *Chem. Rev.* **2007**, *107*, 114.
- (40) Chen, C. T.; Yu, W. C.; Lin, R. K. *Chin. Phys. Lett.* **1985**, *2*, 389.
- (41) Chen, C. T. *Materials for Nonlinear Optics* **1991**, *455*, 360.

- (42) Chen, C. T. *Laser Science and Technology, An International Handbook* **1993**, 15.
- (43) Zou, G.; Ye, N.; Huang, H.; Lin, X. *J. Am. Chem. Soc.* **2011**, 133, 20001.
- (44) Luo, M.; Ye, N.; Zou, G.; Lin, C.; Cheng, W. *Chem. Mater.* **2013**, 25, 3147.
- (45) Shannon, R. D. *Acta Crystallogr., Sect. A* **1976**, A32, 751.
- (46) Cammarata, A.; Zhang, W.; Halasyamani, P. S.; Rondinelli, J. M. *Chem. Mater.* **2014**, 26, 5773.
- (47) Huang, C. K.; Kerr, P. F. *Am. Mineral.* **1960**, 45, 311.
- (48) Lesiecki, M. L.; Nibler, J. W. *J. Chem. Phys.* **1976**, 64, 871.
- (49) Abrahams, S. C.; Kurtz, S. K.; Jamieson, P. B. *Phys. Rev.* **1968**, 172, 551.
- (50) Levine, B. F. *Phys. Rev. B.* **1973**, 7, 2600.

Chapter 7 A Reduced Niobium (III/IV) Oxyfluoride Nb₂O₂F₃

This chapter is mainly based on the results that has been published in “Tran, T.T.; Gooch, M.; Lorenz, B.; Litvinchuk, A. P.; Sorolla, M.; Brgoch, J.; Chu, P. L.; Guloy, A.M.; Nb₂O₂F₃: A Reduced Niobium (III/IV) Oxyfluoride with A Complex Structural, Magnetic and Electronic Phase Transition, *J. Am. Chem. Soc.*, **2015**, 137, 636”

7.1 Abstract

A new reduced niobium (III/IV) oxyfluoride, Nb₂O₂F₃, has been synthesized through the reaction of Nb, SnO and SnF₂ in Sn flux within welded Nb containers and characterized in crystal structure and physical properties. Nb₂O₂F₃ crystallizes in a monoclinic structure (space group: *I2/a*; a=5.7048(1)Å, b= 5.1610(1)Å, c = 12.2285(2)Å, β = 95.751(1)°) that features [Nb₂X₁₀] units (X = O, F) of two edge-shared octahedra with short (2.5739(1) Å) Nb–Nb bonds. The [Nb₂X₁₀] units are connected through shared O/F vertices to form a 3D structure configurationally isotopic to ζ-Nb₂O₅. Nb₂O₂F₃ undergoes a structural transition below 90K to a triclinic structure (space group: *P* $\bar{1}$; a=5.1791(5)Å, b=5.7043(6)Å, c=6.8911(7)Å, α=108.669(3)°, β= 109.922(2)°, γ=90.332(3)°). The transition can be described as a disproportionation or charge ordering of [Nb₂]⁷⁺ dimers: (2[Nb₂]⁷⁺ → [Nb₂]⁶⁺ + [Nb₂]⁸⁺), resulting in doubly (2.5000(9) Å) and singly bonded (2.6560(9) Å) Nb₂ dimers. The structural transition is accompanied by an unusual field-independent ‘spin-gap like’ magnetic transition. Electronic structure calculations indicate that a rare semiconductor–to–poor-metal electronic transition.

7.2 Introduction

The design and synthesis of new materials with desired and tunable properties continues to be a major goal of synthetic solid state chemists. One such class of materials are strongly correlated electron systems which exhibit a range of unusual physical phenomena, such as superconductivity, charge-density-wave (CDW)/spin-density-wave (SDW), metal-insulator transitions, and low-dimensional electronic and magnetic properties.¹⁻⁵ Strongly correlated electron materials provide a foundation for a new understanding of the physics and chemical bonding of the solid state.⁶⁻⁷ Reduced early transition metal oxides and halides have been an intense area of chemical research for many decades owing to the abundance of novel structures and compounds they exhibit, and hence offer a fertile area for exploratory research for new strongly correlated materials.

On the basis of known intrinsic physical behaviors, the compounds of niobium in low oxidation states have been of significant interest.⁸⁻⁹ Reduced niobium halides and chalcogenides form a wealth of metal-metal bonded cluster compounds.^{8,10-12} In contrast, the number of reduced Nb oxides and fluorides is relatively moderate, and the synthesis of reduced niobium oxyfluorides remains a challenge.⁹ Yet, interesting properties have been observed in some low-valent oxoniobates: $\text{Nb}_{12}\text{O}_{29}$ with an average Nb valence of 4.83 was reported to be a metallic antiferromagnet ($T_N = 12$ K);¹³ BaNbO_x was found to be superconducting with $T_c \sim 20$ K;¹⁴ and delithiated phases Li_xNbO_2 with $x = 0.45, 0.50 - 0.60$ were reported to exhibit superconducting transition at temperatures of 5.5 K and 14 – 17 K, respectively.¹⁵⁻¹⁶

The chemistry of niobium oxyfluorides is primarily dominated by the pentavalent state Nb(V).¹⁷⁻²⁰ Synthetic routes to the oxyfluorides using appropriate mixtures of starting materials are usually performed at high temperatures and/or under highly oxidizing (acidic) conditions that often result with Nb in its highest oxidation state.⁹ Successful synthesis of reduced Nb oxyfluorides has so far been limited to $\text{NaNb}_3\text{O}_5\text{F}$ and ANbO_2F (A=Li, Na or K).²¹⁻²² It is also notable that the cubic niobium trifluoride, NbF_3 (ReO_3 -type) may actually contain and be stabilized by oxygen.²³⁻²⁶ In this Chapter, we report the synthesis and characterization of a new reduced mixed-valent Nb(III/IV) oxyfluoride, $\text{Nb}_2\text{O}_2\text{F}_3$, including its crystal structure, physical properties (transport, magnetism, vibrational spectra and heat capacity), and chemical bonding.

7.3 Experiments

Details of the synthesis and characterizations are presented in Chapter 3. Specific descriptions of single crystal X-ray diffraction for $\text{Nb}_2\text{O}_2\text{F}_3$ are discussed in this section. Since O and F atoms cannot be well differentiated by X-ray diffraction, refinements with varying mixed O/F occupancies during the least-squares refinements were attempted. However, the refinement of the two data sets (room temperature and low temperature) did not proceed very nicely and the thermal displacement parameters of some O/F atoms were not well-behaved (non-positive definite). The structural modeling was then improved and completed by refining O and F separately at the different sites. For the monoclinic structure: F was satisfactorily refined at the X1 and X2 sites, and O was refined at the X3 site. For the low temperature triclinic structure: F was refined at the X1, X2 and X3 sites, and O was refined at the X4 and X5 sites.

Bond valence sum (BVS) calculations, based on the empirical expression $S_i = \exp[(R_0 - R_i)/B]$ where S_i = valence of bond “ i ” and $B=0.37$,²⁷ were performed for both crystal structures. For monoclinic (M)-Nb₂O₂F₃, BVS of Nb^{3.5+}, O²⁻ (X3) and F⁻ (X1, X2) resulted in values of 3.39, 1.64, and 1.16–1.17, respectively. For triclinic (T)-Nb₂O₂F₃, BVS of Nb³⁺, Nb⁴⁺, O²⁻ (X4, X5) and F⁻ (X1, X2, X3) resulted in values of 3.10, 3.66, 1.72–1.75, and 1.14–1.17, respectively. Nevertheless, we still cannot completely discount disorder between O and F atoms in the ligand sites (X). Thus, we assign X as O/F disorder in the structural description. Relevant crystallographic data, selected bond distances and angles, atomic coordinates and equivalent isotropic displacement parameters and bond valence sum calculations for monoclinic (M)-Nb₂O₂F₃ and triclinic (T)- Nb₂O₂F₃ are given in Tables 7.1 – 7.5.

Table 7.1 Crystallographic data for monoclinic (M)-Nb₂O₂F₃ and triclinic (T)-Nb₂O₂F₃

	(M)-Nb ₂ O ₂ F ₃		(T)-Nb ₂ O ₂ F ₃
M/gmol ⁻¹	274.82	274.82	274.82
T/K	296(2)	296(2)	83(2)
$\lambda/\text{\AA}$	0.71073	0.71073	0.71073
Crystal system	Monoclinic	Monoclinic	Triclinic
Space group	<i>I</i> 2/a (No. 15) (preferred)	<i>C</i> 2/c (No. 15) (standard)	<i>P</i> $\bar{1}$ (No. 2)
a/ \AA	5.7048(1)	12.9654(2)	5.1791(5)
b/ \AA	5.1610(1)	5.1610(1)	5.7043(6)
c/ \AA	12.2285(2)	5.7048(1)	6.8911(7)
α/deg	90	90	108.669(3)
β/deg	95.751(1)	110.212(1)	109.922(2)
γ/deg	90	90	90.332(3)
V/ \AA^3	358.225(11)	358.225(11)	179.82(3)
Z	4	4	2
d _c /gcm ⁻³	5.096	5.096	5.076
μ/mm^{-1}	6.342	6.342	6.317
2 $\theta_{\text{max}}/^\circ$	75.7	75.7	55
No. of reflections	958	958	785
No. of parameters	34	34	65
R _{int}	0.019	0.019	0.032
GOF	1.240	1.240	1.201
R(F) ^a	0.0121	0.0121	0.0370
R _w (F _o ²) ^b	0.0340	0.0348	0.1100
^a R(F) = $\Sigma F_o - F_c /\Sigma F_o $. ^b R _w (F _o ²) = $[\Sigma w(F_o^2 - F_c^2)^2/\Sigma w(F_o^2)^2]^{1/2}$			

Table 7.2 Selected bond distances (Å) and angles (deg) for monoclinic (M)-Nb₂O₂F₃ and triclinic (T)-Nb₂O₂F₃ (X = O/F)

(M)-Nb ₂ O ₂ F ₃		(T)-Nb ₂ O ₂ F ₃	
Nb – Nb	2.5739(1)	Nb1 – Nb1	2.5000(9)
Nb – X1	2.0690(7)	Nb1 – X1	2.124(3)
Nb – X1	2.1158(7)	Nb1 – X2	2.137(3)
Nb – X2	2.0966(4)	Nb1 – X3	2.087(3)
Nb – X3	1.9586(8)	Nb1 – X4	2.067(3)
Nb – X3	2.0463(8)	Nb1 – X4	2.077(3)
Nb – X3	2.0534(8)	Nb1 – X5	2.038(3)
X1 – Nb – X2	90.32(2)	Nb2 – Nb2	2.6560(9)
X1 – Nb – X3	90.78(3)	Nb2 – X1	2.068(3)
X1 – Nb – X3	88.20(3)	Nb2 – X2	2.069(3)
X2 – Nb – X3	94.59(3)	Nb2 – X3	2.095(3)
X2 – Nb – X3	85.12(3)	Nb2 – X4	1.891(4)
X3 – Nb – X3	92.21(1)	Nb2 – X5	2.027(3)
X3 – Nb – X3	94.85(2)	Nb2 – X5	2.033(3)
Nb – X1 – Nb	135.85(4)		
Nb – X2 – Nb	139.99(5)		
Nb – X3 – Nb	77.78(3)		
		X1 – Nb1 – X2	92.22(11)
		X1 – Nb1 – X4	81.40(12)
		X3 – Nb1 – X4	91.97(12)
		X3 – Nb1 – X4	90.77(12)
		X4 – Nb1 – X5	90.76(13)
		X4 – Nb1 – X5	95.20(14)
		Nb1 – X2 – Nb2	138.39(15)
		Nb1 – X3 – Nb2	133.50(14)
		Nb1 – X4 – Nb1	74.20(12)
		X1 – Nb2 – X3	87.55(11)
		X1 – Nb2 – X4	98.63(13)
		X2 – Nb2 – X5	88.84(13)
		X3 – Nb2 – X4	90.26(13)
		X3 – Nb2 – X5	83.89(12)
		X4 – Nb2 – X5	93.63(13)
		X4 – Nb2 – X5	95.00(14)
		Nb2 – X5 – Nb2	81.70(12)

Table 7.3 Atomic coordinates and equivalent isotropic displacement parameters (\AA^2) for monoclinic (M)- $\text{Nb}_2\text{O}_2\text{F}_3$ ($I2/a$) (X = O/F)

Atom	x	y	z	U_{eq}^a	Wyckoff
Nb	0.84641(2)	0.24545(2)	0.15927(2)	0.00421(5)	8f
X1	0.63268(2)	0.55085(2)	0.10270(6)	0.01000(2)	8f
X2	0.75000	0.1065(2)	0.00000	0.01046(2)	4e
X3	0.55999(2)	0.04303(2)	0.20093(6)	0.00709(2)	8f

^a U_{eq} is defined as one-third of the trace of the orthogonalized U_{ij} tensor

Table 7.4 Atomic coordinates and equivalent isotropic displacement parameters (\AA^2) for triclinic (T)- $\text{Nb}_2\text{O}_2\text{F}_3$ (X = O/F)

Atom	x	y	z	U_{eq}^a	Wyckoff
Nb1	0.58000(9)	0.68111(8)	0.67621(7)	0.0036(3)	2i
Nb2	0.92495(9)	0.80700(8)	0.31351(7)	0.0037(3)	2i
X1	0.8866(6)	0.7472(5)	0.9920(5)	0.0064(6)	2i
X2	0.4284(6)	1.0280(5)	0.7853(5)	0.0065(6)	2i
X3	0.3357(6)	0.5294(5)	0.8037(4)	0.0066(6)	2i
X4	0.7617(7)	0.3583(6)	0.6050(5)	0.0053(7)	2i
X5	0.8454(5)	0.8597(6)	0.5928(6)	0.0055(7)	2i

^a U_{eq} is defined as one-third of the trace of the orthogonalized U_{ij} tensor

Table 7.5 Bond valence analysis for monoclinic (M)-Nb₂O₂F₃^a

Atom	O × 2	F1 × 2	F2	Σcation
Nb × 2	1.28 1.01 0.991	1.24 1.10	1.16	3.39
Σanions	1.64	1.17	1.16	

^a Bond valence sums calculated with the formula: $S_i = \exp[(R_0 - R_i)/B]$, where S_i =valence of bond “*i*” and $B=0.37$

Table 7.5 Bond valence analysis for triclinic (T)-Nb₂O₂F₃^a

Atom	O1	O2	F1	F2	F3	Σcation
Nb1	0.953 0.927	1.025	1.08	1.04	1.19	3.10
Nb2	1.55	1.07 1.05	1.24	1.25	1.16	3.66
Σanions	1.72	1.75	1.16	1.14	1.17	

^a Bond valence sums calculated with the formula: $S_i = \exp[(R_0 - R_i)/B]$, where S_i =valence of bond “*i*” and $B=0.37$

7.4 Results and Discussion

7.4.1 Structures

The monoclinic (space group $I2/a$) crystal structure of $\text{Nb}_2\text{O}_2\text{F}_3$ in Figure 7.1a features $[\text{Nb}_2\text{O}_4\text{F}_6]$ dimeric units containing short Nb–Nb bonds of 2.5739(1) Å. Since differentiation between O and F atoms cannot be confirmed by X-ray diffraction (and for simplicity) the assignment Nb_2X_5 ($\text{X} = \text{O}, \text{F}$) will be used in the structural description. The dimers can be described as $[\text{Nb}_2(\mu_2\text{-X})_2\text{X}_8]$ units consisting of two distorted NbX_6 octahedra condensed through shared edges. Neighboring $[\text{Nb}_2(\mu_2\text{-X})_2\text{X}_8]$ units are linked through shared vertices of 8 X atoms to form $[\{\text{Nb}_2(\mu_2\text{-X})_{2 \times 2/3}\text{X}_{2 \times 1/3}\text{X}_{6/2}\}_\infty]$ slabs along the ab -plane. The slabs are then linked through bridging ligands (X) along the c -axis to form a 3D Nb_2X_5 network, as shown in Figure 7.1a. The Nb–X distances in the Nb_2X_{10} dimer units, range from 1.9586(8) – 2.1158(7) Å. The monoclinic structure of $\text{Nb}_2\text{O}_2\text{F}_3$ is configurationally isotypic to $\zeta\text{-Nb}_2\text{O}_5$,²⁸ although the shortest Nb–Nb distances (3.404(5) Å) in $\zeta\text{-Nb}_2\text{O}_5$ are nonbonding and longer than the equivalent Nb–Nb bonding distances in $\text{Nb}_2\text{O}_2\text{F}_3$. Thus, a topochemical structural relationship exists between $\text{Nb}_2\text{O}_2\text{F}_3$ and $\zeta\text{-Nb}_2\text{O}_5$, where the F substitution of O in $\zeta\text{-Nb}_2\text{O}_5$ results in the chemical reduction of Nb and Nb–Nb metal bond formation.

Single crystal structure determination, performed at 83 K, revealed the structural nature of the phase transition at 90 K. A structural transition from a monoclinic ($I2/a$) to triclinic lattice ($P\bar{1}$) is observed, represented by the loss of I -centering in the monoclinic lattice. The symmetry reduction is manifested by the emergence of two nonequivalent

Nb_2X_{10} dimers with different Nb–Nb bond lengths in the triclinic structure (in Figure 7.1b). One Nb_2X_{10} unit has shorter (2.5000(9) Å), and the other have longer (2.6560(9) Å) Nb–Nb bond lengths.

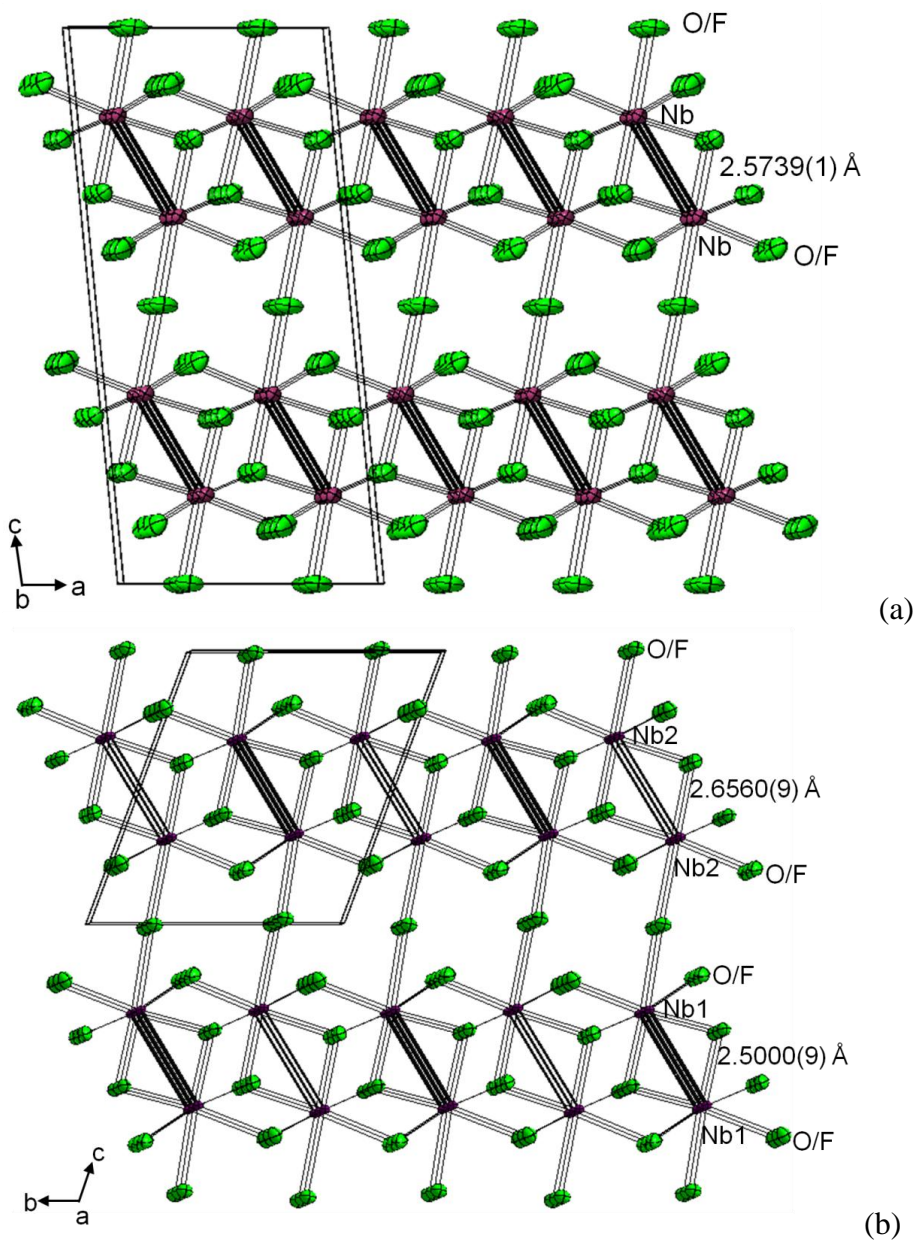


Figure 7.1 ORTEP representation of the crystal structures of (a) monoclinic (M)- $\text{Nb}_2\text{O}_2\text{F}_3$ and (b) triclinic (T)- $\text{Nb}_2\text{O}_2\text{F}_3$. Ellipsoids are drawn at 90% probability.

7.4.2 Energy-dispersive X-ray spectroscopy (EDS) Analysis

The semi-quantitative EDS measurements were taken three times from the selected Nb₂O₂F₃ crystal that was used for X-ray diffraction analysis. The results confirm the presence of Nb, O and F and the absence of Sn above ≈ 0.03 wt.% level.

Element	Atomic % Experimental	Atomic % Theoretical
Nb	27.94(3)	28.57
O	30.52(9)	28.57
F	41.54(7)	42.86

7.4.3 Magnetic properties

The magnetic susceptibility of Nb₂O₂F₃ (see Figure 7.2) increases upon cooling below room temperature and shows a large precipitous drop below 90 K, indicating a phase transition that quenches the magnetic moment. A large thermal hysteresis of cooling and heating data indicates a strongly first-order nature of the phase transition. Quenching of the magnetic moment at the transition suggests a spin-gap formation, often observed in a spin-Peierls system, with the pairing of two spins forming a singlet state with no spin momentum.²⁹⁻³⁰ To clarify whether the transition is driven by magnetic interactions as in spin-Peierls systems, the transition was studied in the vicinity of the critical temperature as a function of magnetic fields up to 5 Tesla. No change in the transition temperature or the width of the thermal hysteresis was observed, indicating that an origin of the phase transition is unlikely magnetically driven.

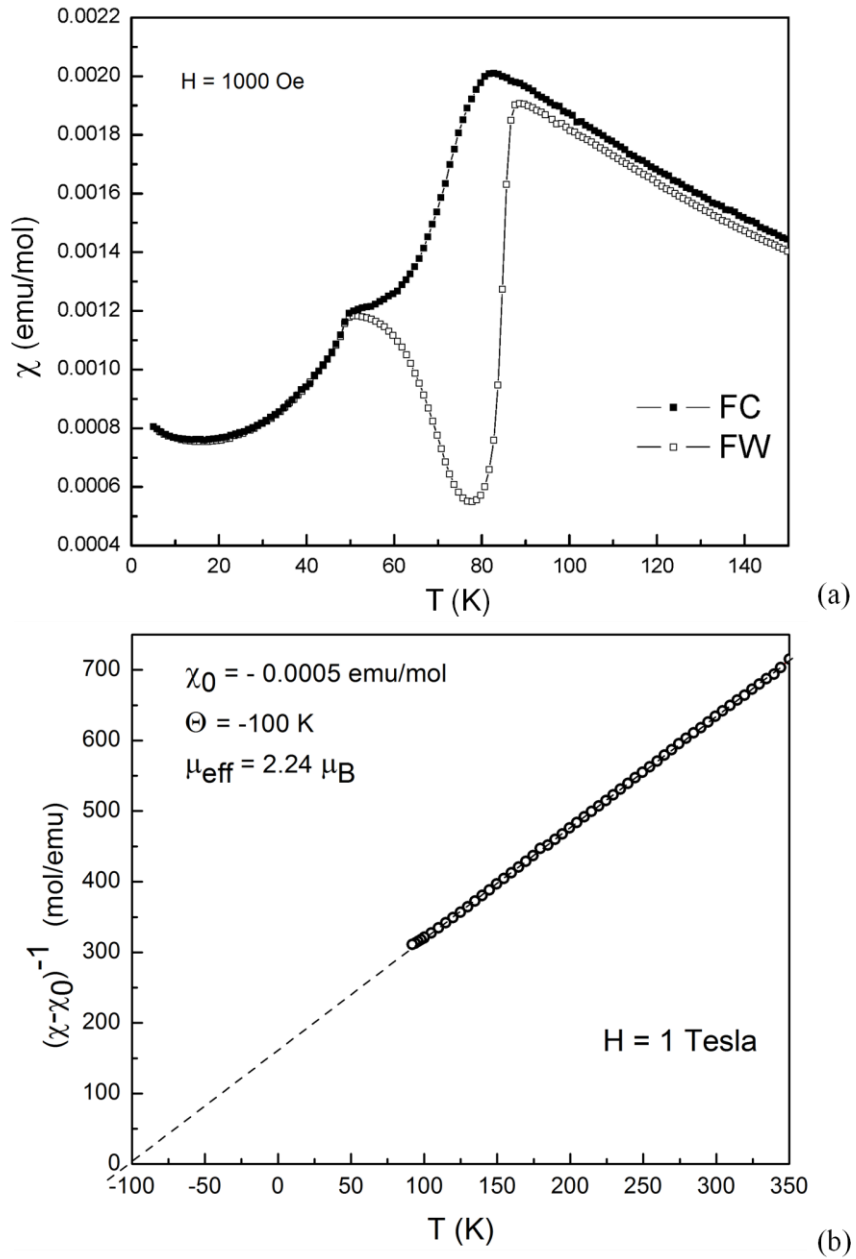


Figure 7.2 (a) Magnetic susceptibility (χ) of $\text{Nb}_2\text{O}_2\text{F}_3$ upon field-cooling (FC) and field-warming (FW), $T = 2 - 150$ K, $H = 1000$ Oe; (b) the reciprocal of magnetic susceptibility ($\chi - \chi_0$) of $\text{Nb}_2\text{O}_2\text{F}_3$ as a function of temperature ($T > 90$ K), $H = 1$ T

Above the critical temperature ($T > 100$ K) the susceptibility fits a Curie-Weiss law with a small diamagnetic contribution ($\chi_0 = -5 \times 10^{-4}$ emu/mol) which can be attributed to the paired 4d electrons in the Nb–Nb bond. The inverse susceptibility, $(\chi - \chi_0)^{-1}$, changes linearly with temperature (Figure 7.2b) above the phase transition, and the Weiss temperature ($\Theta = -100$ K) indicates antiferromagnetic exchange interactions between the Nb₂ dimer spins. The effective magnetic moment, $\mu_{\text{eff}} = 2.24$ μ_B , (per Nb₂ dimer) is consistent with $S = 1/2$ and a [Nb–Nb]⁷⁺O₂F₃ assignment, with Nb–Nb bond order of 1.5 and having unpaired electrons at the Nb π -bonding orbitals. The slightly larger value of μ_{eff} to the spin only value of 1.74 could be an indication of an incompletely quenched orbital moment.

To gain more insight into the two anomalies of χ clearly seen near 50 K and 90 K (Figure 7.2a) and their thermodynamic signature, the heat capacity C_p was measured over a wide temperature range, as shown in Figure 7.3. Two sharp peaks confirm the transitions at 50 K and 90 K, respectively. In between these temperatures, C_p follows the normal temperature dependence as extrapolated between the high ($T > 80$ K) and low ($T < 50$ K) temperature ranges, although the magnetization reveals large thermal hysteresis effects. The observed temperature dependence of the magnetization suggests possible coexistence of competing magnetic states or the system being at non-equilibrium.

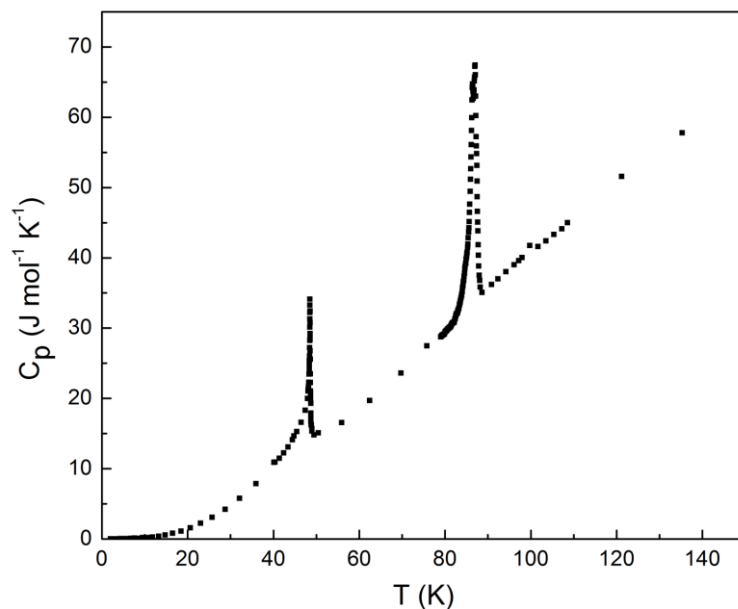


Figure 7.3 Temperature dependence (2 K to 150 K) of heat capacity (C_p) of $\text{Nb}_2\text{O}_2\text{F}_3$ in the vicinity of the phase transitions

To further understand the change of the magnetization, additional measurements of the time dependence of the magnetization at a given temperature (T) were performed by cooling down very fast from 110 K to T K. It is observed that the magnetization at 80 and 45 K, before and after the transition, slightly decreases over time. (see Figure 7.4). At 75, 70 and 55 K, however, the magnetization changes significantly as the time goes. The changes in the time dependence of the magnetization at 75 and 70 K drop exponentially and then stay essentially unchanged after 4000 and 2000 seconds (~ 1.1 and 0.56 hours), respectively. The magnetization at 55 K, nonetheless, decreases continuously over 6000 seconds (~ 1.7 hours) (see Figure 7.4). It suggests that the transition occurs relatively slow to reach equilibrium and the dynamic signature should be taken into account.

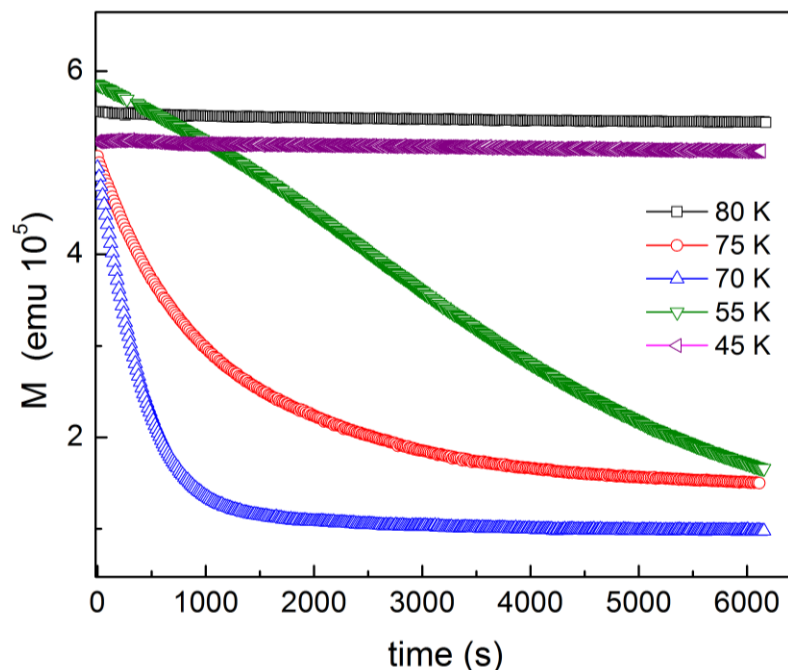


Figure 7.4 Time dependence (0 to 6000 seconds) of the magnetization of $\text{Nb}_2\text{O}_2\text{F}_3$ at 80, 75, 70, 55 and 45 K (T). The temperature was decreased very fast from 110 K to T K where the measurements were performed.

To answer the question whether it is required a certain period of time for a stable state being established, the temperature dependence of the magnetization was measured after equilibrating the system. Figure 7.5 depicts that the thermal hysteresis is observed in the vicinity of the phase transition near 80 K, that is consistent with the first order phase transition discussed earlier. In addition, the anomaly of the magnetization near 50 K is no longer present after the relaxation occurred. This indicates that the thermodynamic driving force governs the transition, nevertheless, it is likely that an activation energy is associated with the rate of the transition. The dynamic origin could possibly arise from the O/F diffusion during the transition to accommodate the charge ordering (CDW) in Nb_2 dimers. Yet, the true nature of the behavior is needed to be further investigated.

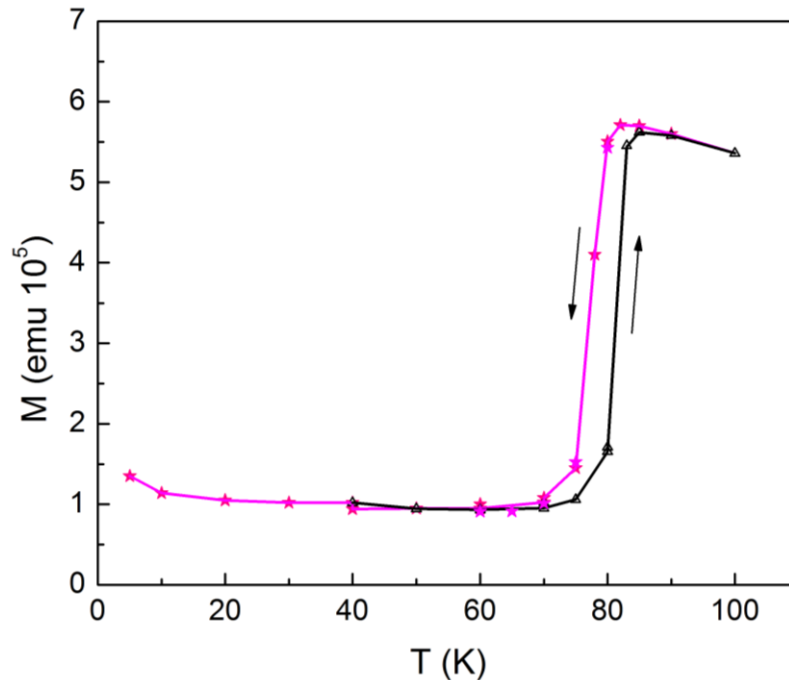


Figure 7.5 Temperature dependence (5 to 100 K) of the magnetization of $\text{Nb}_2\text{O}_2\text{F}_3$ after the relaxation

7.4.4 Transport properties

Electrical transport measurements on $\text{Nb}_2\text{O}_2\text{F}_3$ indicate a semiconducting temperature dependence of the resistivity (in Figure 7.6). The resistivity (ρ) increases rapidly and reaches a magnitude of nearly giga-Ohms-cm near the phase transition. At the critical temperature, ρ appears to show a maximum, and begins to drop at lower temperatures. However, the transport measurements could not be extended to below 80 K since the contact resistance increased and any unguarded measurement becomes questionable in this range. The inset in Figure 7.6 shows that a simple thermally activated conduction process cannot describe the data very well (the plot of $\ln(R)$ vs. $1/T$ would be expected to be linear). This indicates $\text{Nb}_2\text{O}_2\text{F}_3$ is not a simple semiconductor and suggests a more

complex transport mechanism, like variable range hopping behavior wherein electronic correlations and/or disorder induced by oxygen-fluorine disorder play important roles.³¹

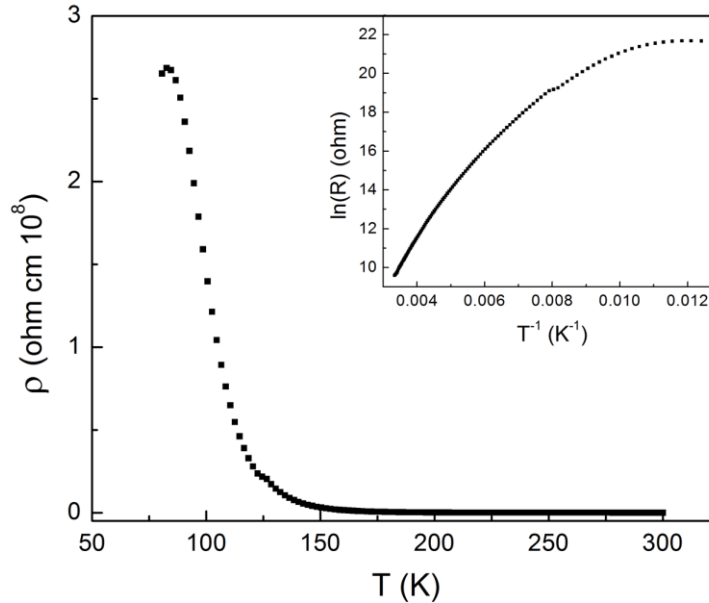


Figure 7.6 Plot of resistivity (ρ) of $\text{Nb}_2\text{O}_2\text{F}_3$ as a function of temperature ($T = 80 - 300$ K). Inset: plot of $\ln(R)$ vs. $1/T$

7.4.5 Raman Scattering, Structural and Magnetic Phase Transition

As aforementioned, single crystal structure determination, performed at 83 K, revealed the structural nature of the phase transition. A structural transition from a monoclinic ($I2/a$) to triclinic lattice ($P\bar{1}$) is observed. The symmetry reduction is manifested by the emergence of two nonequivalent Nb_2X_{10} dimers with different Nb–Nb bond lengths in the triclinic structure (in Figure 7.1b). The structural transition can be described as a charge-ordering (CDW) or disproportionation into mixed-valent dimer states: $2[\text{Nb}_2]^{7+} \rightarrow [\text{Nb}_2]^{6+} + [\text{Nb}_2]^{8+}$, wherein $[\text{Nb}_2]^{6+}$ and $[\text{Nb}_2]^{8+}$ dimers have double

and single bonds, respectively. Furthermore, the spin-gap-like behavior can be attributed to a transition from a Mott insulating paramagnetic state ($M\text{-Nb}_2\text{O}_2\text{F}_3$, $I2/a$) with $S = \frac{1}{2}$, to a mixed-valent or CDW state ($T\text{-Nb}_2\text{O}_2\text{F}_3$, $P\bar{1}$) with $S = 0$.

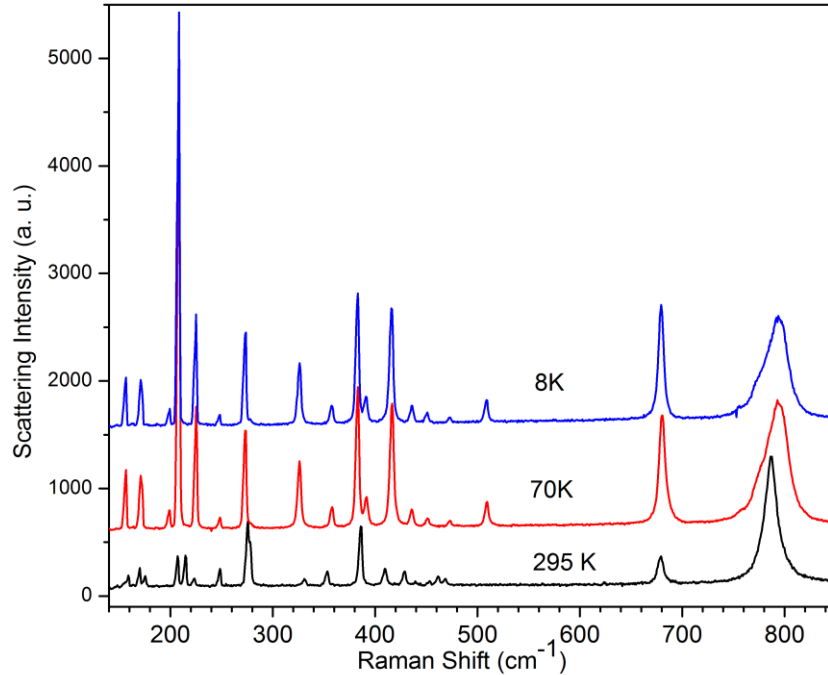


Figure 7.7 Raman scattering spectra of $\text{Nb}_2\text{O}_2\text{F}_3$ at 295, 70 and 8 K. Note that the changes occur below 90 K (at 70 K).

The structural phase transition is confirmed by Raman scattering measurements, where the mode frequency as a function of temperature (8 – 295 K) was observed to remarkably change at temperatures below 80 K (Figure 7.7). The observed number of Raman-active modes and their position agree well with calculated values. In lowering the temperature to ~ 80 K there are no changes in the scattering spectra apart from normal (some small hardening) shifts of lines due to lattice anharmonicity (Figure 7.8). However, drastic changes occur upon cooling below and near the transition temperature. Most of the scattering lines are shifted in frequency by as much as 10 cm^{-1} . However, the

total number of observed lines remains the same, as the number of atoms within the primitive cells (*I*-centered monoclinic and triclinic) is unchanged. Furthermore no changes in the Raman scattering spectra were observed from 8–70 K, indicating the magnetic transition observed at ~50K is not associated with a significant structural transformation.

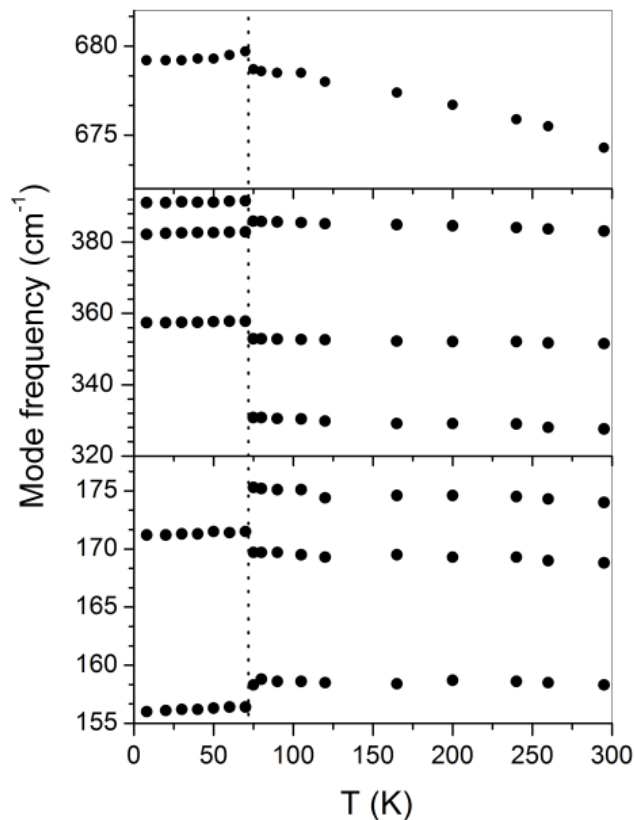


Figure 7.8 Temperature dependence ($T = 8\text{--}295\text{ K}$) of the frequencies of selected Raman-active modes of $\text{Nb}_2\text{O}_2\text{F}_3$. The phase transition below 90K is indicated by a dashed line.

7.4.6 Electronic Structure

The electronic structure and metal-metal bonding of dimeric M_2X_{10} units as in $Nb_2O_2F_3$ have been well studied.³²⁻³³ A simple molecular orbital (MO) approach provides a useful starting point in understanding the structural/electronic behavior of the title compound. Metal-metal bonding interactions arise from the orbital mixing of the t_{2g} -derived $4d$ orbitals of the Nb atoms forming six hybrid MO's: σ , π , δ , δ^* , π^* , σ^* ; listed in increasing energy; (the e_g -derived Nb orbitals are involved in Nb-O/F interactions). Allowing for Nb_2^{7+} (d^1-d^2) electron assignment in the Nb_2 dimer results in the MO electron configuration: σ^2, π^1 ; with Nb-Nb bond order of 1.5. It is noted that the observed Nb-Nb distance in $Nb_2O_2F_3$ is shorter than the reported Nb-Nb triple bond distance (2.614 Å) in $NaNb_3O_5F$,²¹ nevertheless Nb-Nb bonds have also been reported to be insensitive to bond multiplicity.³⁴ Continuing the MO arguments to the extended solid, bands around the Fermi level are expected to be t_{2g} -derived Nb_2 states. The expected band-filling corresponds to a metallic half-filled π -band which gives rise to instability with respect to possible magnetic ordering, bond formation and/or charge ordering.³⁵⁻³⁶

The semiconducting and paramagnetic behavior of $Nb_2O_2F_3$ above 90 K suggests strong correlations akin to Mott insulators. Density functional theory (DFT) confirms this classic MO analysis. The monoclinic structure, Figure 7.9, is a semiconductor with a calculated band gap of approximately 1 eV. The DOS near the Fermi level are comprised of exclusively Nb d-orbitals. The bands below E_F arise from fully filled π - and σ -interactions of the Nb^{7+} ions, which is consistent with Nb-Nb dimer formation. The transformation to the triclinic structure on cooling leads to a unique electronic

rearrangement, most notably a loss of the band gap. It is apparent from these calculations that $\text{Nb}_2\text{O}_2\text{F}_3$ structure undergoes a semiconductor-to-metal transition coupled with this structural distortion. The triclinic compound contains a deep, non-zero pseudo-gap at E_F indicating poor metallic character. The bands below the pseudo-gap are associated with the shorter (2.5000(9) Å) Nb_2^{6+} and correspond to a fully filled σ - and π -interactions yielding an electron configuration of $\sigma^2\pi^2$ or Nb=Nb double bonds. The interactions for the Nb_2^{8+} dimers in contrast show a σ -interaction fully filled below E_F while the π -interactions are unoccupied above E_F . The result is an electron configuration of σ^2 or Nb–Nb single bonds.

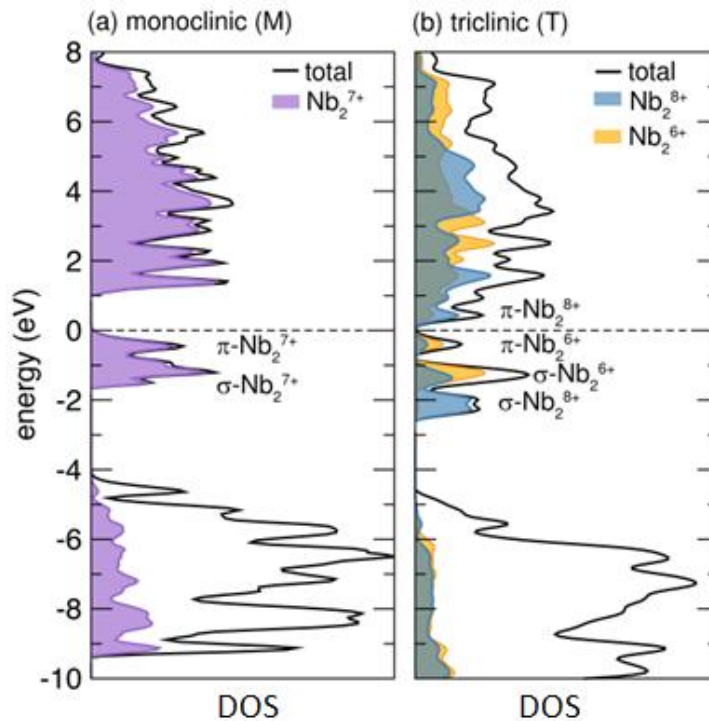


Figure 7.9 The density of states (DOS) of (a) monoclinic (M)- $\text{Nb}_2\text{O}_2\text{F}_3$ with the partial DOS for the Nb_2^{7+} dimers and (b) the triclinic (T)- $\text{Nb}_2\text{O}_2\text{F}_3$ with the partial DOS of the single bond Nb_2^{8+} and double bond Nb_2^{6+} shown. The respective Fermi levels (E_F) are set at 0 eV.

7.5 Conclusions

The synthesis of $\text{Nb}_2\text{O}_2\text{F}_3$ represents a unique example of a reduced niobium oxyfluoride derived from fluorine substitution of a simple binary Nb_2O_5 . $\text{Nb}_2\text{O}_2\text{F}_3$ possibly exhibits Mott variable-range hopping and undergoes an unusual ‘spin-gap’ formation ($T < 90\text{K}$) arising from the disproportionation of the metal-metal bonded dimers. A similar ‘spin-gap’ behavior associated with metal bond formation has been reported for $\text{Ba}_3\text{NaRu}_2\text{O}_9$.³⁷⁻³⁸ Electronic calculations indicate the ‘spin-gap’ transition in $\text{Nb}_2\text{O}_2\text{F}_3$ is accompanied by a loss of a band-gap leading to a rare semiconductor to poor-metal transition. In addition, it is suggestive that even the phase transition is governed by the thermodynamic driving force, the dynamic origin should be considered and needed to be further investigated. The low-temperature synthesis of $\text{Nb}_2\text{O}_2\text{F}_3$ in Sn-flux opens new directions for further exploratory studies in strongly correlated low-valent early-transition-metal oxyfluorides.

7.6 References

- (1) Kandpal, H. C.; Opahle, I.; Zhang, Y.-Z.; Jeschke, H. O.; Valenti, R. *Phys. Rev. Lett.* **2009**, *103*, 067004/1.
- (2) Simon, A. *Angew. Chem., Int. Ed. Engl.* **1997**, *36*, 1789.
- (3) Gabovich, A. M.; Voitenko, A. I.; Ausloos, M. *Phys. Rep.* **2002**, *367*, 583.
- (4) Si, Q.; Steglich, F. *Science* **2010**, *329*, 1161.
- (5) Morosan, E.; Natelson, D.; Nevidomskyy, A. H.; Si, Q. *Adv Mater* **2012**, *24*, 4896.
- (6) von Lohneysen, H.; Rosch, A.; Vojta, M.; Wolfle, P. *Rev. Mod. Phys.* **2007**, *79*, 1015.
- (7) Canadell, E.; Whangbo, M. H. *Chem. Rev.* **1991**, *91*, 965.
- (8) Simon, A. *Angew. Chem., Int. Ed. Engl.* **1981**, *20*, 1.
- (9) Köhler, J.; Svensson, G.; Simon, A. *Angew. Chem., Int. Ed. Engl.* **1992**, *31*, 1421.
- (10) Schäfer, H.; Schnering, H. G. *Angew. Chem.* **1964**, *76*, 833.
- (11) Miller, G. J. *J. Alloys Compd.* **1995**, *229*, 93.
- (12) Sokolov, M. N.; Fedin, V. P. *Coord. Chem. Rev.* **2004**, *248*, 925.
- (13) Cava, R. J.; Batlogg, B.; Krajewski, J. J.; Gammel, P.; Poulsen, H. F.; Peck, W. F., Jr.; Rupp, L. W., Jr. *Nature* **1991**, *350*, 598.
- (14) Strukova, G. K.; Kedrov, V. V.; Zverev, V. N.; Khasanov, S. S.; Ovchinnikov, I. M.; Batov, I. E.; Gasparov, V. A. *Physica C: Superconductivity* **1997**, *291*, 207.
- (15) Geselbracht, M. J.; Richardson, T. J.; Stacy, A. M. *Nature* **1990**, *345*, 324.

- (16) Xue, Z.; Dong, A.; Guo, Y.; Che, G. *J. Alloys Compd.* **2009**, *476*, 519.
- (17) Nieder-Vahrenholz, H. G.; Schäfer, H. *Z. Anorg. Allg. Chem.* **1987**, *544*, 122.
- (18) Cordier, S.; Roisnel, T.; Poulain, M. *J. Solid State Chem.* **2004**, *177*, 3119.
- (19) Guelin, J.; Ravez, J.; Hagenmuller, P. *J. Less-Common Met.* **1988**, *137*, 75.
- (20) Wadsley, A. D.; Andersson, S. *Perspect. Struct. Chem.* **1970**, *3*, 1.
- (21) Köhler, J.; Simon, A. *Angew. Chem., Int. Ed. Engl.* **1986**, *25*, 996.
- (22) Ruedorff, W.; Krug, D. *Z. Anorg. Allg. Chem.* **1964**, *329*, 211.
- (23) Ehrlich, P.; Ploger, F.; Pietzka, G. *Z. Anorg. Allg. Chem.* **1955**, *282*, 19.
- (24) Schäfer, H.; Schnering, H. G.; Niehues, K. J.; Nieder-Vahrenholz, H. G. *J. Less-Common Met.* **1965**, *9*, 95.
- (25) Delobbe, V.; Chassaing, J.; Bizot, D. *Rev. Chim. Miner.* **1985**, *22*, 784.
- (26) Brink, F. J.; Noren, L.; Withers, R. L. *J. Solid State Chem.* **2004**, *177*, 2177.
- (27) Brown, I. D. *Chemical Reviews* **2009**, *109*, 6858.
- (28) Ercit, T. S. *Mineral. Petrol.* **1991**, *43*, 217.
- (29) Khomskii, D. I. *Prog. Theor. Phys. Suppl.* **2005**, *159*, 319.
- (30) Voit, J. *Rep. Prog. Phys.* **1995**, *58*, 977.
- (31) Mott, N. F. *Phil. Mag.* **1969**, *19*, 835.
- (32) Goddard, R. J.; Hoffmann, R.; Jemmis, E. D. *J. Am. Chem. Soc.* **1980**, *102*, 7667.
- (33) Cotton, F. A.; Diebold, M. P.; O'Connor, C.; Powell, G. L. *J. Am. Chem. Soc.* **1985**, *107*, 7438.
- (34) Tayebani, M.; Feghali, K.; Gambarotta, S.; Yap, G. P. A. *Inorg. Chem.* **2001**, *40*, 1399.

- (35) Whangbo, M. H. *Acc. Chem. Res.* **1983**, *16*, 95.
- (36) Austin, I. G.; Mott, N. F. *Science* **1970**, *168*, 71.
- (37) Stitzer, K. E.; Smith, M. D.; Gemmill, W. R.; zur Loye, H.-C. *J. Am. Chem. Soc.* **2002**, *124*, 13877.
- (38) Kimber, S. A. J.; Senn, M. S.; Fratini, S.; Wu, H.; Hill, A. H.; Manuel, P.; Attfield, J. P.; Argyriou, D. N.; Henry, P. F. *Phys. Rev. Lett.* **2012**, *108*, 217205/1.

Chapter 8 Concluding Remarks

In this work, the structure-property relationships of several new solid-state materials, i.e., layered and three-dimensional insulating fluorocarbonates ($\text{KPb}_2(\text{CO}_3)_2\text{F}$, $\text{K}_{2.70}\text{Pb}_{5.15}(\text{CO}_3)_5\text{F}_3$, APbCO_3F where $A = \text{Rb}$ or Cs and AMgCO_3F where $A = \text{K}$ or Rb) and a highly correlated electron compound of $\text{Nb}_2\text{O}_2\text{F}_3$, have been investigated. These materials have been synthesized through hydrothermal and solid-state techniques ($\text{KPb}_2(\text{CO}_3)_2\text{F}$, $\text{K}_{2.70}\text{Pb}_{5.15}(\text{CO}_3)_5\text{F}_3$, APbCO_3F where $A = \text{Rb}$ or Cs and AMgCO_3F where $A = \text{K}$ or Rb) and a flux method ($\text{Nb}_2\text{O}_2\text{F}_3$). The reported compounds have been structurally and functionally characterized. The crystal structures have been determined from single crystal X-ray diffraction, that provide the basis of understanding their physical properties, i.e., SHG and piezoelectricity ($\text{K}_{2.70}\text{Pb}_{5.15}(\text{CO}_3)_5\text{F}_3$, APbCO_3F where $A = \text{Rb}$ or Cs and AMgCO_3F where $A = \text{K}$ or Rb), magnetic and transport properties ($\text{Nb}_2\text{O}_2\text{F}_3$). In addition, DFT calculations have been performed to gain further insight into the interplay of structure and property.

Two potassium lead fluorocarbonates $\text{KPb}_2(\text{CO}_3)_2\text{F}$ and $\text{K}_{2.70}\text{Pb}_{5.15}(\text{CO}_3)_5\text{F}_3$ have been discussed. The origin of centricity in the crystal structures was described. The double and triple-layers in $\text{KPb}_2(\text{CO}_3)_2\text{F}$ and $\text{K}_{2.70}\text{Pb}_{5.15}(\text{CO}_3)_5\text{F}_3$ are inherently noncentrosymmetric, as they are composed entirely of elements possessing a trigonal symmetry in the ab -plane. This makes a positive contribution to NCS material engineering as controlling the packing and polar directionality of these new structural building units to form acentric structures has become accessible.

Following the direction opened from the two potassium lead fluorocarbonates, other rubidium and cesium compounds in this family, RbPbCO₃F and CsPbCO₃F, have been discovered. These materials exhibit large SHG responses, 250 and 300 × α -SiO₂ and piezoelectricity with $d_{33} = 72$ and 94 pm/V for RbPbCO₃F and CsPbCO₃F, respectively. SAMD analyses indicate that the origin of the NLO response is derived from the microscopically polar PbO₆F₂ units and the cooperatively aligned acentric CO₃ groups. Importantly, for *achiral* and *nonpolar* compounds, the large inversion lifting distortion does not guarantee that a large NLO response will result; the relative orientation of the displacements contributing to the mode-polarization amplitude need to be taken into account. Even the enhanced SHG efficiencies were achieved in the rubidium and cesium lead fluorocarbonates, the band gaps ~ 300 nm (~ 4.1 eV), which are not very wide, hinder these materials from being used in deep UV NLO photonic application.

To create NCS materials with wide transparency windows, we substituted lead metal with a main group element – magnesium, that resulted in two deep UV NLO compounds, namely KMgCO₃F and RbMgCO₃F. These materials are SHG active at both 1064 and 532 nm incident radiation. KMgCO₃F and RbMgCO₃F exhibit the SHG efficiencies of 120, 160 × α -SiO₂ (1064 nm output) and 0.33, 0.60 × β -BBO (532nm output) and piezoelectricity with $d_{33} = 38$ and 49 pm/V, respectively. The SHG responses of these compounds are larger than those of the Ca and Sr analogues. The asymmetric distribution of charge of Mg[CO₃] layer in the *ab*-plane enhances the SHG responses of the compounds. That is attributed to the different denticity of Mg cation compared with those of other alkali-earth cations, i.e., the Mg cation is connected to one bidentate and two

monodentate linkages of $[\text{CO}_3]$ groups. In addition, KMgCO_3F and RbMgCO_3F possess wide transparency windows with the UV cut-off edges below 200 and 190 nm, respectively. This could be an indication that KMgCO_3F and RbMgCO_3F are potentially used for deep-UV NLO materials.

In line with discovering new synthetic manners for these aforementioned insulating nonlinear optical materials, we have explored another area of inorganic solid-state chemistry – highly correlated electron systems. A reduced niobium (III/IV) oxyfluoride, $\text{Nb}_2\text{O}_2\text{F}_3$, has been synthesized in Sn-flux. The low-temperature synthesis of $\text{Nb}_2\text{O}_2\text{F}_3$ has provided new routes for further exploratory studies on highly correlated low-valent transition-metal systems. $\text{Nb}_2\text{O}_2\text{F}_3$ undergoes an unusual ‘spin-gap’ formation that is attributed to the charge ordering (CDW) or disproportionation of metal-metal Nb-Nb bonds. It is observed that the material exhibits semiconducting paramagnetic behavior above the transition temperature. Additional investigations on the phase transition as a function of relaxation time could indicate that the dynamic contribution, which possibly arises from the more pronounced O/F diffusion at low temperature ~ 50 K, should be considered. Yet, the true nature of the transition is needed to be further studied.

Depending on the classes of materials with desired physical properties, appropriate synthetic manners are required to be found and executed successfully. In this work, we are able to synthesize a few materials from NLO insulators to highly correlated electron semiconductor. For laser and photonic-related systems, understanding the crystallographic architecture and the packing of new asymmetric structure building units facilitate the design of new NCS compounds. Mixed-metal fluorocarbonates with large

SHG responses and wide transparency windows are promising for NLO material engineering. In addition, a reduced niobium (III/IV) oxyfluoride has opened new directions to discovering other novel low-valent transition metal compounds. Understanding, at some certain degrees, the complex magnetic and electronic phase transition associated with the structural phase transition in $\text{Nb}_2\text{O}_2\text{F}_3$ has broadened perspectives on condensed matters for chemistry.

It is our intention to extend these studies to other (i) NLO fluorocarbonates of main group elements and (ii) early-transition-metal oxyfluorides or fluoronitrides. That potentially develops the understanding of (i) tunable SHG responses and (ii) unconventional correlated systems from atomic and electronic scales.